MODELING THE MICROSTRUCTURE EVOLUTION DURING HOT DEFORMATION OF MICROALLOYED STEELS

MODELING THE MICROSTRUCTURE EVOLUTION DURING HOT DEFORMATION OF MICROALLOYED STEELS

By

MOHAMMAD KASHIF UR REHMAN, B.Tech

A Thesis Submitted to the School of Graduate Studies in Partial Fulfilment of the
Requirements for the Degree Doctor of Philosophy

McMaster University

Doctor of Philosophy (2014)	McMaster University (Materials Science & Engineering), Hamilton, Ontario

TITLE: Modeling the Microstructure Evolution During Hot Deformation of Microalloyed Steels

AUTHOR: Mohammad Kashif Ur Rehman, B. Tech (National Institute of Technology, Jamshedpur)

SUPERVISORS: Dr. Hatem S. Zurob and Dr. S.V.Subramanian

NUMBER OF PAGES: xv, 174

Abstract

A physically based model has been developed to describe static recrystallization and grain coarsening of recrystallized grains during hot rolling of Nb microalloyed austenite. Key feature of recrystallization model is detailed description of the nucleation process; the model predicts recrystallization incubation time as well as time evolution of recrystallization nucleation rate along with recrystallized grain size. In addition to this, effect of static recovery, solute drag of Nb and precipitation of Nb(C,N) are captured in both recrystallization nucleation and growth models.

Once recrystallization is complete, fine recrystallized austenite grains tend to coarsen driven by its surface energy, which is captured in a physically based model. The present grain coarsening model takes into consideration effect of solute drag of Nb using Cahn’s model and precipitates using Zener drag. The model predictions are validated using the available experimental database in literature.

The model is applied to analyze quantitatively grain coarsening problem encountered between the end of roughing and the start of finish rolling under industrial processing conditions. The model enabled quantitative analysis of the effect of cooling rate on key metallurgical parameters, which determine the coarsening kinetics. Based on these results, an engineering solution to overcome grain coarsening problem was identified. The solution lies in accelerated water cooling upstream just after roughing. This engineering solution is being adopted in the design of next generation rolling mills for processing microalloying steels.

Acknowledgement

I am grateful for the excellent guidance and encouragement provided by my supervisors Dr. Zurob and Dr. Subramanian for their constructive advice, knowledge, patience and understanding. All our meeting were highly enriching experience. I am also deeply thankful to Dr. Provatas for serving on my supervisory committee.

I would also like to thank Diana Maltese and Nancy Cole for all the instances at which their assistance helped me along the way.

Financial support of Steel Research Center, McMaster University is gratefully acknowledged. Special thanks is owed to Mr Badgley and Mr Decker from U.S Steel Canada, Dr Nafisi, Dr Collins and Mr VanderBreggen from Evraz Inc. NA for providing rolling mill database and discussion on various issues currently faced by steelmakers in processing of low alloy steels.

I am also thankful to Mr Marcos Stuart from CBMM Brazil for arranging the interaction with steel makers in Europe and Asia so as to get a better appreciation of the technological problems.

Last but not the least I owe special thanks to my family and friends whose support and encouragement enabled me to complete this project.

Table of Contents

List of Figures

List of Tables

1. Introduction

No other material has as profound an effect on human civilization as iron and iron alloys. The progress of human civilization is closely related to the development of iron/steel making technologies. With the advent of Bessemer process of steel making at Sheffield England in 1855 mass production of cheap steels was made possible. This led to rapid development in infrastructure and allowed further expansion of industrial revolution and thus leading to modern society.

The current world production of crude steel is to the order of 1.5 billion tons. Due to continued demand of steel and environmental degradation associated with steel production, lot of research has been focussed on improving the mechanical properties of steel.

1.1. Hot rolling of steels

Historically steels for flat products used to be cast in blooms which were then rolled in an intermediate mill to create slabs for hot rolling. These slabs were then hot rolled to desired shape and size. The motivation for hot rolling previously was dimensional control rather than microstructure and mechanical property. Although the deformation cycle was never intentionally controlled for grain size evolution but due to multiple phase transformation cycles and high deformation the steels were subjected to, as-cast grain size and abnormal grains were less of an issue. Coupled to this, the low strength requirements of as-rolled steels made microstructure control during rolling not a priority. The strength requirements of those steels were fairly low. For more demanding applications such as boiler vessel, heat treated plates were used which gave a better control on mechanical properties. Historically the engineering design philosophy followed a stress based approach wherein the focus was to have high yield strength (stress based design). This was easy to achieve by small addition of carbide/nitride forming elements. Vanadium and molybdenum were two elements which were adopted readily by steel makers. During hot rolling these elements remain dissolved in austenite and precipitate later in ferrite during transformation. Grain refinement during phase transformation coupled with precipitation of microalloys (Ti, Nb and V) led to drastic increase in strength and toughness of steel with a very slight increase in input cost. This heralded the era of microalloyed steels.

With increased focus starting around 1970's on strain based engineering design researchers found that a two-step rolling process (roughing and finish rolling) gave better results. This was termed as thermo-mechanical controlled processing (TMCP) or recrystallized controlled rolling.

1.2. Microstructure control during hot rolling (TMC Process)

The main purpose of TMP of HSLA steels is to refine the ferrite grains, which leads to simultaneous increase in strength, ductility and low temperature fracture toughness. In this process hot rolling is carried out in two steps. The first deformation phase (rough rolling) is carried out at elevated temperatures (1050 to 1250 ^{o}C) so as to refine the as cast coarse grains by static recrystallization. After this the bar is held for the temperature to fall below 900 ^{o}C and then second deformation step (finish rolling) is carried out. Throughout the hot rolling process the time-temperature-deformation window is controlled in such a way that complete recrystallization is ensured in rough rolling and no recrystallization occurs during finish rolling.

A series of deformation without recrystallization leads to severe defect generation in the matrix. Also the equiaxed austenite grains become elongated resembling the shape of a pancake. The pancaked elongated grains have very high grain boundary area per unit volume compared to the strain free equiaxed grains. Since grain boundaries are preferential nucleation sites for austenite to ferrite phase transformation an increase in grain boundary area coupled with increase in defects drastically increases the potential nucleation sites for phase transformation thus giving further grain refinement. As is evident from **Figure 2**, for any equiaxed grain size a strained austenite gives finer ferrite grains than a strain free one.

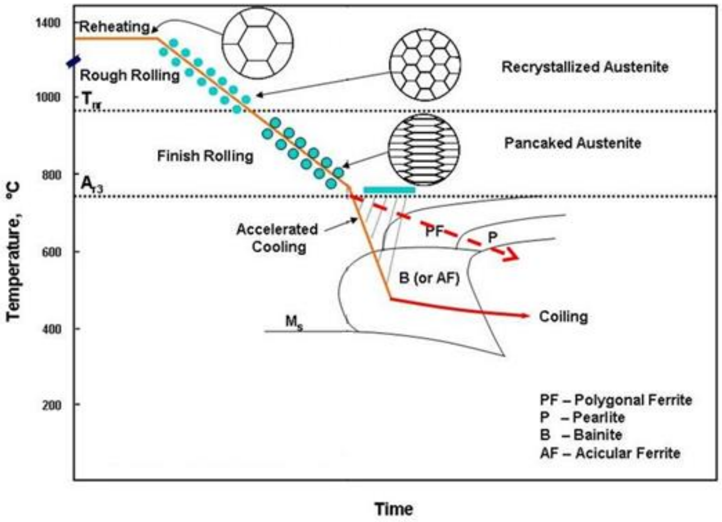

Figure 1: Schematic of thermo mechanical processing of steels showing the rough rolling temperature window where recrystallization is complete and finish rolling window wherein pancaking in absence of recrystallization takes place[1].

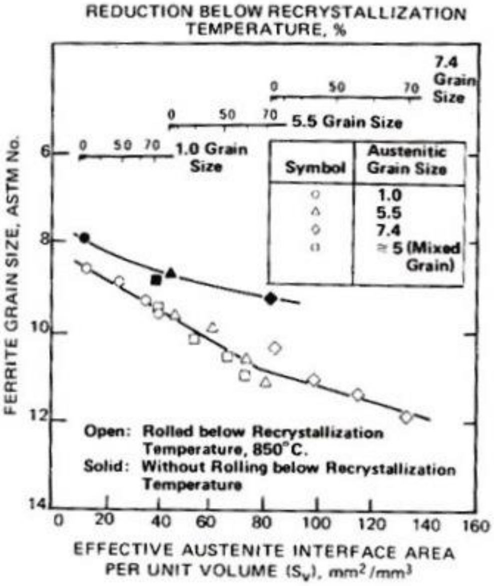

Figure 2: Variation of ferrite grain size, strain with interfacial area (S_v) in 0.03 wt % Nb steel [2].

Additions of alloying elements enhance mechanical properties significantly. Small amount of Nb, V and Ti are usually added either individually or in combination up till 0.1%. These steels are called microalloyed because of small percentage of alloying additions. The presence of microalloys either as a solute or in carbides/nitrides alters recovery and recrystallization kinetics thus allowing modification of rolling schedule. Nb is widely used to stop recrystallization at high temperature so as to allow finish rolling to be done at elevated temperature than what was originally possible without Nb. The steel chemistry and rolling parameters developed to capitalize on this aspect of Nb is called as HTP(high temperature processing) or more recently developed OHTP (optimized high temperature processing) process[3].Vanadium is added to precipitate out in ferrite during transformation giving precipitation hardening[4].

The key metallurgical processes operating during Thermo-Mechanical Controlled Processing (TMCP) are recovery, recrystallization, precipitation and grain coarsening[5]. Such processes are a function of composition, temperature, strain, strain rate, relaxation time. These processes are not mutually exclusive events and interact with each other in multiple ways. These factors influence the mechanical properties of steels in numerous ways and hence a good physical understanding of the process is essential to understand the underlying metallurgy.

1.3. Scope of thesis

The present study was motivated by the desire to further enhance our understanding of thermo-mechanical processing and associated grain refinement process.

Industrially this is achieved by a two stage rolling process wherein deformation is first applied at high temperature for grain refinement and further deformation is given at low temperature for strain accumulation.

In recent years the problem of strain accumulation has received increased focus due to the market demand for higher strength product with high toughness and in high thickness. Producing higher thickness products significantly reduces the total possible deformation which leads to reduced austenite grain refinement during rough rolling and reduced strain accumulation during finish rolling. This has led to increased focus on optimization of rolling schedules.

The present work focuses upon modeling of the evolution of microstructure following deformation of a supersaturated alloy. A quantitative physical model was developed which looks into various metallurgical phenomena and interaction between them during rolling in austenitic phase.

In the later part of the contribution, an attempt has been made to rationalize microstructure evolution of an industrial rolling schedule with the help of the developed model and comparison is made to an alternative hypothetical case.

2. Literature Review

The microstructure evolution during thermo-mechanical processing is manipulated using a combination of metallurgical processes viz. recovery recrystallization precipitation and grain coarsening. All of them interact with each other in numerous ways (**Figure 3**).

Over the last three decades, great progress has been made toward the modeling of thermo-mechanical processing of microalloyed steels [6-19]. The key to modeling microstructure evolution during the hot rolling of microalloyed steels is to capture the processes of recovery, recrystallization, and precipitation as well as their interactions.

Earlier work on this topic has led to development of powerful semi-empirical relationships that describe the interactions between recovery, precipitation, and recrystallization with great accuracy [4, 9, 10, 12, 15, 16, 20, 21].

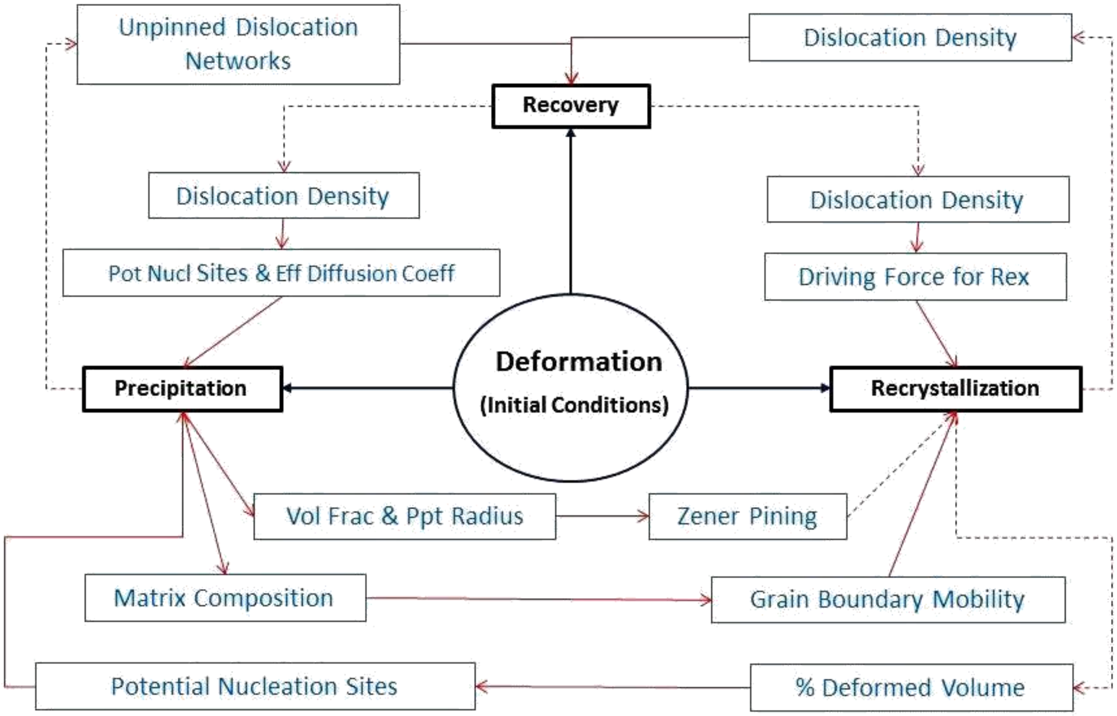

Figure 3: Schematic showing the various interactions between recovery, recrystallization and precipitation. The blue boxes represent sub-processes, dotted red line represents the inverse relationship whereas solid red line represents direct relationship.

This research project will focus on microstructure evolution during hot rolling and its application to steel processing.

2.1. Recovery

During hot rolling of steels most of the applied deformation energy gets converted into heat and only a fraction of it(~1%) remains as stored energy [12]. This extra energy is stored inside the material in the form of increased dislocation density.

Recovery is usually defined as a process by which deformed grains can reduce their stored energy by the removal or rearrangement of defects in their crystal structure.

Depending on the stacking fault energy (SFE) of the system some or all of the sub process will operate viz. formation of cells, annihilation of dislocations within cells, formation of low-angle sub-grains and sub-grain growth, **Figure 4**. This occurs by a combination of dislocation glide, cross-slip and climb. In case of low alloy microalloyed steels, austenite is unstable at room temperatures making direct observation using TEM difficult. Due to this recovery is usually studied in model materials such as Al, Cu etc.[22].

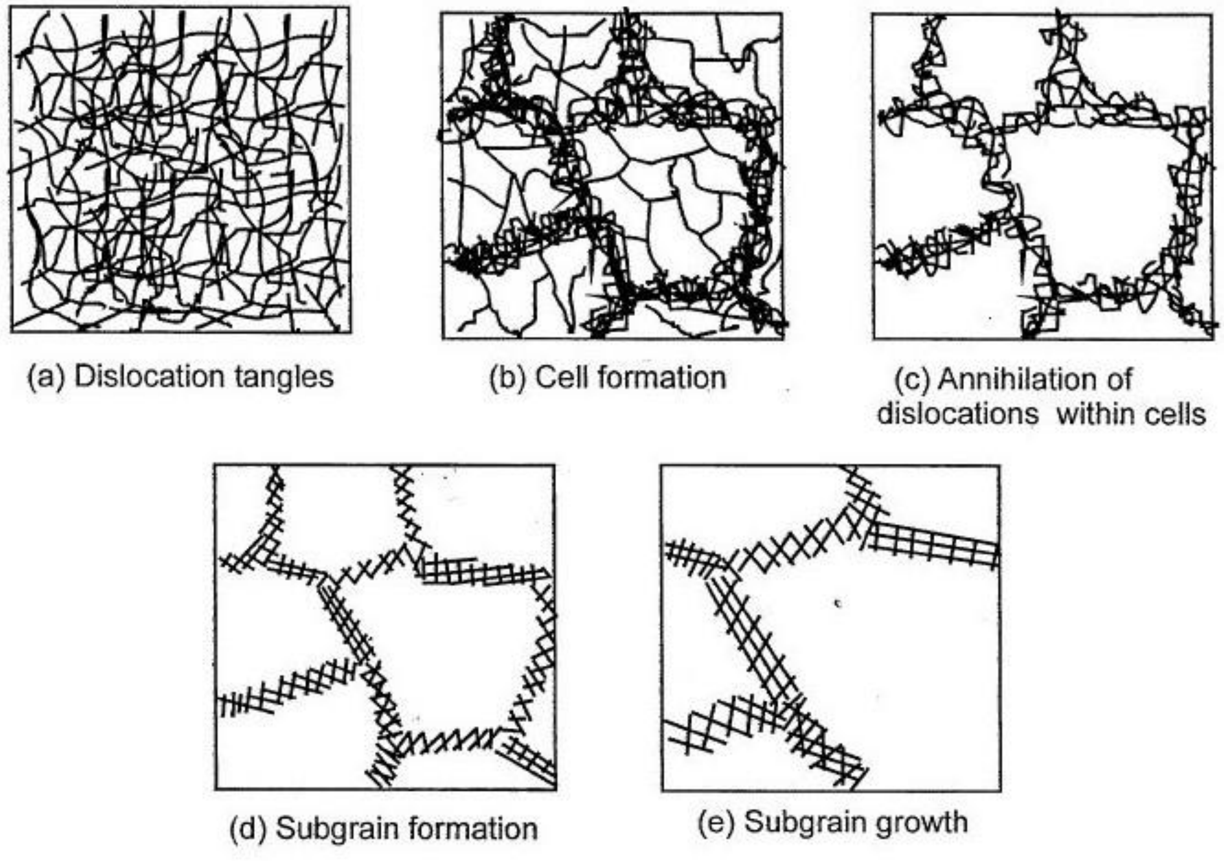

Figure 4: The stages of recovery where first cells are formed due to the rearrangement of dislocations and then subgrains are formed and grow due to annihilation of dislocations, from Humphreys and Hatherly[12].

2.1.1. Recovery Measurements

Since recovery progress is essentially a measure of reduction in stored energy of deformation, any method which can measure stored energy in principle will be able to measure the recovery kinetics. Due to high number density of dislocations involved number counting of dislocations is impossible. Direct methods such as Calorimetry and X-ray diffraction are used, whereas indirect method can include measuring the changes in some physical and mechanical property of the material such as stress, electrical resistivity, hardness and density.

Although due to recovery, a lot of macroscopic properties are affected such as electrical resistivity, hardness, flow stress, density etc., but from engineering point of view double hit test and stress relaxation test are more popular as they output flow stress evolution which being an engineering parameter can be directly used in engineering design or for analysis can be easily converted to dislocation density using Forest Hardening type relation:

$$\sigma = \sigma_y + M\alpha\mu b\sqrt{\rho} \qquad \text{Eq. 1(a)}$$

$$\sigma_D = \sigma - \sigma_y \qquad \text{Eq. 1(b)}$$

where σ is the flow stress, σ_y is the yield stress, σ_D is stress due to dislocation, μ is the shear modulus, b is burgers vector, ρ is dislocation density, α is a constant of the order of 0.15 and M is the Taylor factor which is 3.1 for FCC material [23].

In principle, the results obtained through them can have marked interference from recrystallization; hence in order to avoid it, recovery studies are only done under T_{NR}

(Temperature of No Recrystallization) or for short times above that temperature. A brief explanation of these two processes follows:

2.1.1.1. Double deformation test

In double deformation test, recovery kinetics can be measured by indirectly monitoring the degree of softening measured from an interrupted mechanical test. The basic procedure of this is that the sample after being given a specific heat treatment is deformed to a fixed strain after which the stress is removed. After holding for a definite amount of time the sample is deformed again to measure its new yield stress. The shape of the second deformation curve is strongly dependent on the softening occurring between the inter-pass times. A typical stress strain curve is shown in **Figure 5**.

From the stress strain diagram obtained, varieties of methods are available to analyze them quantitatively e.g. back extrapolation method, mean flow stress and offset method [24, 25] (see **Figure 6**).

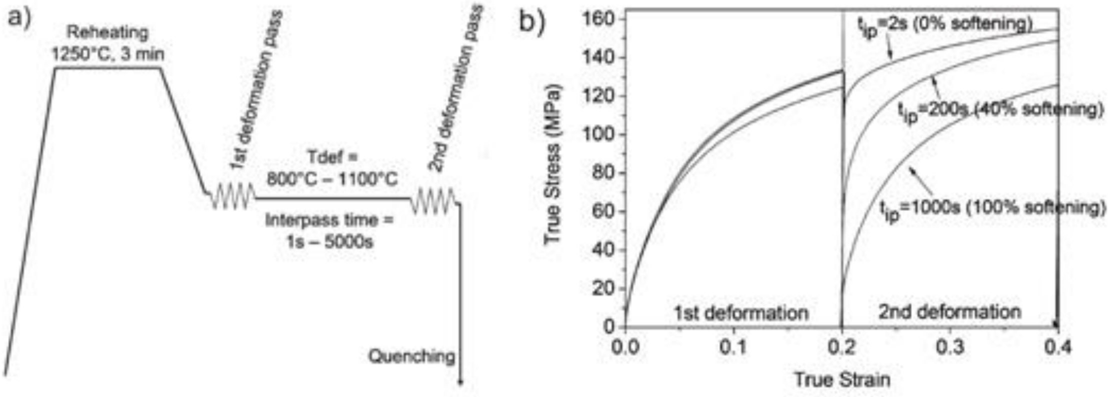

Figure 5: (a) Procedure of the double deformation test and (b) resulting stress-strain curves from the double deformation test used to calculate the fraction of softening during the inter-pass time [24]

The main drawback of this method (double deformation) is that it's quite tedious, because for every data point a new sample is required, which has to be given the same thermo-mechanical treatment.

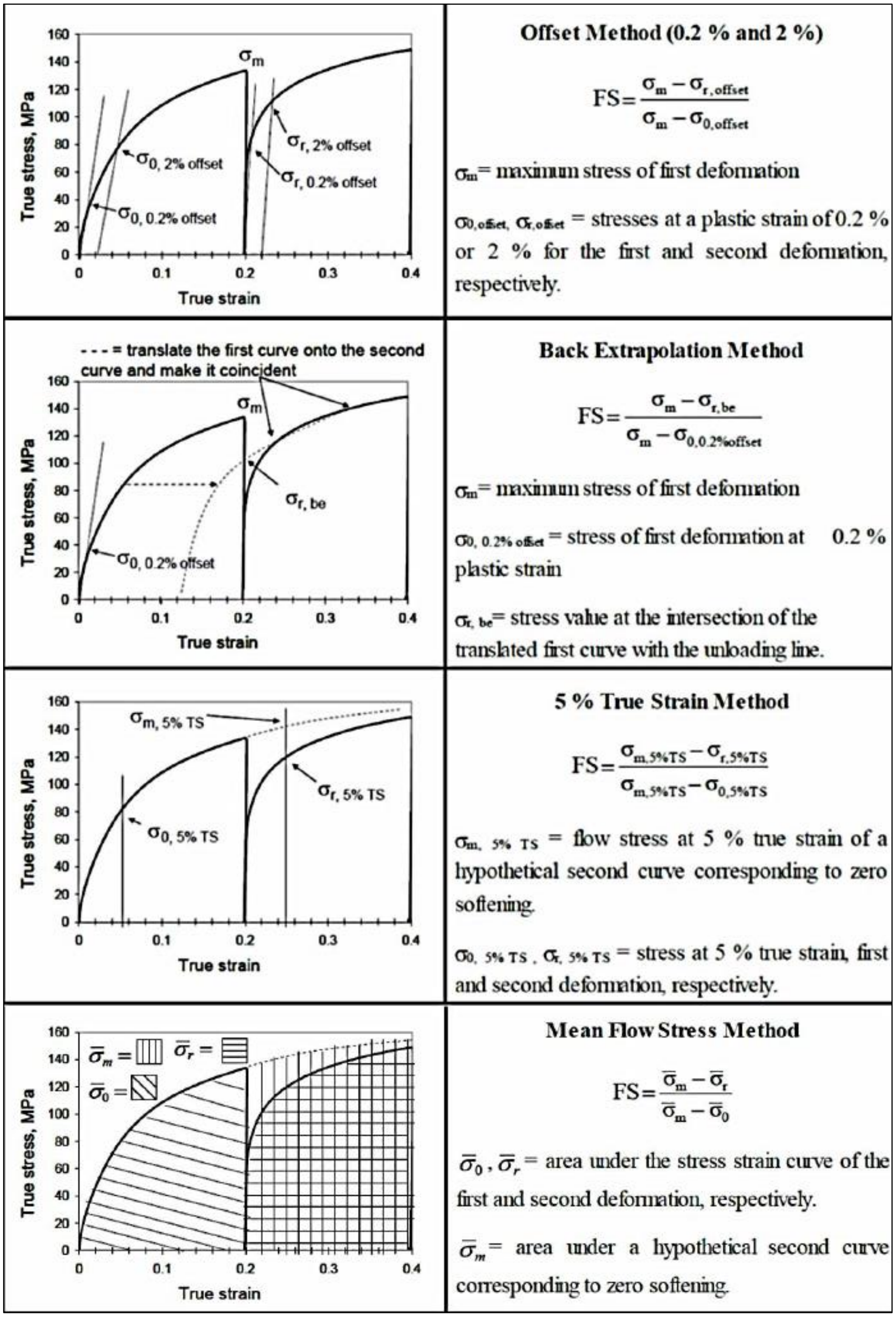

Offset Method (0.2 % and 2 %)

$$FS=\frac{\sigma_m-\sigma_{r,offset}}{\sigma_m-\sigma_{0,offset}}$$

σ_m= maximum stress of first deformation

$\sigma_{0,offset}$, $\sigma_{r,offset}$ = stresses at a plastic strain of 0.2 % or 2 % for the first and second deformation, respectively.

Back Extrapolation Method

$$FS=\frac{\sigma_m-\sigma_{r,be}}{\sigma_m-\sigma_{0,0.2\%offset}}$$

σ_m= maximum stress of first deformation

$\sigma_{0,\ 0.2\%\ offset}$ = stress of first deformation at 0.2 % plastic strain

$\sigma_{r,\ be}$= stress value at the intersection of the translated first curve with the unloading line.

5 % True Strain Method

$$FS=\frac{\sigma_{m,5\%TS}-\sigma_{r,5\%TS}}{\sigma_{m,5\%TS}-\sigma_{0,5\%TS}}$$

$\sigma_{m,\ 5\%\ TS}$ = flow stress at 5 % true strain of a hypothetical second curve corresponding to zero softening.

$\sigma_{0,\ 5\%\ TS}$, $\sigma_{r,\ 5\%\ TS}$ = stress at 5 % true strain, first and second deformation, respectively.

Mean Flow Stress Method

$$FS=\frac{\bar{\sigma}_m-\bar{\sigma}_r}{\bar{\sigma}_m-\bar{\sigma}_0}$$

$\bar{\sigma}_0$, $\bar{\sigma}_r$ = area under the stress strain curve of the first and second deformation, respectively.

$\bar{\sigma}_m$= area under a hypothetical second curve corresponding to zero softening.

Figure 6: Overview of the commonly used method to calculate softening from double deformation test (Nb microalloyed steel, Tdef = 1000°C, t_{ip}= 200s)[26]

2.1.1.2. Stress relaxation test

Though the double deformation method explains recovery progress quite efficiently, it suffers from the drawback that it needs lot of experiments to get a softening curve. The method of stress relaxation provides an opportunity to measure the complete softening kinetics with one sample.

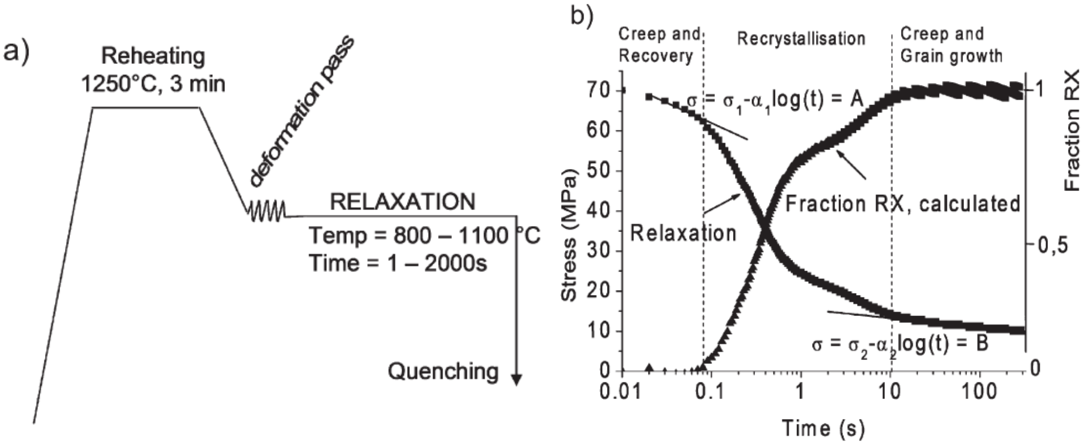

Figure 7: (a) Procedure for stress relaxation test and (b) illustration of the analysis of a stress relaxation test. [24]

The sample after being given the necessary heat treatment cycle is deformed. After a definite amount of strain, at a given strain rate the displacement in the sample is fixed and decay in stress with time is recorded. This gives the recovery kinetics. Care has to be taken in both the methods, that evolution of flow-stress is affected by microstructural events such as recovery, recrystallization, precipitation and grain coarsening and hence suitable design of experiment is needed to study any one of these mechanisms.

2.1.2. Effect of strain, solute and temperature on recovery kinetics

Strain: Increase in strain leads to increase in dislocation density. . Since the driving force for recovery is dislocation density this leads to increased recovery kinetics with increase in strain. In microalloyed steels, increase in recovery kinetics is manifested in terms of more definitive sub structure.

2.1.2.1. Effect of Solutes on recovery

Dislocations create strain field in the matrix and as such are potential sites for solute to segregate, thus relieving stress. Solutes may influence recovery by their effect on the stacking fault energy [27], by pinning dislocations both within cells and sub-grain boundaries, and by affecting the concentration and mobility of vacancies[12]. The migration of subgrain boundary generally occurs by climb of dislocation comprising the boundary at a rate controlled by the diffusion of solutes [13]. Solute pinning of dislocations will inhibit both dynamic and static recovery, resulting in a higher stored energy than for a solute-free material, [12].

Study done by Zadeh et al.[28] on two steels with varying Nb content has revealed that for the same temperature the one with lower Nb exhibit higher recovery kinetics. One of the most comprehensive experimental work done, to investigate the effect of micro alloying elements on recovery was done by Yamamoto et al. [29]. They used a series of micro alloyed steels and decarburized it so as to eliminate the effect of precipitates and then evaluated softening kinetics using double-deformation test for a range of temperatures

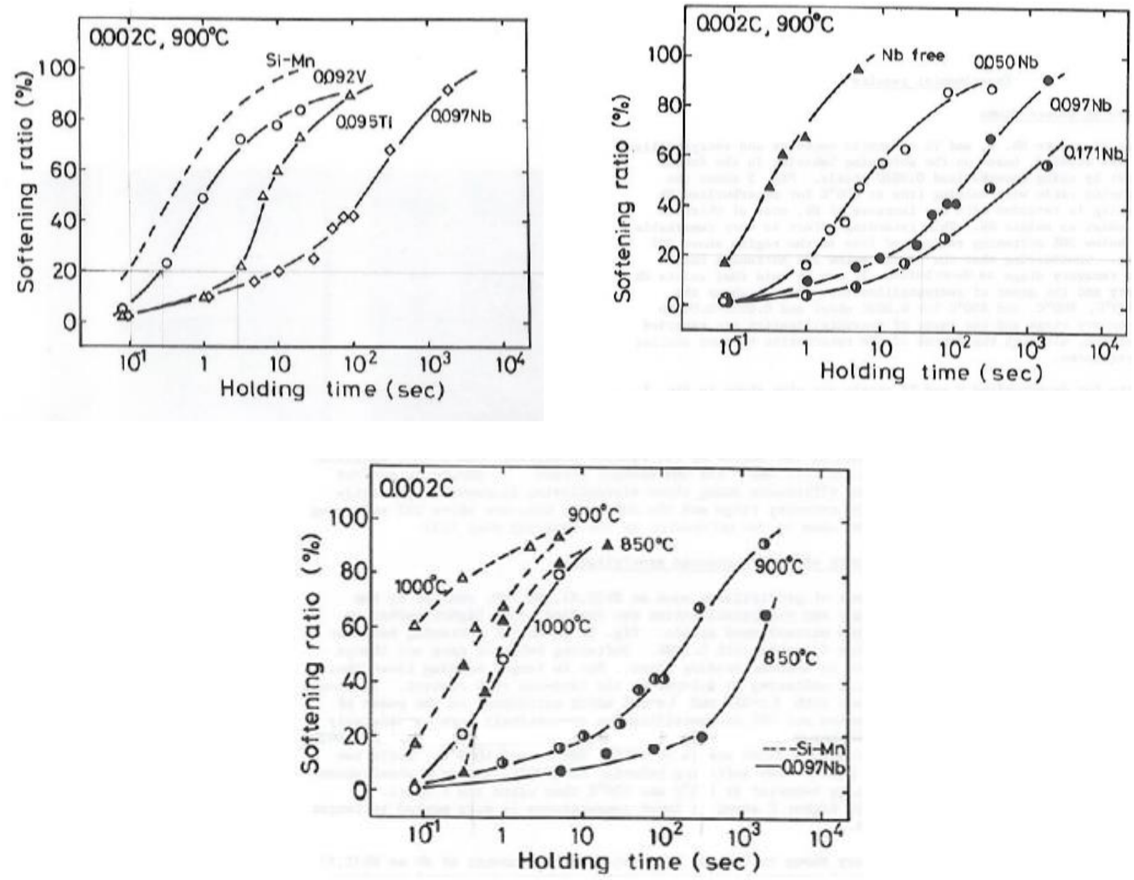

Figure 8: (a) Effect of various solutes on softening kinetics, (b) effect of solute content on softening kinetics, (c) Effect of temperature on softening kinetics. The first 20% softening is solely due to recovery and hence can be interpreted in terms of effect on recovery. [29]

Important observations coming out of Yamamoto's work [29] (**Figure 8**) are as follows:

The microalloying elements (Nb,Ti and V) significantly retard the kinetics of recovery. The retardation increases in the order V<Ti<Nb. This effect is clearly visible in **Figure 8**(a). The initial softening about 20% is solely due to recovery and is confirmed from the metallographic observations[29]. As such, time for 20% softening (t_{20}) is a convenient way to compare recovery kinetics. The degree of retardation depends upon the solute content. From **Figure 8**(b) increase in solute Nb leads to increase in t_{20}.

The effect of solute concentration on recovery changes as a function of temperature. This effect is obvious in **Figure 8**(c) where the slope of the softening curve changes with respect to temperature. In case of Nb steels at higher temperature the sub-grain formation and growth is slowed down due to solute drag effect of Nb and at lower temperatures the Nb(C,N) precipitates retards recovery [28-30].

The above effect was also confirmed by McElroy [31] who proposed that solute elements interact with dislocations either by altering the SFE or by segregating to dislocation and pinning them. Nb and Ti significantly affect the stacking fault energy (SFE) of austenite[32]. They found that the addition of 1% Nb to a 15-15 stainless steel lowered SFE by 20mJ/m^2. However in micro-alloyed steel Nb is usually less than 0.1 wt%, due to which effect of micro-alloys on Stacking Fault Energy is not expected to be significant. Nes [22] mentioned that in case of thermally activated glide, solutes alter the jog spacing causing the apparent activation energy for recovery dependent on both the initial dislocation density and solute misfit.

2.1.2.2. Effect of Particles on Recovery

Second phase particles may be present before recovery commences or they may precipitate during recovery. In both the cases they affect recovery kinetics prominently.

In **Figure 9** the initial 20% can be attributed to recovery. Comparing the dotted lines (precipitate free) with the solid ones (with precipitate), one observes more deviation at lower temperatures which highlight the inverse relationship between recovery and precipitation kinetics.

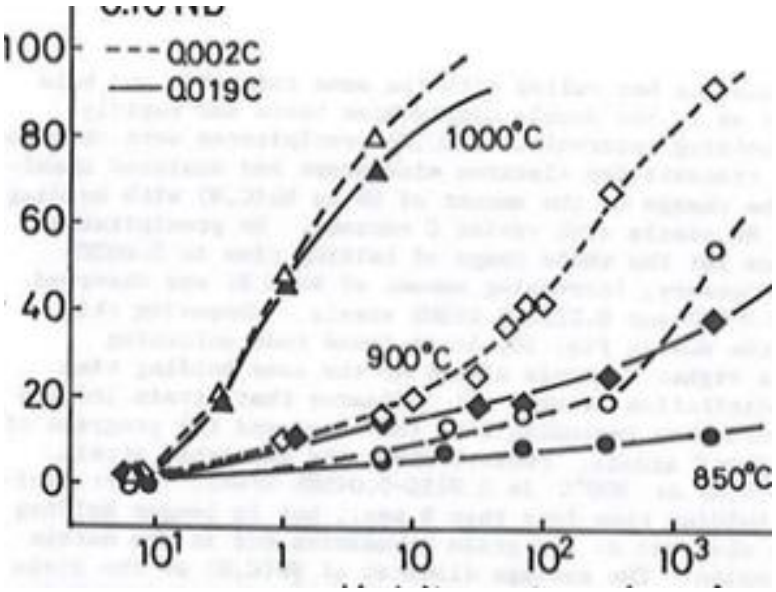

Figure 9: Effect of particles on recovery kinetics[29].

Second phase particles may affect recovery in several ways. Humphreys [12] mentions that during the initial stage of recovery when dislocations rearrange themselves to form low angle boundaries, the second phase particles can pin these individual dislocations thus preventing their rearrangement, hence slowing down recovery. He further states that if the inter-particle distance is small and comparable to the scale of dislocation network then they will inhibit recovery but in practical cases this rarely occurs and hence it is not investigated much.

2.1.3. Recovery Models

Modeling recovery is difficult mainly because of the large number of dislocations involved (~10^{15} /m^2) and their heterogeneous distribution. In case of large deformation dense dislocation networks form which make direct observation of microscopic mechanism difficult. This leads to modeling of strain energy distribution (associated with dislocations) and the individual processes viz. cross-slip, glide and climb at a scale of both inter-grain (50-500μm) and intra–grain (1-10μm). The correlation between the microstructure evolution at subgrain level, multi-granular level and the macroscopic mechanical properties is of paramount importance to engineers.

There are two most commonly reported isothermal relations in literature which are often referred to as logarithmic or power law kinetics. Logarithmic kinetics is commonly observed in micro alloyed steels at intermediate annealing temperatures ($\mathrm{T_m}/2$). The logarithmic kinetics occurs when dislocation glide or solute drag is the rate control step.

The decay of flow stress is generally found to follow either logarithmic or power law kinetics[12]

$$\sigma_D = c_1 - c_2 \ln(t) \qquad \text{Eq. 2(a)}$$

$$\sigma_D = c_3 - c_4 (t)^{-m} \qquad \text{Eq. 2(b)}$$

where, C_1, C_2, C_3 and C_4 and m are constants and vary with material and processing condition. Friedel et al. [33] concluded that the logarithmic decay equation is only valid in low temperature anneals of strongly strained fcc metals the mechanism being that of thermally activated cross-slip. Maruyama et al. [34] suggested that logarithmic kinetics could be attributed to glide control or solute drag control. Power law kinetics has been found to be mainly observed in polycrystals [35, 36].

As recovery comprises of growth of cellular structure and decay of dislocation density inside the cellular structure, Nes [22] came up with a two parameter model to describe recovery.

$$\sigma(t) = \sigma_i + M\mu b\left[f_s\alpha_1\sqrt{\rho(t)} + f_h\alpha_1'\frac{1}{\sqrt{\delta(t)}}\right] \qquad \text{Eq. 3}$$

where σ_i is frictional stress, δ is sub-grain size and α_1, α_1' are constants.

The model assumes that the decay in flow stress is due to the contribution from subgrain boundary and the dislocation density inside those sub-grains. In case of high SFE material the inside of sub-grains gets cleaned quickly and the progress of recovery is controlled by the coarsening of sub-grains. Sellars and coworkers [37] have used a single parameter model (subgrain size) and have correlated it to strength in Al alloys. The drop in flow stress is analogous to Hall-Petch relationship of decay in yield stress due to increase in grain size. In a realistic sense to apply this model for microalloyed austenite, as it has an intermediate SFE one need to have a separate model for both dislocation density decay in the cell structure and the increase in cell/sub-grain size. Also as the sub-grain grows it becomes more misoriented increasing the boundary mobility, which is not captured in the above model. The volume fraction of cell size and grain boundary thickness changes with the progress of recovery which is difficult to quantify.

Verdier et al.[38] found the yield stress decay to be logarithmic for small strains irrespective of the cellular microstructure evolution. Hence he concluded that the strength decay can simply be modeled by a single internal variable (average dislocation density), which will be related via a Forest Hardening type relationship (Eq. 1).

The model proposed assumes that the internal stress relaxation is due to thermally activated dislocation rearrangement and annihilation. The plastic relaxation rate $\dot{\varepsilon}$ is related to change in internal stress σ_d by:

$$\frac{d\sigma_d}{dt} = -\dot{\varepsilon}E \qquad \text{Eq. 4}$$

where E is Young's modulus. The relation between $\dot{\varepsilon}$ and dislocation density is given by Orowan Law:

$$M\dot{\varepsilon}_p = \rho b\bar{V} \qquad \text{Eq. 5}$$

where M is the Taylor factor, ρ is the dislocation density and $\bar{V}$ is the average dislocation velocity. The dislocation velocity is thermally activated and is influenced by σ_d as per;

$$\bar{V} = b\nu_D exp\left(-\frac{U_a}{k_b T}\right) sinh\left(\frac{\sigma_d V_a}{k_b T}\right) \qquad \text{Eq. 6}$$

where ν_D is the Debye frequency. Finally the evolution of flow stress is given by an equation of the following form:

$$\frac{d\sigma_d}{dt} = -\frac{64\sigma_d^2}{9M^3\alpha^2 E} exp\left(-\frac{U_a}{k_b T}\right) sinh\left(\frac{\sigma_d V_a}{k_b T}\right) \qquad \text{Eq. 7}$$

In this equation U_a is activation energy and V_a is activation volume.

The value of activation energy ranges from that of pipe diffusion to bulk diffusion. As recovery is dislocation rearrangement hence, recovery kinetics will be affected by different mechanism like cross-slip, climb or solute drag, which in turn is represented by activation energy in the present model.

The activation volume V_a is related to the spacing of the pinning centers. The activation volume corresponds to an activation length of V_a/b^2 which varies between 20-40b. This activation length is the average measure of the distance between two pinning centers. These centers may be jogs on a screw dislocation as in the case of glide, or solute atoms in case of solute drag. Hasegawa et al. [39] has found that with change in pre-strain levels the cell walls tighten and thus changes the activation spacing. Fitting the experimental recovery data using Verdier model a trend can be observed for activation volume as a function of Nb content and relaxation temperature **Figure 19**. The trends follows the underlying physical understanding, that is to say that as the niobium concentration increases the distance between pinning centre(Nb solute atoms) decreases. For the same niobium concentration increasing the temperature increases the mobility of Nb atoms making them less effective pinning centres resulting in decrease in activation volume.

2.2. Precipitation

The micro-alloying elements which remain in solution at high temperatures start precipitating at low temperature. Nb, Ti and V are the most commonly used micro-alloying elements and upon cooling they form carbides, nitrides and/or carbonitride. A lot of research have proved beyond doubt that addition of micro alloying elements (Ti, Nb and V) in steels significantly alters the mechanical properties[4]. These fine precipitates not only harden the steel but significantly delay/stop recrystallization by Zener drag allowing for enhanced strain accumulation in controlled rolling [2]. Beside delaying recrystallization these micro-alloying precipitates also prevent grain growth during heat treatment of the rolled product [4]. Due to all these factors precipitation has been examined in detail by many researchers [40-42]. From a strengthening perspective the size distribution and volume fraction of the precipitates are most important. To quantify the size distribution and volume fraction it becomes imperative to investigate the composition and time temperature transformation curves of these micro-alloying precipitates. These two are discussed in later sections. By now a variety of techniques have been developed which are able to model precipitation fairly accurately. These models range from simple empirical equations to fairly complex MD simulations which are able to explain the process in quite detail [43-53]. All these models can be sub-grouped into two categories. The first category deals with models which describe precipitation in much detail, with very few assumptions and are more physically based thereby providing better understanding of the underlying processes. In this category, the Kinetic Monte-Carlo [43-45] and the cluster dynamics techniques [46-48] are able to describe all stages of precipitation (from nucleation to coarsening) with a precise description of the kinetics of the processes. However these methods do have their own set of restriction which limits their applicability such as high CPU time. The second class of model are simple models which aren't as accurate as the first class but nevertheless offers significant advantage in areas where the first one lacks such as computer processing time, scalability due to which these models are widely used in describing practical situations[49-52]. They evaluate nucleation and growth from differential equations of the classical laws in a continuous way.

2.2.1. Composition

Niobium forms carbides and nitrides in HSLA steel which have very low solubility in austenite. It is a nonstoichiometric compound and is usually represented as NbC_x. Since microalloyed steels almost always contain other carbide and nitride formers the stoichiometry of NbC and NbN is not ideal and will depend upon the activity of interstitials. Balasubramanian and Kirkaldy [53] have proposed a regular solution model to calculate the composition. Their calculation shows x in NbC_x vary between 0.87-0.98. Other researchers have found it to vary from 0.75 to 0.98 [54, 55]

Due to similarities in electronic configuration of nitrides and carbides ($R_N \approx 0.67Å$ and $R_C \approx 0.77Å$), the physical properties of microalloying carbides and nitrides are quite similar. The carbides and nitrides form a solid solution among themselves leading to variation in exact compositions. Palmiere et al. [56] have summarized a number of studies done previously on the composition of these precipitates using atom probe spectrometer. The advantage of this technique over others is that it involves a direct observation and analysis of the precipitates and hence enables a more realistic estimate. Furthermore Dutta et al. [57] reported that low nitrogen steels revealed precipitates ranging from $NbC_{0.8}$ to stoichiometric NbC, while high nitrogen steels exhibited carbonitrides of the compositions ranging from $NbC_{0.67}N_{0.33}$ to $NbC_{0.8}N_{0.07}$.

Perez et al.[58] found that for low driving force niobium nitride and niobium rich carbonitrides form first and later carbon is absorbed into the precipitate giving the average composition as $NbC_{0.59}N_{0.38}$. Similar observation of distinct changes in composition was Perrard et al. [42] using TEM.

To calculate the solubility product of niobium carbonitrides Gladman [4] assumed it to be an ideal solution of NbC and NbN and calculated C/N ratio from the solubility product data of niobium carbide and niobium nitride in austenite. Consequently it was later shown that the ratio changes with change in niobium, carbon, nitrogen and austenizing temperature.

Xu et al. [59] used a Monte-Carlo method to determine the exact composition of the carbides. Nb was assumed to be present randomly on one sub-lattice whereas C and N are randomly mixed on the other sub-lattice as suggested by other researchers [60, 61]. Xu [59] reported that the composition of carbides does change with deformation temperature and solute niobium content, which the regular solution model was quite able to predict.

Similar behavior of varying composition was observed in vanadium microalloyed steels by Maugis et al. [62] wherein he argues that the ratio of C/N in V(C, N) is a function of alloy chemistry and thermal cycle.

2.2.2. Solubility Product

Solubility limit is defined as the maximum amount of solute which will remain dissolved in solvent (matrix) at a given temperature. Over a period of time, researchers have proposed a variety of equations for Nb/NbCN system, which differ slightly in their results. A summary of a list of solubility product equations reported in literature is given in Appendix 3. The differences in solubility product equations can be attributed to differences in measurement technique (sensitivity). Irvine's equation [63] is one of the most widely used

$$\log[Nb]\left[C+\frac{12}{14}N\right]=2.26-\frac{6770}{T} \qquad \text{Eq. 8}$$

Recently Palmiere et al. [56] have published a different solubility product equation based upon atom probe studies

$$\log[Nb]\,[C]=2.06-\frac{6770}{T} \qquad \text{Eq. 9}$$

Chemical driving force for precipitation is expressed as supersaturation as shown in Eq. 10 the others being surface energy and strain.

$$k_s = \frac{\log[Nb]\left[C + \frac{12}{14}N\right]}{2.26 - \frac{6770}{T}} \qquad \text{Eq. 10}$$

Higher the supersaturation ratio higher will be the thermodynamic potential for precipitation.

2.2.3. Effect of Other alloying element

In microalloyed steels, apart from the microalloying elements other elements such as Mn, Ni, Cr, Si etc. are also present in significant amounts. These elements themselves do not form carbides/nitrides but nevertheless they alter the activity of other species present in the matrix. Although the interactions are quite weak on per atomic basis compared to Nb, Ti or V, but due to their high concentrations in microalloyed steels (upto 2%) their effect cannot be ignored.

Koyama et al.[64] have experimentally determined the influence of other alloying elements on the solubility product of NbC/NbN. In their published equation only one alloying element is considered at a time, for solubility product calculation. Usually more than one alloying elements are present in microalloyed steels and hence direct application of Koyama's equation is not accurate enough.

For dilute solutions Wagner Interaction Parameters can be used to incorporate the effect of other alloying elements [40, 49]. For Fe-M-X-K system, where X is the interstitial, K is the alloying element and M is the microalloy.

$$ln\, a_M^\gamma = \left[ln\, a_M^\gamma\right]_{K=0} + \sum \varepsilon_M^K X_K^\gamma \qquad \text{Eq. 11(a)}$$

$$ln\, a_X^\gamma = \left[ln\, a_X^\gamma\right]_{K=0} + \sum \varepsilon_X^K X_K^\gamma \qquad \text{Eq. 11(b)}$$

where, K (K=1, 2, 3...) is the other alloying element. The first term ($\left[ln\, a_M^\gamma\right]_{K=0}$, $\left[ln\, a_X^\gamma\right]_{K=0}$) represents the activity of the microalloying element in absence of other alloying element K, X_K^γ is the mole fraction of element K and ε_M^K is the Wagner interaction parameter between M and K. Accordingly the solubility product equation when M=Nb and X=C in austenite in the presence of other alloying element will become

$$\log[\%Nb]\,[\%C] = \{\log[\%Nb]\,[C\%]\}_{K=0} - \sum_{K=1}^{n} \left\{(\varepsilon_{Nb}^K + \varepsilon_C^K)[\%K]\frac{A_{Fe}}{230.3\, A_K}\right\} \qquad \text{Eq. 12}$$

where, A_{Fe} and A_K are the atomic weight of Fe and K respectively, the concentration [%K] is also in weight percent. Hence if the Wagner interaction parameters are known for each element $\varepsilon_{Nb}^K, \varepsilon_C^K$ the overall solubility product can be calculated using the above equation. Estimates of Wagner interaction parameters are tabulated in Appendix 4. Care should be taken in applying the above equation as it is only valid for dilute solutions and proper higher order interaction parameters need to be applied when applying it to non-dilute solutions.

2.2.4. Precipitation kinetics

A large number of researchers [15, 60, 65-70] have studied the precipitation kinetics of micro-alloying elements and their effect on microstructure. Results of the studies conclusively prove that pre-deformation significantly alters the precipitation kinetics [66, 71]. These studies have focused on studying precipitation kinetics as a function of steel composition, initial grain size, deformation temperature, amount of strain, strain rate and type of deformation. These studies employ different methods to measure precipitate size and volume fraction hence a direct comparison of them becomes difficult.

The critical supersaturation level for the nucleation of precipitates in undeformed austenite is expected to be high due to reduced nucleation sites. However the introduction of strain provides sites for nucleation leading to precipitation at lower supersaturation ratios typically between 5 and 7.7 [72, 73], where supersaturation refers to the thermodynamic driving force available for precipitation (Eq. 10). Precipitation mostly occurs on dislocations, grain boundaries and other microstructural defects. The main reason behind this is the large misfit of the precipitates to that of the FCC lattice. The misfit is greatest in case of niobium precipitates and the least for vanadium precipitates. In deformed austenite, dislocations along with grain boundary are preferred nucleation sites. However in typical condition grain boundary volume fraction is usually much less than total dislocation volume fraction hence, initial dislocation density and their evolutions are essential for modeling precipitate evolution.

In order to predict niobium carbonitride precipitation during hot working it becomes imperative to investigate/predict precipitation start temperatures for different deformation conditions. Researchers have done this by using a nucleation model coupled with solubility product equations. Solubility product of Nb(C, N) as a function of chemistry and temperature has been investigated by many groups. Notable among them are the works of Sharma and Koyama [54, 64]. Sharma's work in particular is indispensible because of the fact that they have investigated effect of other elements (Cr, Mo, Si) on the solubility product of NbC and NbN in austenite.

2.2.4.1. Precipitate Nucleation

The most prominent nucleation sites are dislocation and grain boundaries [70]. For the case of coarse grained austenite (50 µm), the amount of grain boundary precipitates is less than 1% of total number of precipitates [66]. Some studies [74, 75] have suggested grain boundary precipitation as a modified form of precipitation on extrinsic dislocations.

Dutta and Sellars [66] were one of the pioneers in this field and proposed a semi-empirical model based upon data mining and classical nucleation theory to predict the start of precipitation in Nb microalloyed steels as a function of process variables and composition.

$$t_{5\%} = A[Nb]^{-1}\varepsilon^{-1}Z^{-0.5} * exp\frac{270{,}000}{RT} * exp\frac{B}{T^{3}(\ln k_{s})^{2}} \qquad \text{Eq. 13}$$

where, $t_{5\%}$ is the time for 5% precipitation, [Nb] is the solute Nb concentration, ε is the true strain Z is the Zener-Holloman parameter, T is the absolute temperature, k_s is the super saturation ratio, A and B are empirical constants.

Liu and Jonas [68] treatment of nucleation driving force was quite comprehensive, it was calculated from a thermodynamic database as a function of chemical composition. They assumed that a critical nucleus forms when solute clusters, during solution treatment.

$$\frac{dN}{dt} = \frac{\rho D_0 X_{Nb}}{a^3} exp\left(-\frac{Q}{RT}\right) exp\left(-\frac{\Delta G^*}{kT}\right) \qquad \text{Eq. 14}$$

where, D_0 and Q are the frequency and activation energy for the diffusion of Nb in austenite and R is the gas constant. The above equation gives nucleation rate which could be integrated to give the time evolution of nuclei.

2.2.4.2. Growth and Coarsening

In early precipitation kinetics models [76, 77] one of the key problems was lack of a reliable nucleation model which tended to give a variable growth kinetics depending upon the initial nucleation density. A small strain applied at high enough temperature is sufficient to accelerate precipitation by orders of magnitude in time with respect to undeformed austenite [78, 79].

As discussed earlier, the Liu and Jonas[67] model was pioneering. It was developed for Ti(C, N) precipitation in austenite but they argued that the model can be extended to other precipitates precipitating heterogeneously. Precipitation was argued to occur in three distinct stages. (i) Nucleation and Growth according to parabolic law (ii) Nucleation Site saturation followed by only growth. (iii) Coarsening/Ostwald ripening of the precipitates. This model follows diffusion controlled growth law hence square of diameter is linearly proportional to time in the initial stages. The precipitate coarsening was explained using a Lifshitz-Wagner equation:

$$\bar{r}^n - \bar{r_0}^n = Kt \qquad \text{Eq. } 15$$

where, n depends upon the coarsening mechanism. n=3 is for bulk diffusion, n=4 for grain boundary diffusion, n=5 if dislocation diffusion is the rate controlling step. Later on the model was further extended by Park and Jonas [69] to incorporate precipitation under continuous cooling using the additivity principle. This model was the first attempt on predicting precipitation finish time. Essentially, it used a JMAK type equation where the constants were calculated from solute concentration gradient. Solute concentration gradient is the change in solute concentration from matrix to the precipitate core along the interface.

The next generation of precipitation models which came almost a decade later tries to explain the underlying physics of the problem. Among these Dutta and Sellars [15] , Fujita and Bhadeshia [41] and Deschamp and Brechet [80] are worth mentioning. In these models, the concept of time evolution of precipitates was presented and covered all three aspect of precipitation viz. nucleation, growth and coarsening. Nucleation was modeled using classical nucleation theory. The roles of bulk diffusion and pipe diffusion in growth and coarsening were also incorporated. Dutta and Sellars [15] assumed heterogeneous precipitation occurring exclusively on dislocations and accelerated coarsening occurring because of pipe diffusion. The model takes into consideration simultaneous growth and coarsening. The limitation of Dutta and Sellars model is that it’s too sensitive to dislocation density and for a correct estimation of precipitation kinetics needs a correct estimation of dislocation density. Further on Fujita and Bhadeshia [41] modeled growth and coarsening using concentration gradient at the interface the driving force of which is the concentration gradient along the interface. The model by Deschamp et al. [80] is quite comprehensive in its approach to explain the heterogeneous precipitation kinetics occurring on dislocations and their further growth and coarsening. This model assumes nucleation and growth to occur simultaneously. Accelerated coarsening by accelerated diffusion of solute atoms along the dislocation network is also taken care of. The model was originally made and validated for Al-Zn alloys but was later shown by Zurob et al. [5] to work in micro-alloyed austenite as well.

2.3. Recrystallization

Recrystallization as a term is a misnomer. It was originally believed that after deformation the loss of ductility is due to the destruction of crystalline structure, which after annealing is restored due to restoration of crystalline structure, hence the process name re-crystallization [81]. Recrystallization has a drastic effect on the overall mechanical properties of a material. Humphreys [12] defines it as a process wherein deformed grains are replaced by a new set of strain free grains. Due to this progressive decrease in deformed grains there is a drastic reduction in overall dislocation density which leads to a decrease in yield strength of the material and increased ductility. These un-deformed grains first nucleate and then they grow so as to consume the entire structure of deformed grains. The overall recrystallization kinetics is governed by both the nucleation rate and growth rate of each nucleus. Doherty [82] mentions that industrially, recrystallization is very important because it softens the material in order to restore ductility thus allowing further processing. Recrystallization after deformation is the only metallurgical process to refine grain size, shape and texture in the case of steels. Compared to recovery, recrystallization leads to a more significant decrease in strength and increase in ductility. As per Burke et al. [83] the key parameters affecting static recrystallization are pre-strain, annealing temperature, starting grain size, solute content, precipitate volume fraction and size. This will be discussed in further detail in the subsequent sections.

2.3.1. Nucleation of recrystallization

Unlike recovery which is a continuous process, recrystallization occurs in discontinuous manner i.e there is a definite incubation time after which nucleation takes place followed by growth of those nuclei. However in a classical thermodynamic sense nucleation of recrystallization doesn’t occur. The nuclei do not originate from an other phase rather than it forms from a pre-existing cells/sub-grains once a certain growth criterion has been fulfilled [82].

Among all the nucleation mechanisms mentioned in literature such as particle stimulated nucleation, nucleation due to sub-grain coarsening and strain induced boundary migration (SIBM) [12], in the present context of static recrystallization in low strain high temperature micro-alloyed steels, researchers have agreed that SIBM is the dominant mechanism [13, 84, 85].

This mechanism takes into account the presence of pre-existing grain boundaries. After deformation the substructure developed tends to coarsen due to recovery. The sub-grains adjacent to the boundaries when coarsened sufficiently so as to overcome the capillarity drag effects bulges in the adjacent grain as shown in **Figure 10**. Once the sub-grains have coarsened substantially the bulging becomes thermodynamically favourably. The decrease in stored energy due to elimination of defects caused by the passage of the boundary is greater than the increase in total grain boundary surface due to bulging [86-88].

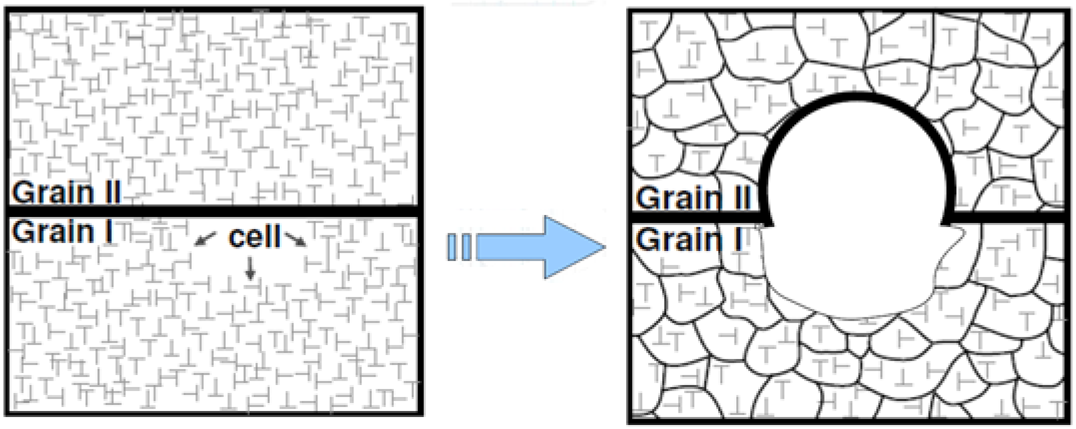

Figure 10: Schematic of the subgrain coarsening and boundary bulging associated with recrystallization nucleation[85].

Another interesting aspect of SIBM nucleation is that the orientation of the new grain is similar to the original grain from which it deformed as there is no new creation of a high angle boundary.

SIBM being the dominant mechanism was further supported by Hurley and Humphreys [84] who reported that SIBM is the dominant mechanism for total strains less than 0.7, though they did not investigate the effect of strain rate on nucleation mechanism. Later on Humphreys [89] further explains that the boundary migration in SIBM can be triggered by the presence of a stored energy gradient across the boundary. The boundary can move as a front (multiple sub-grain (SIBM) or as a boundary bulge adjacent to a single large sub-grain).

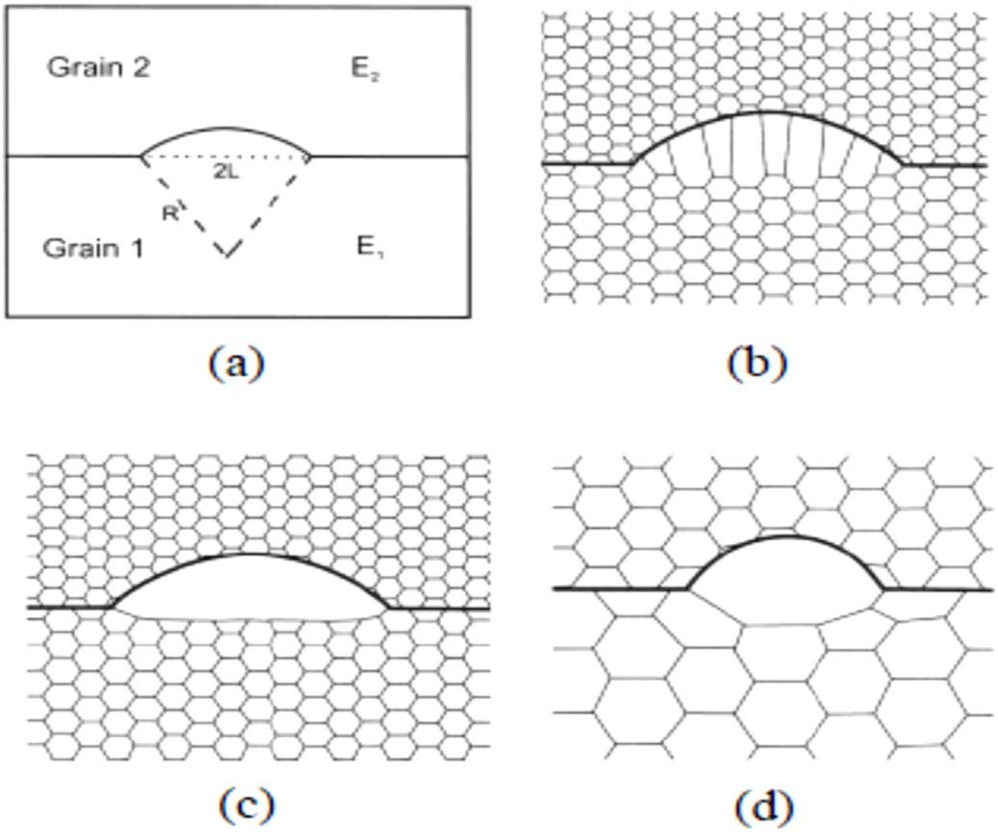

Figure 11: (a) SIBM of a boundary separating a grain of low stored energy (E1) from the higher energy one (E2), (b) dragging of the dislocation structure behind the migrating boundary, (c) the migrating boundary is free from the dislocation structure (d) SIBM originating at a single large subgrain [12].

Bate et al. [90] and then Hurley et al. [84] stated that in case of materials, with poorly developed dislocation cell structures and large stored energy differences SIBM occurs by well recovered sub-structures. In materials where there are a significant number of secondary phase particles, multiple SIBM will be favored. Stressing the effect of recovery on strain induced boundary type migration (SIBM) Hurley [84] states from the experimental study done on measuring growth rates of SIBM in aluminum, that there is an incubation time needed for nucleation to happen which proves that prior recovery is essential for SIBM to occur.

Lauridsen et al. [91] using X-ray diffraction published incubation time for recrystallization nucleation (**Figure 12**). A critical nucleus size of 1 micron has been assumed in this and it was shown that 80% of nucleation occurs before the material has recrystallized 10% which is close to site saturation, but the remaining 20% of the nuclei form much later. **Figure 12** shows, that nucleation does happen at later times possibly due to heterogeneous distribution of stored energy but it proves that the site saturation assumption is not true in all cases.

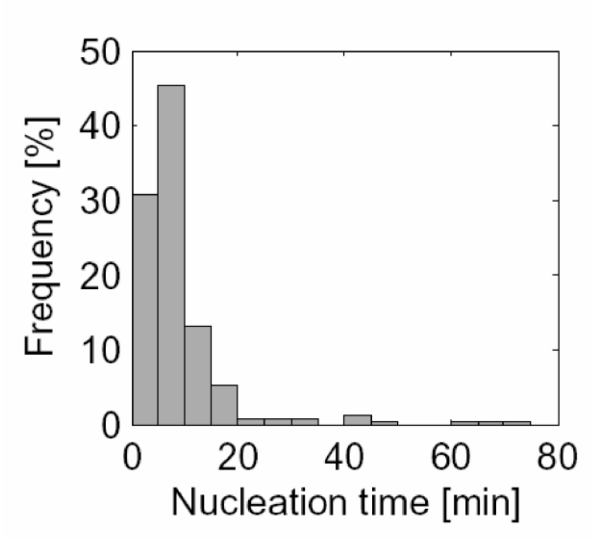

Figure 12: Distribution of nucleation times determined from 244 recrystallization curves by 3-d X-ray diffraction [91].

2.3.2. Growth Kinetics

Recrystallization proceeds with the migration of high angle boundaries. Once nucleation takes place the bulged high angle boundary sweeps across the deformed grains consuming the deformed substructure leaving behind a clean strain free microstructure. Migration of high angle boundaries is common to both recrystallization and grain coarsening, the key difference being the driving force for each process. Recrystallization is driven by dislocation density difference across the high angle boundary whereas grain coarsening is driven by the minimization of grain boundary surface energy.

From the theory of thermally activated growth, the relationship between boundary migration rate and driving force under non-equilibrium conditions is usually expressed as

$$V = M_{GB}\,(P - P_Z) \qquad \text{Eq. 16}$$

where, V is the boundary velocity, M_{GB} is a proportionality constant, also referred to as grain boundary mobility, P is the driving pressure and P_Z is the drag forces due to second phase particle.

In pure materials the mobility refers to the energy spent to transfer an atom from a shrinking grain to the growing grain across the grain boundary. Turnbull [92] derived the following expression from first principles for the grain boundary mobility in pure single phase materials.

$$M_{pure} = \frac{\delta D_{GB} V_m}{b^2 RT} \qquad \text{Eq. 17}$$

In this equation δ is the grain boundary thickness, D_{GB} is the grain boundary self-diffusion coefficient, V_m is the molar volume. b is the burger vector. The grain boundary diffusion has exponential dependence on temperature as shown below

$$D_{GB} = D_0 \exp\left(-\frac{Q}{RT}\right) \qquad \text{Eq. 18}$$

Because of the exponential dependence of diffusion on temperature, the mobility can be expressed in an Arrhenius type relationship as follows:

$$M_{GB} = M_0 exp\left(-\frac{Q}{RT}\right) \qquad \text{Eq. 19}$$

The experimental database on recrystallization **Figure 13** shows it proceeds with an incubation time. The incubation time relates to the time taken by subgrain to overcome the capillary barrier. Once nucleation starts migration of high angle boundaries (growth) continues until mutual impingement of recrystallized grains takes place i.e till all the new high angle boundaries meet. Distribution of recrystallized regions around the deformed grain is heterogeneous and impingement of nuclei occurs even at early times of recrystallization [81].

2.3.2.1. Solute Drag

It is well known by now that addition of small amount of solutes decreases recrystallization kinetics significantly [29, 93, 94]. The process by which solute elements reduce grain boundary mobility is termed as Solute Drag effect. The effect has been exummed in detail and modeled by a number of authors [95-97].

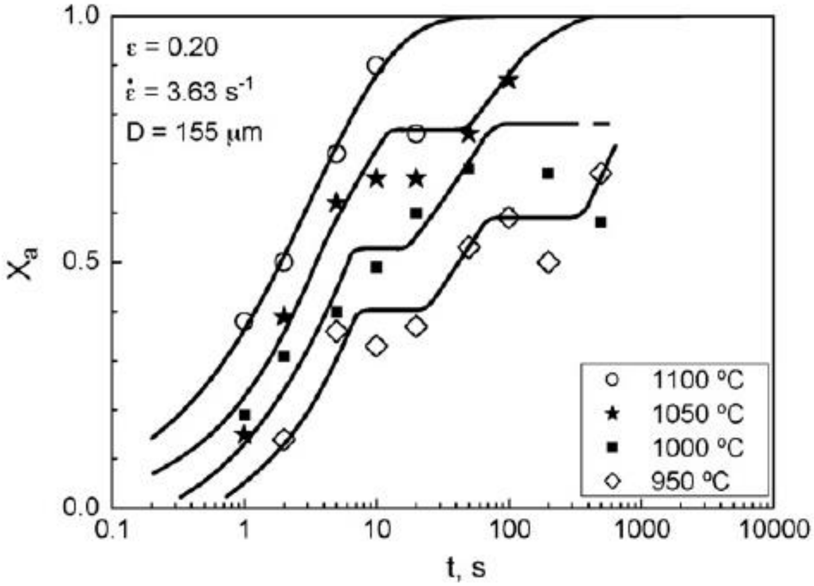

Figure 13: Plot of recrystallized volume fraction as a function of time for a steel containing 0.13 V and 0.48 C [98].

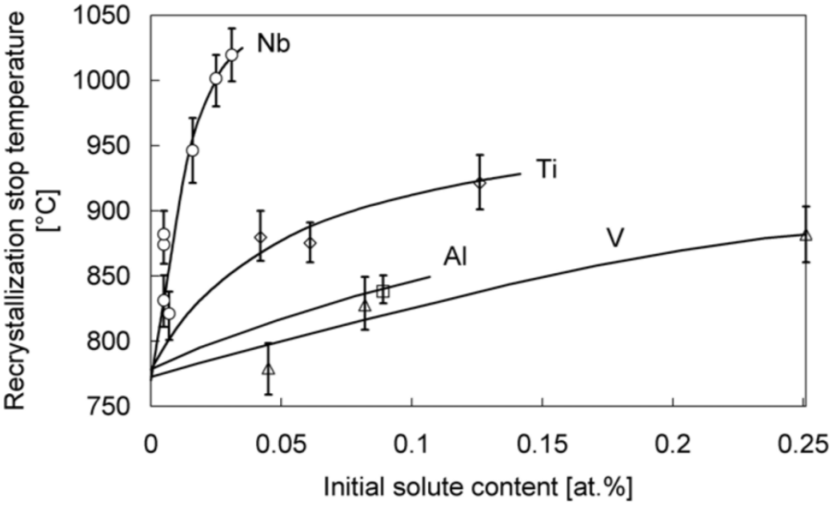

Figure 14: Effect of the initial solute content on the recrystallization stop temperature[94].

With reference to microalloyed steels, the microalloys at higher temperatures remain in solution and retard recrystallization kinetics through solute drag effect and at low temperatures precipitate which further pins the recrystallization. To study the effect of solute drag and to eliminate the interference with precipitates decarburization/denitriding experiments are usually carried on. One of the most comprehensive studies done was by Yamamoto et al. [29] where it was conclusively shown that niobium has the highest solute drag effect and vanadium the smallest among all microalloying elements, the same is shown in **Figure 15**.

Solute drag can be visualized in terms of dynamic segregation of solutes on a moving boundary so as to reduce their lattice misfit strain energy. In a stationary boundary of a single phase material the concentration profile of the solute ahead of the boundary and behind are exactly the same thus cancelling any attractive or repulsive force on the boundary. However as the boundary moves more solute atoms are left behind than are assimilated from the front due to their slow movement relative to the moving boundary thus creating an asymmetrical concentration profile. This leads to a drag force experienced by the boundary slowing down its advance. Solute drag is quite effective even in very small concentrations in reducing the boundary mobility thus reducing the growth kinetics of both recrystallization and grain coarsening.

For precipitate free case rearranging Eq. 16 yields:

$$P = \frac{V}{M_{GB}} \qquad \text{Eq. 20}$$

Or ,

$$P = f_i\, V \qquad \text{Eq. 21(a)}$$

$$f_i = \frac{1}{M_{GB,i}} \qquad \text{Eq. 21(b)}$$

f_i is the intrinsic friction of the material and relates to the energy needed to move an atom from one side of the boundary to the other side. Its reciprocal is the mobility of the boundary $M_{GB,i}$ which is the intrinsic boundary mobility in the absence of any solute.

Generalizing the above equation to include drag from other sources yields:

$$P = f_i V + P_{solute} + P_{zener} \qquad \text{Eq. 22}$$

where P_{solute} is the solute drag experienced by the boundary and P_{zener} is the Zener drag due to second phase particles.

P_{solute} can be independently calculated using Hillert's treatment of solute drag or can be expressed as Vf_{solute} where V is the boundary velocity and f_{solute} is solute drag force which can be calculated using Cahn [99] and by Lucke and Stewart treatment [96] (CLS model) of solute drag.

The migration of high angle boundaries in a single phase microstructure whether it is due to recrystallization or grain coarsening both approaches viz. Hillert's model or CLS model will give the same result. However in the case of phase transformation wherein there are different phases across the boundary, the stability of solutes becomes different across the two sides of the boundary due to which the solute drag formulation changes and only Hillert's model is applicable.

In the present work only Cahn's model is being used. Cahn's treatment of solute drag can easily be incorporated with the growth equations discussed in the previous section. Accordingly, for low velocity branch of Cahn's model (**Figure 15**) the solute drag is proportional to solute concentration

$$P_{solute} = \alpha\, C_0 \qquad \text{Eq. 23}$$

where, C_0 is the micro alloying element concentration in solution. α is a constant and is a function of both solute-boundary binding energy and cross-boundary solute diffusion coefficient. It is given by;

$$\alpha_m = \frac{\beta\, N_V (k_b T)^2}{E_b\, D_X}\left(sinh\left(\frac{E_b}{k_b T}\right) - \frac{E_b}{k_b T}\right) \qquad \text{Eq. 24}$$

where β is the grain boundary thickness, N_V is the number of atoms per unit volume, E_b is the solute-boundary binding energy and D_X is the trans-interface boundary diffusion.

From Eq. 21(a), Eq. 22 and Eq. 23 the overall boundary mobility ($M_{GB,eff}$) is given by:

$$\frac{1}{M_{GB,eff}} = \frac{1}{M_{GB,i}} + \alpha C_0 \qquad \text{Eq. 25}$$

Recently Zurob and Dunlop [85, 100] used this approach to model the solute drag effect on recrystallization kinetics. The maximum value of intrinsic mobility used was given by

Turnbull mobility[83, 92] which is the boundary mobility in absence of all possible attachment kinetics.

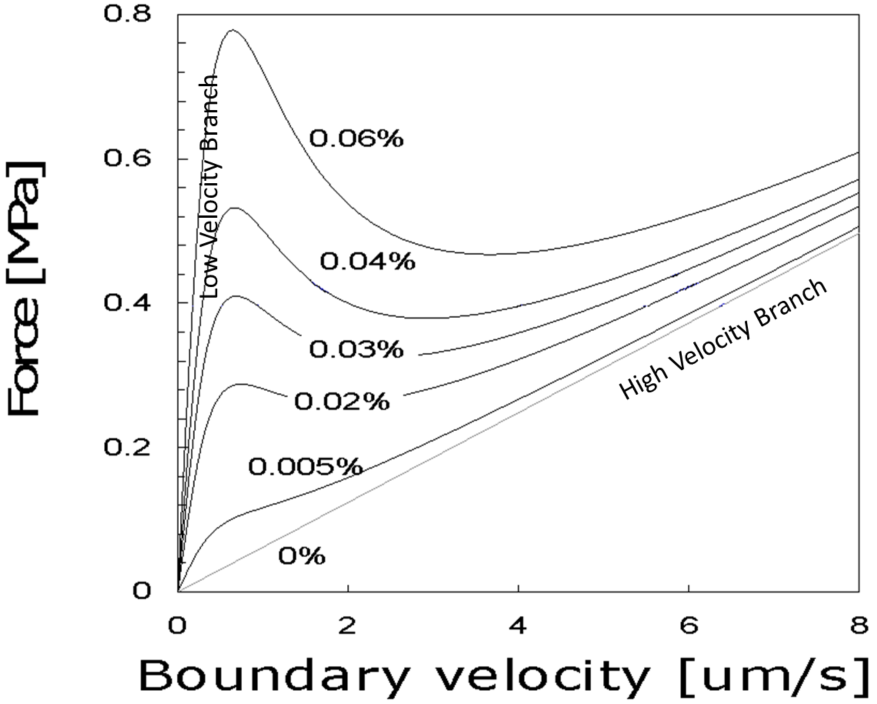

Figure 15: Cahn's solute drag plot for different values of Nb, showing the low velocity and high velocity branch. [101]

2.3.2.2. Zener Pinning

Presence of fine dispersion of hard second phase particles are known to delay or completely stop recrystallization [102]. This is due to the fact that when a moving boundary intersects a particle a small area of the boundary disappears. The potential energy of the system gets lowered by an amount equal to the total surface energy of the absent boundary as shown in **Figure 16**. Therefore for the boundary to break away from the particle it needs to create the surface thus raising the overall energy. This difference in energy level is what is termed as Zener drag.

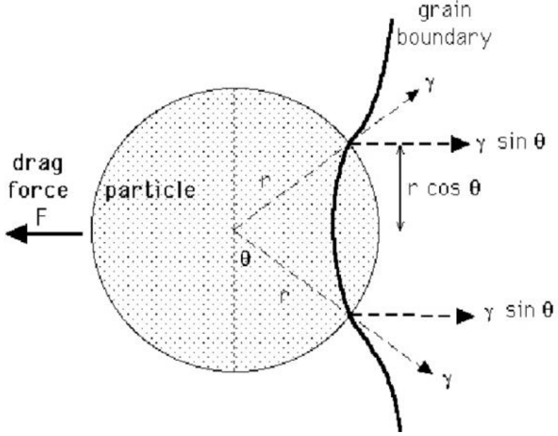

Figure 16: The interaction between a grain boundary and a spherical particle [103]

The net drag force on the boundary of energy γ per unit area due to a non shearable particle of radius r is given by

$$F = 2\pi r\gamma \sin\theta \cos\theta \qquad \text{Eq. 26}$$

The force is maximum when θ=45°. Substituting this value in the above equation gives the maximum force experienced by the boundary:

$$F = \pi r\gamma \qquad \text{Eq. 27}$$

For a random distribution of particles of radius r the number of particles per unit volume is

$$N_V = \frac{3F_V}{4\pi r^3} \qquad \text{Eq. 28}$$

where F_V is the volume fraction of the particles. Number of particles intersecting unit area(N_S) of the grain boundary is diameter of the particle times N_V.

$$N_s = \frac{3F_V}{2\pi r^2} \qquad \text{Eq. 29}$$

The total drag force then becomes N_s times F

$$P_Z = \frac{3F_V\gamma}{2r} \qquad \text{Eq. 30}$$

In terms of classical thermodynamics Zener drag is not a drag force as it is discontinuous rather, it is a form of activation energy needed by the moving boundary to pass through the obstacles.

In case of microalloyed steels since precipitation takes place after deformation, grain boundaries are preferential sites for precipitation thus making the grain boundary experience a higher Zener drag than what is calculated from the above equation assuming a random distribution. This is discussed in more detail in section 3.1.3.6.

2.3.3. Modeling of Recrystallization Kinetics

It has been demonstrated in numerous experiments that progress of recrystallization follows a sigmoidal curve. One of the earliest and simplest models to explain this was by Johnson, Mehl, Avrami and Kolmogorov (JMAK) model. The key concept of the model is extended volume fraction [12].

$$X_{ext} = \int_0^t V_t \dot{N} dt \qquad \text{Eq. 31}$$

where, $\dot{N}$ is the nucleation rate (assumed constant) and V_t is the volume of the single recrystallized grain. The extended volume fraction does not take into consideration the impingement of one growing nuclei on another and that new nuclei can't form in areas which has already been recrystallized. If the nuclei are randomly distributed in the deformed material then the actual recrystallized fraction is given by:

$$X = 1 - \exp(-X_{ext}) \qquad \text{Eq. 32}$$

Combining the above two equation and replacing volume by $4\pi(v\ t)^3/3$ one obtains:

$$X = 1 - \exp\left(-\frac{4\pi}{3}\int_0^t \dot{N} v^3 t^3 dt\right) \qquad \text{Eq. 33}$$

where v is the velocity of the interface. In the most common formulation of the above equation nucleation rate and growth velocity are assumed to be constant. Consequently the above equation simplifies to:

$$X = 1 - \exp\left(-\frac{\pi}{3}\dot{N} v^3 t^4\right) \qquad \text{Eq. 34}$$

The above equation is the simplified JMAK equation for constant nucleation and growth rates.

Most of the empirically/quasi-physically based modeling has assumed nucleation and growth rates to be constant and the two values are clubbed up together in one variable. Consequently the above equation simplifies to:

$$\mathrm{X} = 1 - \exp(-\mathrm{K}\mathrm{t}^{\mathrm{n}}) \qquad \text{Eq. 35}$$

K and n are commonly referred to as Avrami constants. Conventionally, Avrami constants are not calculated separately but are obtained by fitting the JMAK equation to the experimentally obtained recrystallization kinetics data due to which any physical meaning is difficult to derive out of the values of those constants. As such, at best Avrami constants are quasi-physical parameters.

The above equation can be similarly derived for the limiting case of site-saturation wherein all nuclei will be formed before the start of recrystallization growth. This assumption will lead to an exponent value of 3. JMAK exponent will lie in between 3 and 4 when nucleation decreases at a finite rate [12]. Experimentally derived JMAK exponents can have values less than 3 also because of the fact that the growth rates and dimensionality can change during recrystallization[12].

Figure 17 shows how Avrami exponent can change during recrystallization. In the first case wherein initial grain size is 15 microns even then, if nuclei are at grain boundaries they are still random globally. Increasing the grain size to 50 microns made the nuclei distribution non-random which violated the JMAK assumption thereby leading to non-constant Avrami exponent.

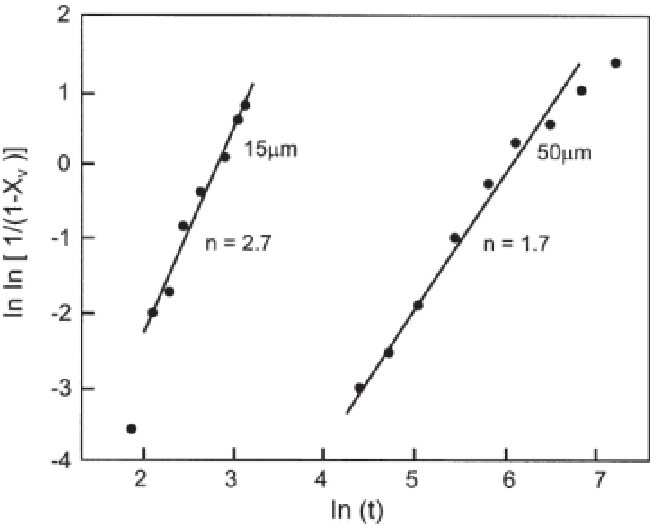

Figure 17: Recrystallization kinetics of copper at 225°C of different initial grain sizes cold rolled 93%. [104]

In industrial processing, the main objective of recrystallization is to refine coarse austenite grains (~1500 μm). Due to large size of the grains nucleation is non-random hence a constant Avrami exponent is not applicable for industrial processing. **Table 1** shows the theoretically calculated values of Avrami exponent depending on the nucleation mechanism and growth dimensionality. As discussed before (**Figure 12**) nucleation rate changes during recrystallization and site saturation or constant nucleation rate are not always true in most cases. Also the recrystallizing grain can get constrained due to sample geometry or microstructural constraint leading to dynamic change in growth dimensionality because of which, the experimentally obtained Avrami constants are not integral values and changes with time.

Growth Dimensionality	**Site Saturation**	**Constant Nucleation Rate**
3-D	3	4
2-D	2	3
1-D	1	2

Table 1: Theoretical calculated Avrami exponents[12].

JMAK model assumes a random distribution of nuclei and requires considerable modification to be used in cases where in the nucleation is supposed to start from some definite regions eg. grain boundary, twins etc. This is the most serious limitation of JMAK model.

The next generation models tried to solve this problem by making the Avrami exponent as a function of time to give a better fit to the experimental data, which was purely empirical in approach thus limiting its applicability to the domain for which it was defined and any physical interpretation of the model wasn't possible from them.

Sellars et al. [105] proposed an empirical equation for predicting time for 50% recrystallization.

$$\mathrm{t}_{50\%} = 2.5 \times 10^{-19} \mathrm{D}_0^2 \varepsilon^{-4} \exp\left(\frac{300{,}000}{\mathrm{RT}}\right) \qquad \text{Eq. 36}$$

This equation is valid for carbon manganese steels. Similar equations have been proposed for micro-alloyed steels. This and other equations of similar type, in past two decades are immensely popular with researchers studying the relative effects of influential parameters and have reported databases for activation energy, strain exponent etc for a variety of composition and processing conditions. Medina et al. [106] using torsion based experiments reported the values of the constants used in Sellar's equation for a variety of steels of both microalloyed and C-Mn type. Sun and Hawbolt [107] used Sellars models to compare recrystallization kinetics between steels having different chemistries and processing conditions, while remarking that physically based models will give a better insight but are too complicated to develop.

In 2001 Cho et al [8] used Sellars equation of $t_{50\%}$ to compare between steels of different chemistries and processing conditions. They found that Nb in solution delays growth considerably and when it precipitate at lower temperature it further delays growth. Though Sellars model isn't capable enough to predict the complete kinetics, but is quite good in making comparison between different chemistries and processing parameters.

Later on more sophisticated models [108] based upon Sellars equation and coupled with FEM, were able to predict microstructure and flow stress evolution throughout the volume of the material. Coupling Sellars equation with Forest-Hardening equation (Eq. 1) allows calculation of flow stress evolution.

These models were able to predict recrystallization evolution in multi-pass deformation under continuous cooling hence were able to predict complete austenite microstructure evolution.

In 2006, Zurob et al. [85] presented a model wherein they used a similar idea of Humphreys [109] that the rate of growth of an individual sub-grain is given by Mobility times the Driving Force. The driving force in this case is the stored energy of deformation reduced by the amount given by Zener drag of precipitates. The growth of an individual grain is assumed to be isotropic and spherical. To calculate global recrystallization kinetics Avrami extended volume approach was used. The same model was further extended and applied by Dunlop et al. [100] for Zirconium Alloys.

Later on Pereda et al. [110] developed a growth model for multi pass rolling and under non isothermal conditions from single pass isothermal models. They modeled the growth using a coupled Avrami and Sellar's equation.

$$\mathrm{X} = 1 - \exp\left[-\ln 2\left(\frac{\mathrm{t}}{\mathrm{t}_{0.5\mathrm{X}}}\right)^{\mathrm{n}}\right] \qquad \text{Eq. 37}$$

where t is time (s). $\mathrm{t}_{0.5\mathrm{X}}$ is the time to reach a 50% recrystallized fraction and n is the Avrami exponent.

$$\begin{aligned}\mathrm{t}_{0.5\mathrm{RX}} = 9.92 \times\ 10^{-11}\mathrm{D}_0\varepsilon^{-5.6\mathrm{D}_0^{-0.15}}\dot{\varepsilon}^{-0.53}\exp\left(\frac{180{,}000}{\mathrm{RT}}\right)& \\ \times \exp\left[\left(\frac{275000}{\mathrm{T}} - 185\right).[\mathrm{Nb}]\right]&\end{aligned} \qquad \text{Eq. 38}$$

For this to be applicable for a wider range of conditions the Avrami exponent was modified by

$$\mathrm{n} = 155\exp\left(-\frac{56485}{\mathrm{RT}}\right) \qquad \text{Eq. 39}$$

These equations were strictly valid for isothermal single pass rolling. To extend it for non-isothermal conditions Pereda et al [110] used the additivity principle wherein the temperature was discretized in small isothermal steps and the corresponding recrystallized fraction was calculated in each step and later on added. To calculate for multi-pass deformation schedules effective grain sizes were calculated at end of each pass and the corresponding recrystallized fraction and was used as an input for the next pass.

A physically based model for SIBM nucleation is mostly overlooked in the literature mainly because most of published work has assumed a site saturated approach and the overall kinetics is modeled using the Avrami equation thus eliminating the need for a separate nucleation model. Humphreys [89] remarks that the growth of recrystallization occurs on a scale which can be measured microscopically unlike nucleation, due to which most models and simulations of recrystallization treat growth in detail and nucleation is often overlooked.

A precise nucleation model is essential for any realistic and stable recrystallization model. It has been found [89] that, majority of nucleation occurs in a very short time compared to the total time for recrystallization (**Figure 12**) hence the number density of recrystallization nuclei is replaced by a constant [5] known as site-saturation approach. Absence of a reliable nucleation model makes it difficult to predict recrystallized grain size and incubation time. To solve these limitations researchers [85] have used the Bailey Hirsch criterion [111] to calculate the critical size of nucleation. According to the criterion a sub-grain of size $\mathrm{r(t)}$ will start to grow in an unstable manner within the deformed structure when the driving force for growth $\mathrm{G(t)}$ overcomes the capillary forces $2\,{}^{\gamma_{SE}}/_{r(t)}$ where γ_{SE} is the surface energy. Nucleation will commence when the sub-grain size is greater than $2\,{}^{\gamma_{SE}}/_{G(t)}$ .Only sub-grains larger than this size will act as nuclei and will grow.

$$r_c(t) > \frac{2\gamma_{SE}}{G(t)} \qquad \text{Eq. 40}$$

This allows the calculation of critical nuclei size. Coupling this with a growth kinetics equation of sub-grain and high angle boundary growth rate allows prediction of the incubation time for nucleation and then the complete recrystallization kinetics.

Backe [112] recently published a recrystallization model wherein it was assumed that the size of sub-grain is proportional to the mean free distance of the dislocation slip. Low angle boundary energy and sub-grain misorientation both depend upon the dislocation density. The progress of recovery causes dislocation density to decrease and at a certain critical value of the ratio of recovered dislocation density to the original deformed dislocation density nucleation was assumed to start. She proposed that the growth rate of sub-grains will be proportional to subgrain boundary mobility, driving force and the sum of vacancy concentration in the deformed and recrystallized zone. The driving force used by her is the stored energy of deformation reduced by the Zener pinning force and Solute drag forces.

2.4. Grain Coarsening in austenite

Once recrystallization is complete the fine recrystallized grains tend to coarsen driven by the curvature/surface energy. Since austenite is not stable at room temperature in HSLA steels there is not exhaustive experimental database published in literature for the case of microalloyed steels. The problem of grain coarsening has been theoretically and experimentally addressed over the past by many researchers [19, 21, 83, 113-121]. However most of the databases reported on literature for steels are based either on ferrite or on temperature stabilized austenite. Given the difficulty in etching of low alloy microalloyed austenite few experimental databases has been developed [11, 115, 122, 123]. Laser Ultrasonic has been also used to monitor in-situ grain size evolution during both recrystallization and grain coarsening [119, 124, 125].

Grain coarsening is driven by the curvature surface energy. The grains coarsen so as to minimize their boundary surface area.

In the mean field modeling technique, the driving force is approximated as inverse of the mean grain radius times the boundary surface energy approximated by a proper factor.

$$P = \frac{\alpha\gamma_{gb}}{\bar{R}} \qquad \text{Eq. 41}$$

where α is a geometric constant and γ_{gb} is the grain boundary energy. Substituting this in rate equation ($d\bar{R}/dt = MP$) and integrating gives the overall growth equation.

$$\bar{R}^2 = \overline{R_0}^2 + 2\alpha M\gamma_{gb}\,\Delta t \qquad \text{Eq. 42}$$

where $\bar{R}$ is the final average grain size, $\overline{R_0}$ is the starting average grain size.

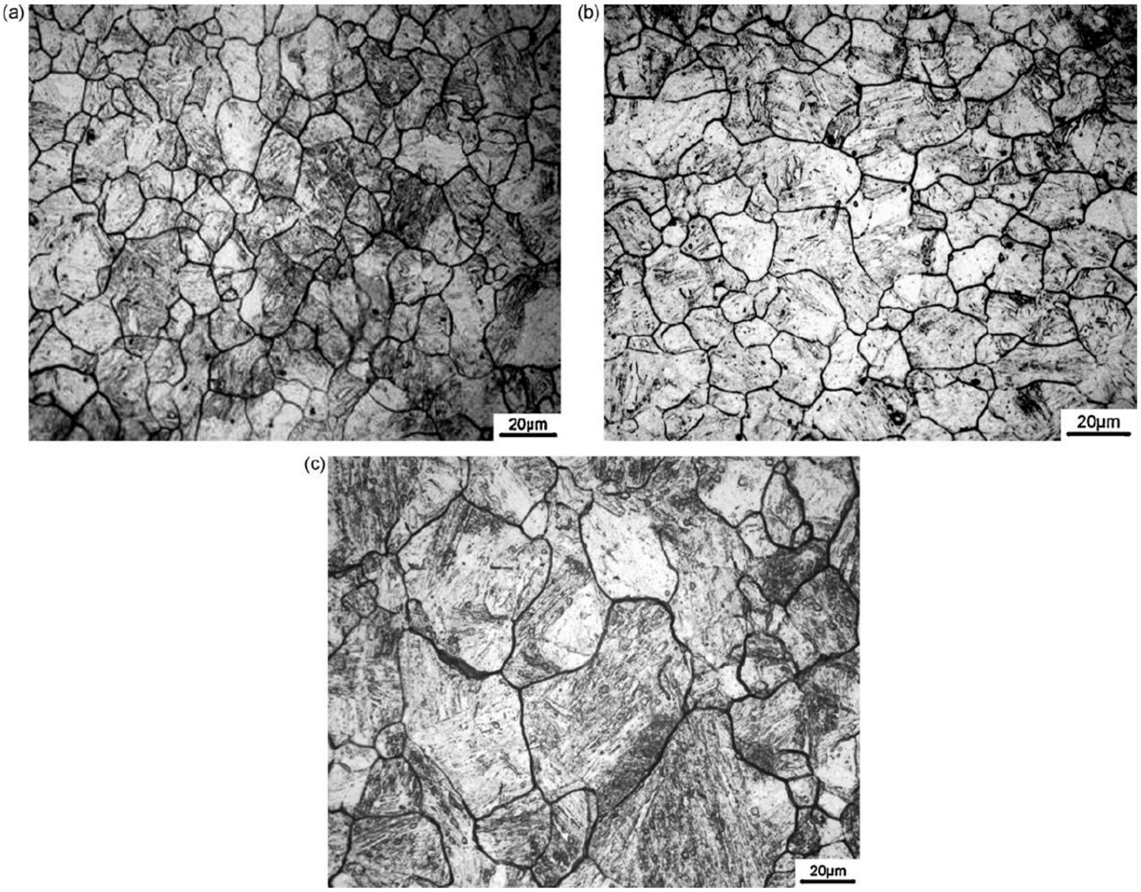

Figure 18: Grain coarsening kinetics of a 0.1 wt% Nb API X80 steel at 1000 ^{o}C, (a) recrystallized austenite grains at time t=0. (b) Coarsened grains after time t= 60 sec. (c) Coarsened grains at time t=240 sec[122].

The above equation in a more generic form is represented as

$$\bar{R}^{n} = \overline{R_0}^{n} + c\,\Delta t \qquad \text{Eq. 43}$$

where n and c are constants. Analysing the equations published in literature one finds that the constant c shows an Arrhenius type relationship with temperature. In other words;

$$\bar{R}^n = \overline{R_0}^n + \left[A\, exp\left(-\frac{Q_{gc}}{RT}\right)\right] \Delta t \qquad \text{Eq. 44}$$

Where Q_{gc} is the activation energy associated with grain coarsening and T is the temperature. A list of reported values in literature of $n, A\ and\ Q_{gc}$ as compiled by Manohar et al. is shown in

Table 2.

2.4.1. Effect of Particles

The above derivation doesn't consider the effect of particle pinning on the moving boundary. The effect of rigid particle on a moving boundary is usually calculated using a Zener-Smith formulation[103].

For non-coherent randomly distributed particles, Zener Pressure is usually represented as:

$$P_Z = \frac{3F_V\gamma_{gb}}{2r} \qquad \text{Eq. 45}$$

where F_V is the volume fraction of the second phase particles, r is the mean particle radius.

The Zener drag can be subtracted from the driving force for boundary movement Eq. 41, giving the net available driving force. Modifying rate equation to incorporate Zener drag the equation becomes:

$$\frac{dR}{dt} = M\left(\frac{\alpha\gamma_{gb}}{\bar{R}} - \frac{3F_V\gamma}{2r}\right) \qquad \text{Eq. 46}$$

Since the above equation is not explicit in terms of R it can only be numerically integrated.

From the above equation it is clear that upon integration the exponent of grain size (R) will be 2 if normal grain growth behaviour is assumed. However using the above equation to fit the experimental data the results are not always encouraging. Accurate knowledge of precipitate volume fraction and size distribution along with boundary mobility is essential. Accurate knowledge of solute content evolution is important to calculate the solute drag so as to calculate the boundary mobility for prediction of grain size evolution. Experimentally this is difficult, which has led the researchers to fit the experimental data with different exponent values as shown in

Table 2.

Steel type	n	A	Q_{gc}	Temp, K	Units	Ref
C-Mn	10	3.87E+32	400,000	>1273	Gs in µm, Q_{gc} in J/mol, R in J/mol-K, t in sec	[19]
		5.02E+53	914,000	<1273		
Low C-Mn	2	4.27E+12	66,600		Gs in µm,Q_{gc} in Kcal/mol, R in Kcal /mol-K, t in sec	[126]
0.22C-0.9Mn	2	1.44E+12	63,780		Gs in µm, Q_{gc} in Kcal/mol, R in Kcal /mol-K, t in sec	[127]
C-Mn C-Mn-V	7	1.45E+27	400,000		Gs in µm,Q_{gc} in J/mol, R in J/mol-K, t in sec	[10]
C-Mn-Ti	10	2.60E+38	437,000		Gs in µm, Q_{gc} in J/mol, R in J/mol-K, t in sec	[10]
C-Mn-Nb	4.5	4.10E+23	435,000		Gs in µm, Q_{gc} in J/mol, R in J/mol-K, t in sec	[10, 128]

Table 2: Summary of various grain coarsening equations reported in literature as compiled by Manohar et al. [120].

3. Modeling framework

In the first part of this chapter individual process models will be discussed along with the various interdependencies observed between them. Recovery is discussed in section 3.1.1, precipitation is discussed in section 1 and recrystallization is discussed in section 3.1.3. The rest of the chapter focuses towards the individual specific sub processes operating.

3.1. Individual Process Modules

3.1.1. Recovery Module

Following the analysis of Verdier et al. [38], the decay in internal stress can be represented by a single parameter. Recovery is modeled using a modified version of Friedel's model [33] which is due to Verdier et al. [38] :

$$\frac{d\sigma_D}{dt} = -\frac{64\sigma_D^2 \upsilon_d}{9M^3 \alpha E} exp\left(-\frac{U_a}{k_b T}\right) sinh\left(\frac{\sigma_D V_a}{k_b T}\right) \qquad \text{Eq. 47}$$

where, U_a and V_a are the activation energy and activation volume respectively. In the domain of microalloyed steels activation energy is assumed to be constant, value of which will be between activation energy for pipe diffusion and bulk diffusion [22]. In the present analysis the value of activation energy does not discriminate between cross-slip, climb or solute drag. A value equal to 285 kJ/mol equal to austenite self-diffusion[22] has been used which satisfactorily explains the experimental data set. V_a was initially used as a fitting parameter for recovery model. **Figure 19** shows the value of V_a as a function of Nb content and temperature obtained after fitting the experimental softening data.

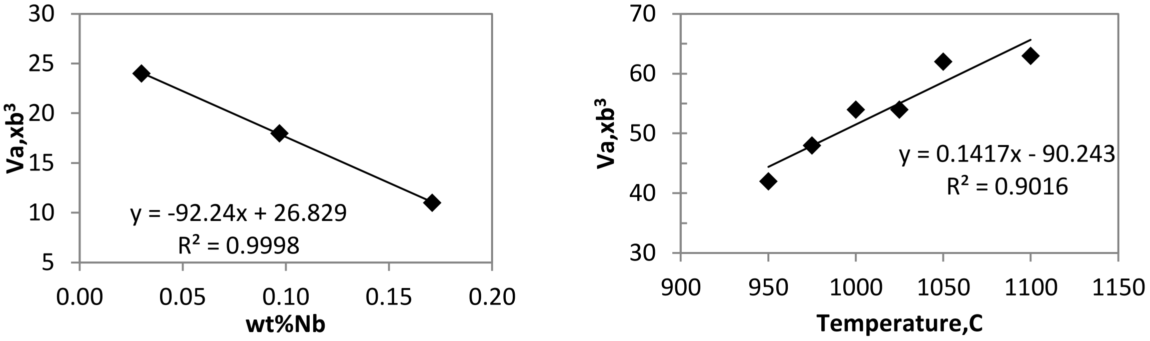

Figure 19: (a) Plot of activation volume as a function of solute Nb content. (b) Plot of activation volume as a function of annealing temperature for the same steel composition.The steel contains 0.03 Nb, 0.076C and 0.097 Nb, 0.002 C rolled to a strain of 0.3 at a strain rate of 10 s-1 at 900 °C [29, 129]

The effect of solute content on recovery kinetics enters into the model through this parameter. However from the data fit it was realised that V_a shows a strong relationship with solute content and temperature. This motivated us to develop a relationship between activation volume, solute Nb and temperature. Activation volume in Verdier's model refers to activation distance (V_a/b^2) which is the distance between pinning centres of a subgrain boundary. In present argument we have assumed that pinning centres can be either extrinsic dislocations, the spacing of which is proportional to $1/\sqrt{\rho}$, or it could be solute clusters the spacing of which will be proportional to $1/\sqrt[3]{C}$ as calculated through dimensional analysis. For simplicity, both of them are treated as equivalent. The total spacing between pinning centres λ can now be expressed as:

$$\frac{1}{\lambda} = K_1\sqrt{\rho} + K_2\sqrt[3]{C_{Nb}} \qquad \text{Eq. 48}$$

where K_1 and K_2 are proportionality constants, the knowledge of which is essentially for modeling sub-grain growth. Instead of calculating it from first principles we have back calculated it from experimental results [130]:

$$\frac{1}{\lambda} = 6.3\sqrt{\rho} + \frac{0.042}{b}\sqrt[3]{C_{Nb}} \qquad \text{Eq. 49}$$

Finally the activation volume (λb^2) is given by;

$$V_a = {b^2}\Big/\left(6.3\sqrt{\rho} + \frac{0.042}{b}\sqrt[3]{C_{Nb}}\right) \qquad \text{Eq. 50}$$

This equation leads to unrealistically large activation volumes when the dislocation density is low and the amount of solute Nb is small. For example for a case of 0.03 wt % Nb and dislocation density of 4x10^{14}/m^3 the activation volume was calculated to be $23b^3$, where b is the magnitude of burgers vector. When solute Nb has been reduced to 0.001 wt% and dislocation density was reduced to 4x10^{14}/m^3 activation volume was calculated to be $84b^3$. In reality, other pinning points including pinning due to other solutes such as Mn should be included in the above equation. To capture this, we have used the minimum of V_a as given by Eq. 50 and $35b^3$ as the activation volume for sub-boundary motion.

3.1.1.1. Effect of second phase particles on recovery

Strain induced precipitation of Nb occurs with an incubation time and preferentially nucleates on dislocation nodes and grain boundaries. Concurrent strain induced precipitation with recovery can lead to arrest of recovery kinetics by pinning of dislocations nodes until the time when the precipitates coarsen and unpin the dislocation nodes.

Previous treatment by Zurob et al. [5] has tried addressing this problem by removing the number of dislocations pinned by the precipitates from participating in recovery. In simplified terms:

$$\frac{d\sigma_D^{ppt}}{dt} = \frac{d\,\sigma_D}{dt}\left(1 - \frac{n_{ppt}}{n_c}\right) \qquad \text{Eq. 51}$$

Here n_c is the number of dislocation nodes, n_{ppt} is the number of precipitates, $\frac{d\sigma_D^{ppt}}{dt}$ is the recovery rate in presence of strain induced precipitation and $\frac{d\,\sigma_D}{dt}$ is the recovery rate in absence of precipitation Eq. 47. The model predicts a complete halt in recovery kinetics when $\frac{n_{ppt}}{n_c}$ approaches unity that is when the number of particles is equal to the number of dislocation nodes.

Therefore the overall recovery equation becomes:

$$\frac{d\sigma_D}{dt} = -\frac{64\sigma_D^2 v_d}{9M^3\alpha E}\,exp\left(-\frac{U_a}{k_bT}\right) sinh\left(\frac{\sigma_D V_a}{k_bT}\right)\left(1 - \frac{n_{ppt}}{n_c}\right) \qquad n_{ppt} < n_c \qquad \text{Eq. 52(a)}$$

$$\frac{d\sigma_D}{dt} = 0 \qquad n_{ppt} \geq n_c \qquad \text{Eq. 52(b)}$$

For a typical case of Nb microalloyed steel the prediction of Eq. 52 and precipitate number density are plotted in **Figure 20** for 0.03 Nb, 0.076 C deformed to a strain of 0.3 at 950^{o}C. Precipitate number density is calculated by Eq. 58 which will be discussed in a later section. In this case the microstructure exhibits concurrent recovery and precipitation which is shown in **Figure 20**. During the initial time, recovery proceeds with the kinetics as explained by Eq. 47 with little or no interference with precipitation. However as the number of precipitate particle increases the rate of recovery is reduced as described by Eq. 52(a) till the time when precipitate number density is less than dislocation node density. Once precipitate number density exceeds dislocation number density recovery kinetics is explained by Eq. 52(b). Once dislocation entangles start becoming unpinned recovery kinetics again is explained by Eq. 52(a).

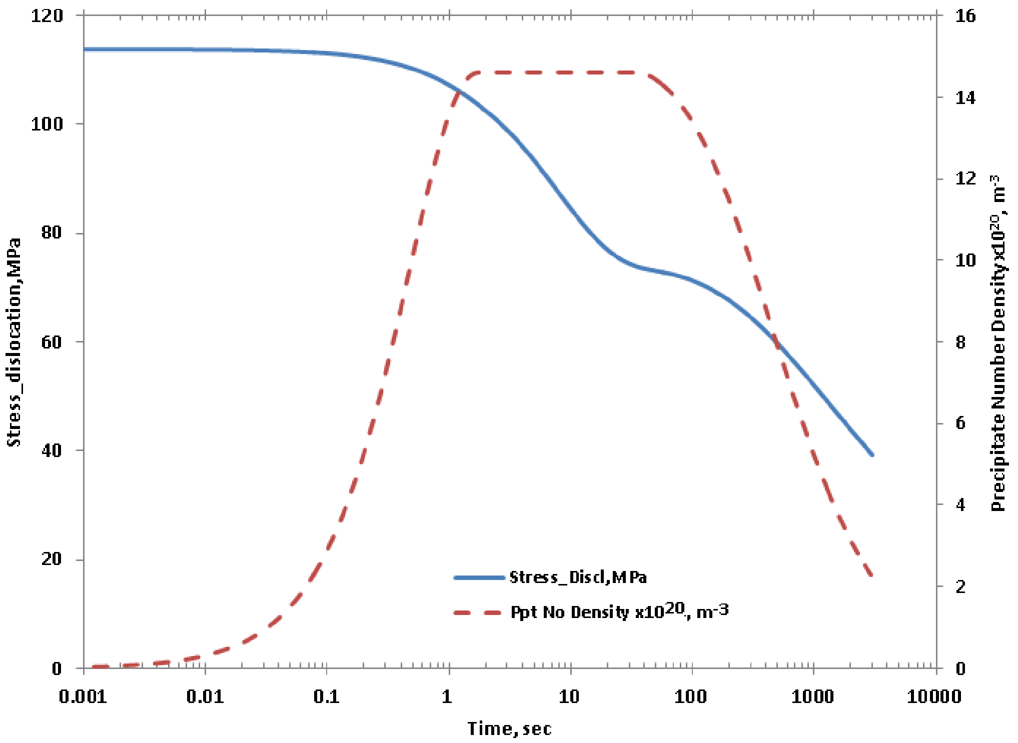

Figure 20: Plot showing the decay in stress due to recovery. Precipitate number density is superimposed on to the plot highlighting that at sufficient number density recovery is arrested halted till coarsening of precipitates starts. The composition of the steel is 0.03 wt % Nb, 0.076 wt % C deformed to strain of 0.3 at 950 °C.

3.1.2. Precipitation Module

In what follows, the precipitation model of Deschamps and Brechet [80] modified by Zurob et al. [5]is used to describe the nucleation, growth and coarsening of Nb(C,N). Precipitation is assumed to occur in two steps. The first step involves nucleation and growth of precipitates as concurrent processes and the second step deals with growth and coarsening of the existing precipitates. The same approach has also been used by Dutta et al. [15] to model Nb(C,N) precipitates in microalloyed austenite. Their results are in excellent agreement with the experimental data [65].

3.1.2.1. Nucleation and Growth

The nucleation model used is a modified form of classical nucleation theory. Nucleation is assumed to occur extensively on dislocations. Although the shape of the nucleus changes with the potential nucleation sites, coherency, crystallography etc. for the present analysis spherical nuclei are assumed. Consequently the driving force for precipitation ($\boldsymbol{\Delta G}$) is given by:

$$\Delta G = \Delta G_{chem} + \Delta G_{int} + \Delta G_{disl} \qquad \text{Eq. 53}$$

Where ΔG_{chem} is the chemical driving force,

$$\Delta G_{chem} = -\frac{4}{3}\pi r^3 \Delta G_v \qquad \text{Eq. 54}$$

where r is the nucleus radius, ΔG_v is the volumetric driving force and is calculated using solubility product of Koyama et al.[64] using the method described by Dutta and Sellars [15]. ΔG_{int} is the interfacial free energy and is given by:

$$\Delta G_{int} = 4\pi r^2 \gamma \qquad \text{Eq. 55}$$

where, γ is the NbCN/Austenite interphase energy in (J/m^2) and is given by [5]

$$\gamma = 0.375 + (0.000025(T_{sol} - T)^{1.5}) \qquad \text{Eq. 56}$$

where, T_{sol} is the dissolution temperature of the precipitates and T is the operating temperature. ΔG_{disl} is the relaxation of dislocation core energy over the precipitate radius and also contains the relaxation of elastic energy around dislocations;

$$\Delta G_{disl} = -\mu b^2 r\left(\frac{1}{5} + \frac{\ln(r/b)}{2\pi}\right) \quad \text{Eq. 57}$$

where μ and b are the shear modulus and Burgers vector respectively. Finally the nucleation rate (steady state) is given by:

$$\frac{dn}{dt} = (n_{total} - n)Z\beta' exp\left(-\frac{\Delta G}{kT}\right) \quad \text{Eq. 58}$$

where Z is the Zeldovich non-equilibrium factor, β' is the rate at which atoms are added to the critical nucleus, n_{total} is the total number of nucleation sites. The second term (n) in the equation relates to the progressive decrease in the available nucleation sites. Following Zurob et al.[5] and Russell [131] $Z\beta'$ is approximated as $\frac{D_{pipe}C_{Nb}}{a^2}$, where D_{pipe} is the pipe diffusion coefficient and a is the lattice parameter of the precipitate. The density of the available nucleation sites, n_{total} has been approximated as$(F_N\ (\frac{\rho}{b}))$, where F_N is a parameter smaller than unity which relates to a minimum distance between precipitates on a dislocation line. During the nucleation and growth stage, the evolution of average particle radius is given by [15, 130]:

$$\frac{dr}{dt} = \frac{D_{eff}}{r}\,\frac{C_{Nb} - C_{Nb}^{r}}{C_{Nb}^{P} - C_{Nb}^{Eq}} + \frac{1}{n}\frac{dn}{dt}(\alpha_N r_N - r) \quad \text{Eq. 59}$$

where C_{Nb}^{r} is the concentration of Nb in equilibrium with a precipitate of radius r. The first term of the equation refers to the parabolic growth equation of the existing particles and the second term refers to the change in particle size due to nucleation of n new particles of size $\alpha_n r_N$. α_N is a constant of value 1.05 [15] and refers to the fact that a nucleated particle will only grow when its radius is greater than the critical radius. The diffusion coefficient used in the equation is a weighted average of bulk and pipe diffusion coefficients as the niobium in solution can migrate to join precipitates either by bulk diffusion or through the high diffusivity dislocation channel.

$$D_{eff} = D_{pipe}\, \pi\, R_{core}^{2} \rho + D_{bulk}(1 - \pi R_{core}^{2} \rho) \qquad \text{Eq. 60}$$

Where R_{core} refers to the radius of dislocation core which is assumed to be equal to Burgers vector b.

3.1.2.2. Growth and Coarsening

As soon as critical radius for nucleation and mean precipitate radius become equal coarsening of the particles begins. Using the approach of Lifshitz-Slyozov-Wagner (LSW), in the case of pure coarsening the evolution of radius is given by;

$$\left.\frac{dr_i}{dt}\right|_{coarsening} = \frac{D_{eff}}{r} \frac{C_{Nb}^{R} - C_{Nb}^{Ri}}{C_{Nb}^{P} - C_{Nb}^{Eq}} \qquad \text{Eq. 61}$$

$\boldsymbol{r}$ is the average precipitate radius. The variable $\boldsymbol{r_i}$ refers to the radius of a specific precipitate. Precipitates having a radius greater than the average radius r will grow and others will tend to shrink and finally will dissolve. Integrating Eq. 61 over the entire size distribution gives the time evolution of precipitate radius. However, given the limitation of the present modeling approach (mean field approximation) and based on the work of

Deschamp and Brechet [80] $\boldsymbol{r_i}$ has been replaced by$\left(\frac{27}{23}\right)r$, the inherent assumption being that large particles contribute more towards the average value [15, 80].

During the simultaneous growth and coarsening regime the overall precipitate size evolution is given by a weighted average of growth and coarsening contribution.

$$\frac{dr}{dt} = (1 - f_{coarse})\left.\frac{dr}{dt}\right|_{growth} + f_{coarse}\left.\frac{dr}{dt}\right|_{coarsening} \qquad \text{Eq. 62}$$

$$f_{coarse} = 1 - erf\left(4\left(\frac{r}{r_n} - 1\right)\right) \qquad \text{Eq. 63}$$

In Eq. 62, $\left.\boldsymbol{\frac{dr}{dt}}\right|_{\boldsymbol{growth}}$ refers to the radius evolution kinetics under pure growth conditions. It is given by the first part of Eq. 58. Similarly, $\left.\boldsymbol{\frac{dr}{dt}}\right|_{\boldsymbol{coarsening}}$ refers to the increase in particle radius under pure coarsening regime given by Eq. 61. The coarsening function varies between 0 to 1; 0 under pure growth condition $(\boldsymbol{r \gg r_n})$ and 1 under pure coarsening condition$(\boldsymbol{r = r_n})$. Similar equation to Eq. 62 and Eq. 63 is used to calculate the precipitate number density During pure growth $\left.\boldsymbol{\frac{dn}{dt}}\right|_{\boldsymbol{growth}} \boldsymbol{= 0}$. Eq. 64 is a solute balance equation the differentiation of which with respect to time gives the rate of variation of precipitate number density under pure coarsening [80].

$$C\left(1 - \frac{4}{3}\pi n r^3\right) = C_0 - \frac{4}{3}\pi n r^3 \qquad \text{Eq. 64}$$

3.1.3. Recrystallization Module

The present model developed is largely based upon the recrystallization model developed by Dunlop et al. [100] for Zircalloy-4. The model is able to predict incubation time, nucleation rate and recrystallized grain size. In what follows the model has been modified and adapted for microalloyed steels.

In present approach, nucleation is assumed to be SIBM, which is a reasonable assumption for small strains as discussed in section 2.3.1. It is also supported by metallographic observation of Hansen et al. [65] where he found that for low strains (0.1 to 0.4) SIBM is a reasonable assumption and at high strain recrystallization does nucleate at twin boundaries and deformation bands. During rough rolling of microalloyed steels the starting austenite grain size is of the order of the order of 1500 µm which makes the assumption of random nucleation in the classical JMAK equation invalid. As discussed in the literature review, researchers have tried to solve this problem by making use of modified JMAK equation i.e by making the JMAK exponent a function of processing parameters. However specific events such as impingement of new grains that have nucleated in proximity of one another along the grain boundary have not been taken into account. A better description of nucleation and growth of recrystallization is illustrated in **Figure 21**. Nucleation has been restricted to only occur at grain boundaries. These nuclei grow within a shell so as to consume the original deformed shell volume. Once the entire shell has been consumed we switch over to pure growth scenario in which a recrystallized surface shell progressively grows towards the center consuming the deformed volume. At any instant the ratio of shell volume to the original deformed grain volume gives the recrystallized volume fraction. These two stages are described in detail in the subsequent section. For simplicity of the math we have assumed the deformed grains to be spheres and the nuclei to be hemispheres, although in reality the deformed grains are ellipsoid and nuclei have irregular surface. This has partially been compensated by changing the volume of the initial grain so as to have the same surface to volume ratio (potential nucleation sites) as that of deformed/pancaked grains.

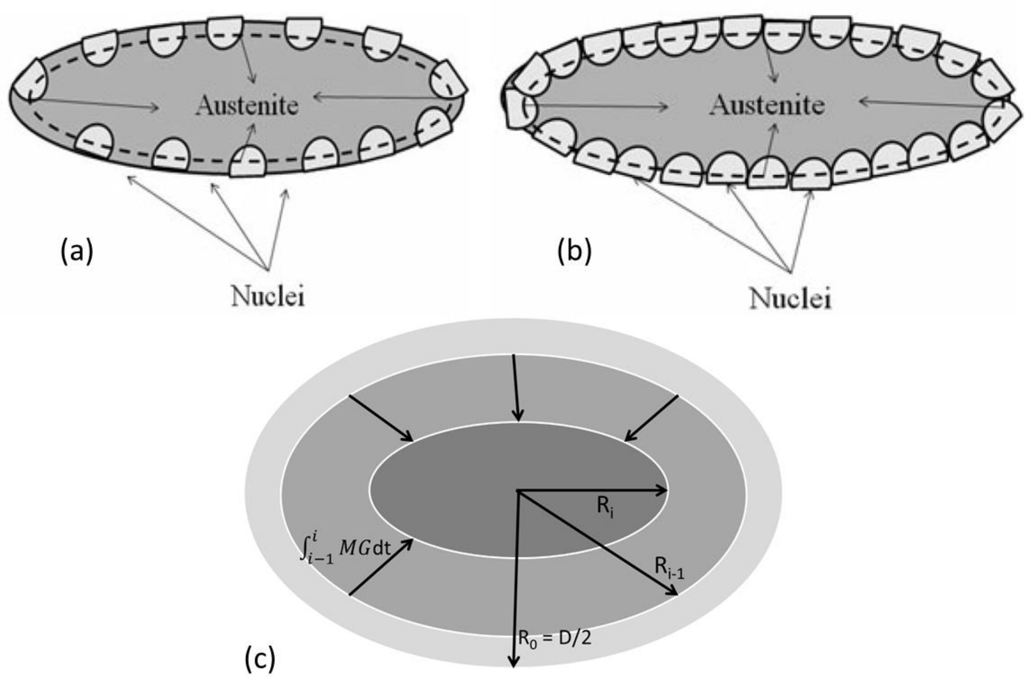

Figure 21: (a) Start of nucleation. Hemispherical nuclei form at the grain boundary by SIBM. The dotted line shows the equivalent recrystallizing film position. (b) Site saturation achieved. New hemispherical nuclei consume the original deformed HAGB. The dotted line shows the equivalent recrystallizing film position. (c) Schematic of the growth of recrystallization front[132]

3.1.3.1. Sub-grain growth

Deformation of austenite leads to the formation of a statistical distribution of subgrains/cells which is assumed to remain self-similar during sub-grain growth. During annealing of the microstructure the average sub-grain size evolves so as to reduce the total stress of the system as discussed in section 3.1.1 and in **Figure 4** at a rate proportional to the sub-grain mobility times the driving force for sub-grain growth.

Recent investigation by Winning et al. [133] has tried to address sub-grain boundary migration. The study essentially concluded that the boundary movement involves bowing out of intrinsic dislocations (structural dislocations) between extrinsic dislocations (structurally necessary dislocations), these extrinsic dislocations act as pinning centres.

The original analysis done by Winning et al. [133] was restricted to pure material and with low driving forces. In the subsequent section, we kept the original methodology and modified several of its parameters so as it can be extended to microalloyed steels. With reference to **Figure 22**, the force experienced by each dislocation is $n\tau$, where n is the number of intrinsic dislocations between two extrinsic dislocations and τ is the resolved shear stress. The shear force along with the chemical potential difference $\Delta\mu$ will cause pinning points to climb. In general movement of extrinsic dislocation can be expressed in terms of diffusion flux:

$$J = -\frac{2D}{\Omega\lambda}\, Sinh\left(\frac{\Delta\mu}{2kT}\right) \qquad \text{Eq. } 65$$

where Ω is the atomic volume, λ is the spacing between pinning centres (ref **Figure 22**), D is the bulk self-diffusion coefficient.

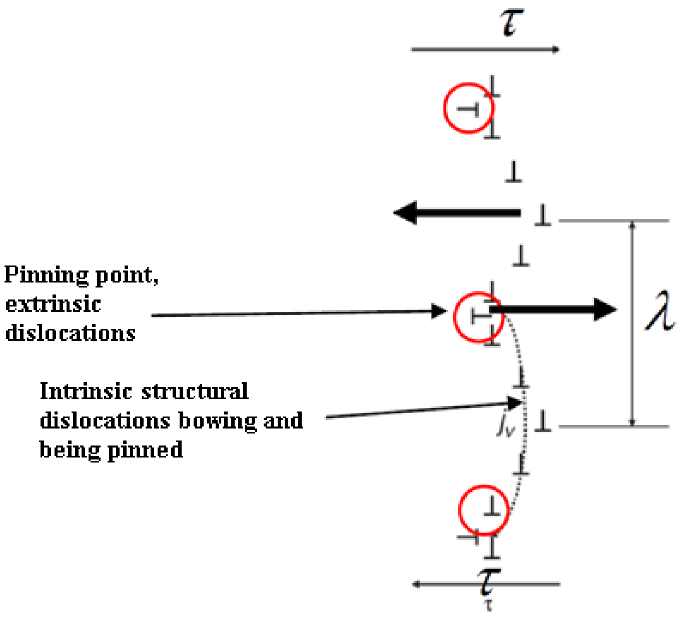

Figure 22: Schematic of the plot of subgrain boundary bowing out while being pinned by extrinsic dislocations[134].

Substituting $2n\tau\Omega$ for the chemical potential difference $\Delta\mu$ leading to;

$$J = -\frac{2D}{\Omega\lambda}\, Sinh\left(\frac{n\tau\Omega}{kT}\right) = -\frac{2D}{\Omega\lambda}\, Sinh\left(\frac{\lambda\theta\tau\Omega}{b\ kT}\right) \qquad \text{Eq. 66}$$

where, the number of dislocations between pinning points n was estimated as $\lambda\left(\frac{\theta}{b}\right)$, where θ is the misorientation of the low angle boundary. λ is calculated as per Eq. 49. The present approach unifies the two modules for recovery and recrystallization giving further confidence in our modeling approach.

Finally the sub-grain boundary velocity is given by;

$$V = -Jb^3 = 2\,\frac{Db^3}{\Omega\lambda} Sinh\left(\frac{\lambda\theta\tau\Omega}{b\,kT}\right) \sim 2\,\frac{D}{\lambda} Sinh\left(\frac{\lambda\theta\tau\Omega}{b\,kT}\right) \qquad \text{Eq. 67}$$

We assume that $\tau\theta$ is proportional to the stress increment due to dislocations, σ_D. Consequently the sub-grain velocity is given by:

$$V = 2\frac{D}{\lambda} Sinh\left(\frac{K_{ad}\ \sigma_D\ \lambda\Omega}{b\ kT}\right) \qquad \text{Eq. 68}$$

Where K_{ad} is an adjustable parameter calculated by fitting experimental data. The above equation is very similar to the one developed by Friedel et al. [33] for dislocation motion in the presence of solute clusters.

Since the velocity of the sub-grain boundary is $\langle r_t \rangle / dt$, the sub-grain growth is finally given by

$$\langle r_t \rangle = \langle r_0 \rangle + \int_0^t 2\frac{D}{\lambda} Sinh\left(K_{ad}\sigma_D b^2 \frac{\lambda}{kT}\right)\, dt \qquad \text{Eq. 69}$$

3.1.3.2. Recrystallization Nucleation

According to the Bailey-Hirsch nucleation criterion a nucleus is formed when the driving force for growth is enough to overcome the capillary forces $(2\gamma_{\mathrm{SE}}/R_{SG})$, where γ_{SE} is the grain-boundary energy and R_{SG} is subgrain radius. At the beginning of annealing the sub-grains are very small and the driving force will not be able to overcome the capillary forces so as to bulge in the neighbouring grains. The critical size for bulging of the subgrains is given by:

$$r_c = \frac{2\gamma_{SE}}{\Delta G_t} \qquad \text{Eq. 70}$$

Where ΔG_t is the driving force for subgrain growth given by:

$$\Delta G_t = \frac{1}{2}\Delta\rho'\,\mu b^2 \qquad \text{Eq. 71}$$

where $\Delta\rho'$ is the dislocation density difference between the two sides of grain boundary. If the dislocation density difference is the same on both sides of the boundary, then $r_c \rightarrow \infty$. If one is to assume that the recovered substructure is dislocation free then $\Delta\rho' = \rho$, where ρ is the global dislocation density. Due to lack of availability of exact numbers on the dislocation density difference in the present work we have used an intermediate value of $\Delta\rho' = \rho/2$ unless stated otherwise.

Due to static recovery taking place continuously, ΔG_t in Eq. 70 is a decreasing function of time leading to critical radius for subgrain bulging as an increasing function of time. If the applied strain is less than the critical strain the increase in subgrain size is not able to overcome the capillary drag forces as shown in **Figure 23**, however if the strain is higher than a critical amount the subgrain will be able to overcome the critical conditions leading to nucleation of recrystallization. The time taken by largest subgrain to overcome the capillary drag force is known as incubation time. The largest subgrain in the distribution is the one which first bulges out. Knowledge of sub-grain size distribution is essential to predict incubation time.

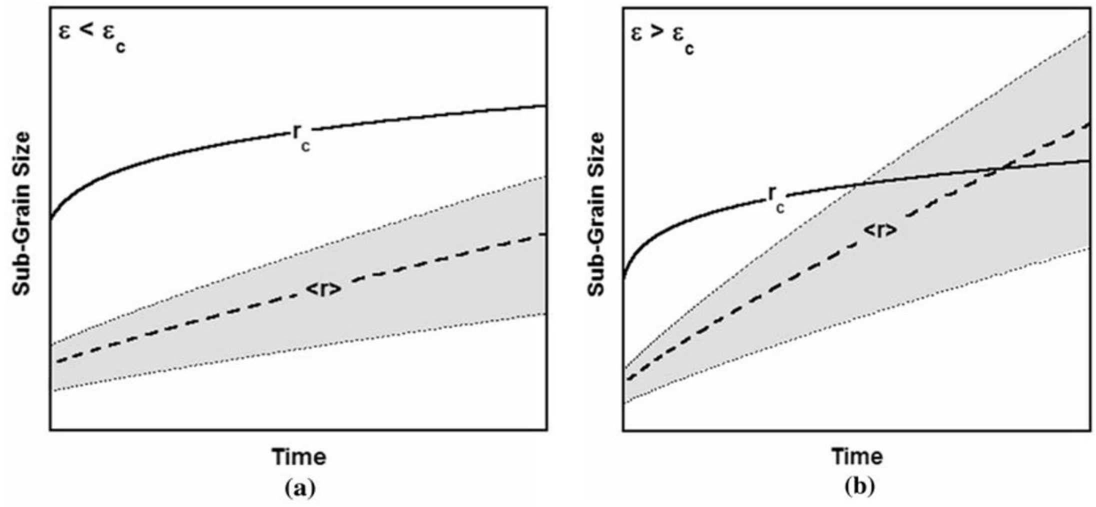

Figure 23: Time evolution of sub-grain size and critical radius of nucleation when applied strain is (a) less than the critical strain of nucleation (b) more than the critical strain of nucleation

Hansen and coworkers [135, 136] measured sub-grain distribution of variety of metals and found that they follow a Rayleigh distribution.

$$P(\chi) = \frac{\pi}{2}\chi\, exp\left(-\frac{\pi\chi^2}{4}\right) \qquad \text{Eq. 72}$$

where, χ is the sub-grain size normalized by the average sub-grain size $\langle r_t \rangle$,

$$\chi = \frac{r}{\langle r_t \rangle} \qquad \text{Eq. 73}$$

And the normalized critical sub-grain size is given by:

$$\chi_{c,t} = \frac{R_{c,t}}{\langle r_t \rangle} \quad \text{Eq. 74}$$

The fraction of the sub-grains $f(t)$, which are larger than the critical size χ_c, is then given by:

$$f(t) = \int_{\chi_{c,t}}^{\infty} P(\chi) d\chi \quad \text{Eq. 75}$$

which has an analytical value of :

$$f(t) = exp\left(-\frac{\pi}{4}\chi_{c,t}^2\right) \quad \text{Eq. 76}$$

Assuming recrystallization occurs solely due to SIBM, only subgrains which are at the grain boundary can develop into recrystallization nuclei. This is obtained by dividing the grain boundary area by the subgrain cross sectional area. Coupling this concept with Eq. 76 one may obtain the nucleation rate as

$$\frac{dN}{dt} = \frac{df}{dt}\frac{S_V}{A_{nucl}} F_n(t) \quad \text{Eq. 77}$$

where A_{nucl} is the average area of a viable nucleus, S_V is the deformed grain boundary area per unit volume and $F_n(t)$ is a function introduced to take into consideration the progressive consumption of nucleation sites.

$$F_n(t) = 1 - \frac{V_{rex}}{4\pi R_i^2 \delta} \quad \text{Eq. 78}$$

V_{rex} is the total volume of recrystallized grains within the outer shell of the deformed grain, R_i is the initial radius of the deformed grain and δ is the thickness of grain boundary shell as shown by **Figure 21**. At the start of annealing $F_n(t)$ is one and as nucleation proceeds, site saturation eventually occurs leading to nucleation rate dropping down to zero which occurs when $F_n(t)$ equals zero.

S_v in Eq. 77 refers to the grain boundary area per unit volume which is calculated using an empirical model of Yoshie et al[137].

$$S_v = \left(\frac{24}{\pi D_i}\right)(0.491e^{\varepsilon} + 0.155e^{-\varepsilon} + 0.143e^{-3\varepsilon}) \qquad \text{Eq. 79}$$

It is assumed that the nuclei are hemi-spherical in shape and they originate from the boundary and grow inwards. Consequently the volume of the recrystallizing nucleus is given by

$$V = \frac{1}{2}\left[\frac{4}{3}\pi\,\langle R_t\rangle^3\right] \qquad \text{Eq. 80}$$

where $\langle R_t\rangle$ is the radius of the spherical cap. The radius of the spherical cap evolves as:

$$\langle R_t\rangle = \langle R_0\rangle + \int_0^t M_{GB}\, G_t\, dt \qquad \text{Eq. 81}$$

where M_{GB} refers to the mobility of high angle grain boundary and G_t refers to the stored energy of deformation. Finally the recrystallized volume fraction is given by:

$$X_t = \frac{N_t V}{V_0} \qquad \text{Eq. } 82$$

3.1.3.3. Effect of precipitates on sub-grain growth and nucleation

As a first approximation, one may be inclined to use the standard Zener pinning argument to capture the effect of precipitation on the nucleation of recrystallization. This approach, however, is not suitable for two reasons. The first is that the nucleation step of recrystallization involves the rearrangement/annihilation of dislocations in order to create a viable recrystallization nucleus. In our model we capture this in terms of sub-grain growth. The interaction of particles with dislocations and sub-grain (low angle boundary) is fundamentally different from particle-boundary interaction described by Zener and as such a Zener description is not appropriate [13, 118, 138]. The second is that, the time evolution of the Zener pinning shows that the pinning force is not significant at early times of annealing and as such Zener pinning could not be responsible for the delay in the onset of recrystallization.

An alternative approach for describing the effect of particles on the nucleation of recrystallization is to incorporate their effect on the sub-grain growth step. It is expected that the sub-grain velocity will be inversely proportional to the number of precipitates. At the same time, the effectiveness of the precipitates as barriers to boundary motion will depend on temperature; as temperature increases, climbs becomes an increasingly more viable option for overcoming precipitate pinning. Based on these considerations, the sub-grain growth velocity is expressed as:

$$\nu = 2\frac{Db^2}{V_A} sinh\left(\frac{K_{ad}\sigma_D V_A}{k_b T}\right)\psi \qquad \text{Eq. 83(a)}$$

$$\psi = \left(\frac{\rho}{N}\right)\frac{1}{\lambda_0}\left(\frac{D_{self}}{D_0}\right) \qquad \text{Eq. 83(b)}$$

The first term in Eq. 83(a) represents the velocity of the sub-grain boundary in the absence of precipitation. This term was employed by Rehman et al [132] for the precipitate-free case with K_{ad} =2.35. The effect of precipitation enters through the term ψ, which has two components, the first represents the spacing of precipitates along the dislocation network, ρ/N, normalized by a characteristic distance, λ_0. The second term reflects the potential for climb and is expressed as the self-diffusion coefficient, D_{self}, normalized by a characteristic diffusion coefficient D_0. The values of λ_0 and D_0were identified by fitting the experimental data [130]; $\lambda_0.D_0$ = 1 x 10^{-22} m^3/s.

The proposed description for the effect of particles on the nucleation of recrystallization is very similar to that used to describe the effect of particles on recovery. This is not surprising given that both processes are essentially controlled by particle-dislocation interactions and both processes could be described in terms of the growth of dislocation cells or sub-boundaries. The new expression predicts that effect of particle pinning on the nucleation of recrystallization evolves with the number density of precipitates (as opposed to the volume fraction of precipitates in the case of Zener pinning). As a result, a significant pinning force can develop rapidly and retard recrystallization at early times leading to the experimentally observed incubation times. Under most circumstances the dislocation network will not be completely pinned and therefore the condition for grain boundary bulging will eventually be reached. Even in the case, in which precipitate number density is very large the delay of recrystallization nucleation will not necessarily be permanent because the onset of particle coarsening could eventually allow sub-grain growth to resume and nucleation to take place.

A subtle point concerning the effect of precipitation on the nucleation of recrystallization concerns the effect of particles on the nucleation criterion. In the precipitate free case, nucleation takes place as per Eq. 70. It is tempting to reduce ΔG_t by an amount equal to the Zener drag in order to reflect the effect of particle pinning. This was not done in this contribution because the particles formed on the boundary coarsen rapidly due to enhanced boundary diffusion and using the classical Zener expression would overestimate the contribution of particle pinning. We have therefore retained the above equation for nucleation criterion.

3.1.3.4. Pure Growth Kinetics

When the shell volume is completely consumed by the recrystallizing nuclei pure growth starts **Figure 21**. In this stage growth kinetics is modeled in terms of a uniform spherical shell of recrystallized material shrinking. Consequently the increase in shell thickness in time step dt is given by $\int_0^{dt} M_{GB}\ G_t dt$. The increase in recrystallized volume is given by;

$$dV = 4\pi R_t^2\ M_{Gb} G_t\ dt \qquad \text{Eq. 84}$$

where R_t is the radius of the non-recrystallized core. Finally, the overall recrystallization kinetics (X_t) during pure growth is given by

$$X_t = 1 - \frac{\frac{4}{3}\pi R_t^3}{V_0} \qquad \text{Eq. 85}$$

where, V_0 is the initial deformed grain volume.

3.1.3.5. High angle boundary mobility

The recrystallization growth kinetics model employs a term M_{GB} which is the high angle grain boundary mobility. It is proportionality constant between boundary velocity and driving force with the units $m^4/J\ s$.

For pure material, the high angle boundary mobility is the highest, a reasonable estimate of which can be calculated from the Turnbull estimate as calculated in Eq. 17. However in the present case of microalloyed austenite, we have taken mobility of HAGB in C-Mn steel as pure. Although significant boundary retardation is expected from Mn, yet it is excluded from the present analysis as Mn is almost always present in all steel grades except in some special cases such as interstitial free steel etc. Consequently mobility as calculated from experimental study of grain coarsening by Zhou et al. [115] on C-Mn steel is used in the present case;

$$M_{C-Mn} = \frac{0.1920}{T} \exp\left(-\frac{20837.14}{T}\right) \qquad \text{Eq. 86}$$

The retardation of the boundary due to solute Nb is captured using Cahn's solute drag model as expressed below;

$$\frac{1}{M_{GB,eff}} = \frac{1}{M_{pure}} + \alpha_m C_{Nb} \qquad \text{Eq. } 87$$

where,

$$\alpha_m = \frac{\beta\, N_V (kT)^2}{E_b\, D_X} \left(sinh\left(\frac{E_b}{kT}\right) - \frac{E_b}{kT} \right) \qquad \text{Eq. } 88$$

β is the grain boundary thickness (~1 nm), N_V is the number of atoms per unit volume, E_b is the solute-boundary binding energy (20 kJ/mol) and D_X is the trans-interface boundary diffusion which is equal to twice the bulk diffusion coefficient of Nb in austenite [132].

Originally in Cahn's model M_{pure} refers to mobility of pure material. As is explained in the previous paragraph mobility of C-Mn steel is used here.

The effect of solute Nb enters into the model through E_b (binding energy) and D_X (cross boundary diffusion coefficient). Compared to D_X , E_b is well known with estimates varying between 20-38 kJ/mol. For cross boundary diffusion coefficient a value twice the bulk diffusion value produced the best fit of experimental results as discussed in section 4. This is in agreement with other published literature [5, 139].

3.1.3.6. Driving force for Recrystallization growth

Driving force for recrystallization is the stored energy of deformation between recrystallization and non-recrystallization region and is often expressed as:

$$G_t = \frac{1}{2}\rho\mu b^2 \qquad \text{Eq. 89}$$

Reproducing the recovery model as described in section 3.1.1 gives us;

$$\frac{d\sigma_D}{dt} = -\frac{64\sigma_D^2 \upsilon_d}{9M^3\alpha E} exp\left(-\frac{U_a}{k_b T}\right) sinh\left(\frac{\sigma_D V_a}{k_b T}\right)\left(1-\frac{n_{ppt}}{n_c}\right) \qquad \text{Eq. 90}$$

In the above equation V_a is activation volume, which relates to activation distance which is the pinning distance or the length of the intrinsic dislocation pileup.

Using Eq. 90 and Eq. 50 stress evolution σ_D can be evaluated which in turn can be used to calculate dislocation density evolution using Forest-Hardening relationship.

$$\sigma = \alpha\, M\, \mu\, b\, \sqrt{\rho} \qquad \text{Eq. 91(a)}$$

$$\rho = \left(\frac{\sigma}{\alpha\, M\, \mu\, b}\right)^2 \qquad \text{Eq. 91(b)}$$

The effect of precipitates on growth of recrystallizing grains is captured in terms of the classical treatment of Zener [103] as modified by Gladman [4]. A planar boundary will intersect particles within a distance r of it, where r is the particle diameter. Hence the number of particle intersecting the unit area of the boundary is

$$N_s = 2rN_v \qquad \text{Eq. 92}$$

where, N_v is the number of particles per unit volume. For a randomly distributed particles of radius r and volume fraction of F_v , the number of particles per unit volume is:

$$N_v = \frac{3F_v}{4\pi r^3} \tag{Eq. 93}$$

Maximum drag force experienced by the boundary by a single particle is $\pi r\gamma$. Hence the total drag force experienced by the boundary by a distribution of particles is:

$$P_z = N_s F_s = \frac{3F_v\gamma}{2r} \tag{Eq. 94}$$

Zener's pinning equation is very important as it highlights that for a constant volume fraction of second phase particles; smaller size particles are more effective in retarding HAGB motion than a coarser one. The Zener approach sometimes gives a pinning value different from what is observed experimentally. The discrepancy is attributed to the fact that the basic assumptions made related to geometry of the second phase particles, interaction zone between the particles and grain boundary, the particle distribution related to spatial and size, and the relationship between the boundary curvature and the grain radius may not be the same for every rolling condition [102]. In the present work we have used Zener force four times the classical value given by Eq. 94. This gave us a better fit to the experimental data. However to get a more accurate Zener calculation one can measure the precipitate size through TEM and feed it back into the model. Once recrystallization has nucleated the high angle boundary created continues to grow with a velocity given by Eq. 95 [12];

$$V = M_{GB}(P - P_z) \tag{Eq. 95}$$

where, M_{GB} is the HAGB mobility, P is the stored energy of deformation and P_z is the Zener drag.

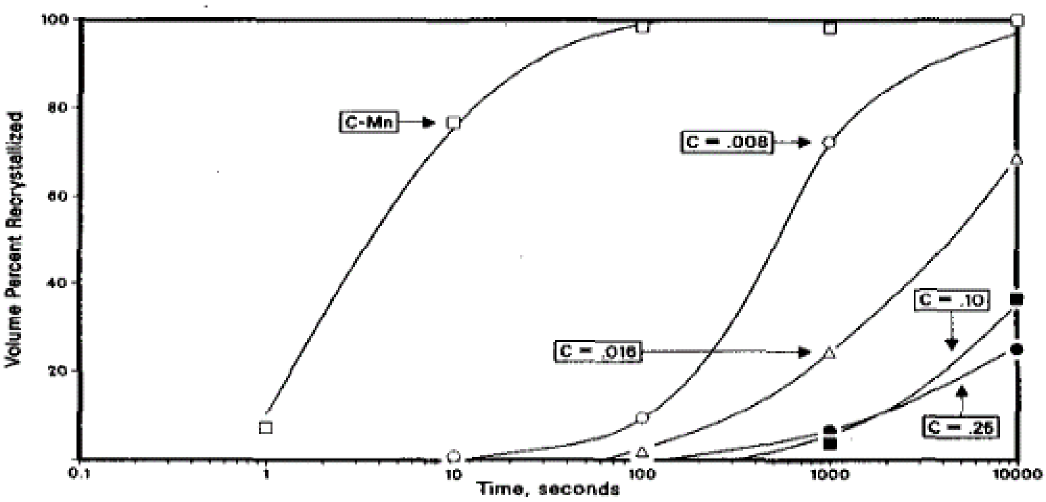

Figure 24: Austenite recrystallization kinetics in steel containing 0.05% Nb at 899°C at a strain of 50% with strain rate of 10.2 s-1[93]. Note the increase in incubation time with an increase in precipitation.

Special consideration needs to be given to the case in which the pinning force in Eq. 95 is greater than the driving force for recrystallization. This is often the case at long times due to the depletion of the driving force by recovery and simultaneous increase of the Zener term due to the increase in volume fraction of precipitates. Experimentally it has been observed that at long annealing times the sample recrystallizes at a very slow rate (see **Figure 24**). According to Eq. 95, the growth rate should go to zero when the net driving force $(P - P_z)$ goes to zero. This stoppage, however, is not permanent because particle coarsening will lead to the dissolution of some particles and this would permit the boundary to migrate locally even when the global pinning force is greater than the global driving force.

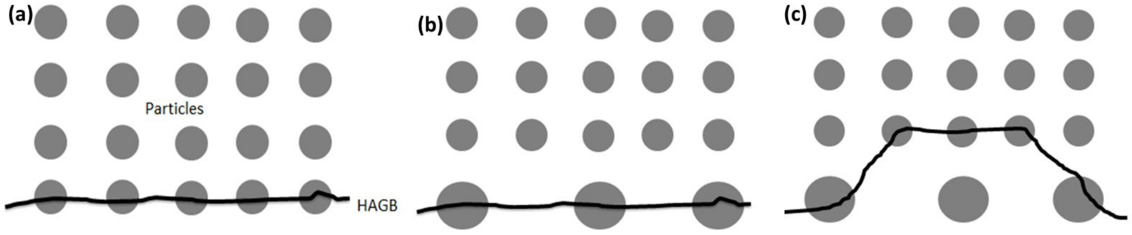

Figure 25: Schematic of the sequence of events that would lead to the advance of the recrystallization boundary (a) At time $t = 0$ when the grain boundary is completely pinned, (b) At time $t = t'$ when the boundary is unpinned as particles coarsens (c) at time $t = t_{up}$ when the boundary advances one step further and gets pinned.

In **Figure 25**(a) the HAGB movement is completely pinned by the precipitates. Accelerated coarsening of the particles located on the grain boundary will lead to a local reduction in the pinning force and the boundary is able to advance (locally), until it encounters a sufficient number of fresh particles which will ensure that the boundary is pinned again. The process repeats leading to a progressive growth of the recrystallizing grains at a very slow rate. At this moment this is a hypothesis but the sequence of events seems to be quite plausible in explaining the experimental database shown in **Figure 24**.

The coarsening of particles located on a high angle boundary was described by Kirchner [140] and Doherty et al.[141]:

$$\bar{r}_t^4 - \bar{r}_0^4 = c\ t \qquad \text{Eq. 96(a)}$$

$$c = \frac{9}{32} w D_{gb} \sigma N_{\alpha}(gb) V_m \left(\frac{1}{ABRT}\right) \qquad \text{Eq. 96 (b)}$$

$$A = (2/3) + (\sigma_b/2\sigma) + (1/3)(\sigma_b/2\sigma)^3 \qquad \text{Eq. 96(c)}$$

$$B = \frac{1}{2} ln\left(\frac{1}{f_b}\right) \qquad \text{Eq. 96(d)}$$

where $N_{\alpha}(gb)$, is the solute content at a grain boundary in equilibrium with an infinitely large precipitate, w is the grain boundary thickness, V_m is the molar volume, $D_{gb}$is the grain boundary diffusion coefficient. σ_b is the grain boundary energy and f_b is the fraction of grain boundary covered by the precipitates. Using the Kirchner model [140] to calculate the coarsening rate along the HAGB and the inter particle spacing, time evolution of the local Zener drag along with the velocity of the HAGB can be calculated. This is further explained below.

When the global precipitate volume fraction of a given particle size exceeds a certain critical value the total Zener drag given by those is larger than the total available driving force for recrystallization. Consequently recrystallization is pinned down. At time t=0.

$$P_Z \geq G_R \qquad \text{Eq. 97}$$

Due to the accelerated coarsening taking place along the HAGB, the boundary becomes locally unpinned. The radius of particle at the point of unpinning can be calculated by equating Zener force and recrystallization driving force:

$$r = \frac{6\gamma F_v}{\rho \mu b^2} \qquad \text{Eq. 98}$$

The time taken for this unpinning to happen $\mathrm{t'}$ can be calculated from Eq. 96(a) to Eq. 98.

$$t' = \frac{r^4 - r_0^4}{c} \qquad \text{Eq. 99}$$

At time $\mathrm{t \geq t'}$, wherein the HAGB has been unpinned, the boundary travels a distance "λ' " which is the inter-particle spacing, where it becomes pinned again.

$$\lambda' = \frac{1}{\sqrt[3]{N}} \qquad \text{Eq. 100}$$

where, N is the precipitate number density per unit volume and is calculated as per Dutta and Sellars model [15]. $\mathrm{t_{up}}$ is the time taken for the boundary to move the distance λ where the HAGB becomes pinned again. From conservation principles the following equation can be solved to obtain $\mathrm{t_{up}}$

$$\lambda = \int_{0}^{t\prime} M_{HAGB}(0)dt + \int_{t\prime}^{t_{up}} M_{HAGB}(G - Z')dt \qquad \text{Eq. 101}$$

The first integral in the above equation becomes zero.

$$Z' = \frac{3\gamma F_v}{(r_0^4 + ct)^{\frac{1}{4}}} \qquad \text{Eq. 102}$$

The high angle boundary velocity can now be calculated in order to obtain the recrystallization kinetics.

$$V = \frac{\lambda}{t' + t_{up}} \qquad \text{Eq. 103}$$

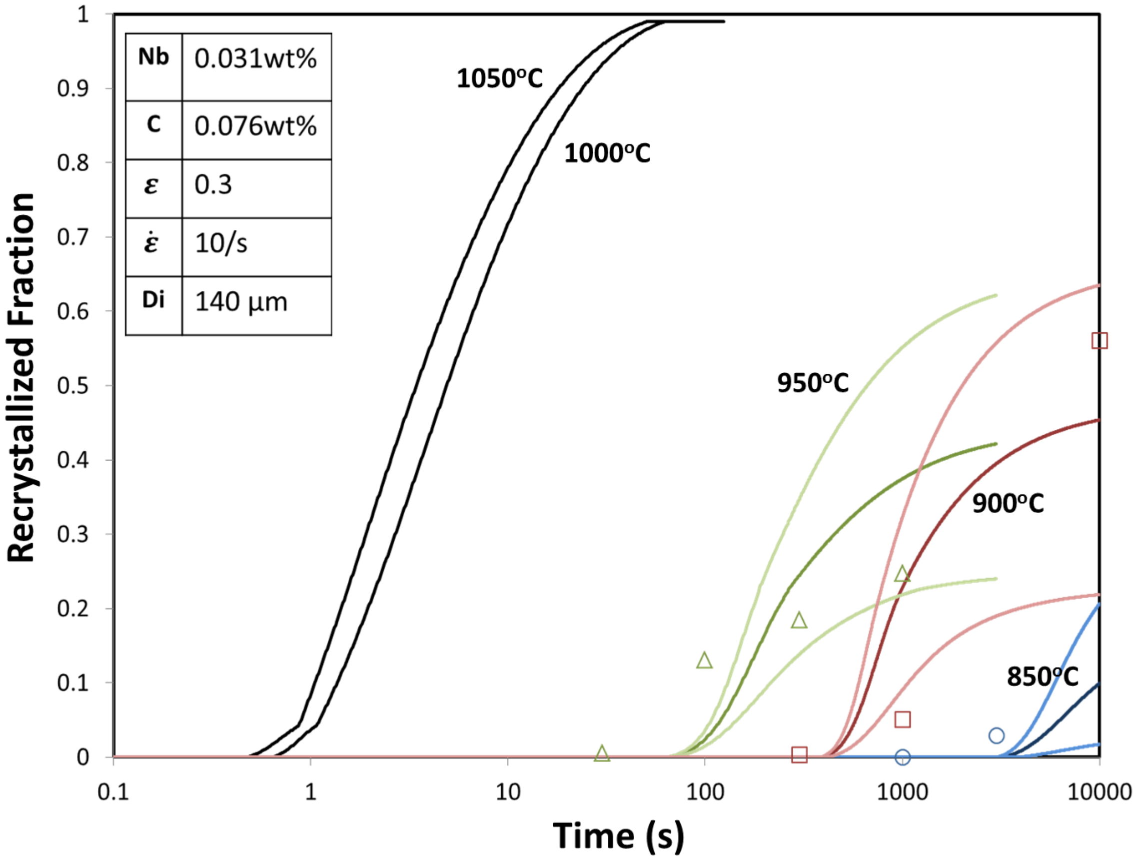

Figure 26: A range of possible recrystallization growth kinetics, based on the use of various values of the fitting parameters of the precipitation growth and coarsening model.

3.1.4. Grain Coarsening

In section 2.4, a review of grain coarsening models has been presented. Once recrystallization is complete, coarsening of fine grains starts, to minimize energy associated with grain boundary. In what follows we have used a simple model assuming that the coarsening behaviour remains self-similar. Reproducing Eq. 46, grain coarsening is given by

$$\frac{dR}{dt} = M_{GB}\left(\frac{\alpha\gamma_{gb}}{\bar{R}} - \frac{3F_V\gamma}{2r}\right) \quad \text{Eq. 104}$$

The key problem in using the above equation is to have a correct estimation of grain boundary mobility (M_{GB}) and Zener drag ($\frac{3F_V\gamma}{2r}$). Correct estimation of Zener drag using microscopy is difficult due to magnitude of the number density of precipitates (10^{20} /m^3) and the size resolution of TEM. Hence, M_{GB} is usually used as a fitting parameter, leading to non-reproducibility of grain coarsening models among various studies. In what follows we have argued that M_{GB} is a grain boundary parameter and should be independent of operating process viz. either recrystallization and grain coarsening hence effective mobility $M_{GB,eff}$ as calculated from Cahn`s model in recrystallization module, which contains intrinsic mobility calculated from grain coarsening experiments on C-Mn steels by Zhou et al. [115]has been used here in grain coarsening model. Similarly Zener drag (P_z), is calculated from the precipitation module. This allows the current grain coarsening module to be predictive.

3.1.5. Calculation of fitting parameters

As with all the modeling work, there are varieties of parameters whose values are not reliably known in the domain of strain, solute content and operating temperature. These parameters such as activation volume of the recovery model, cross boundary diffusion coefficient, subgrain boundary mobility necessitate the use of experimental data to back calculate the constants in the model. Towards this goal we have used a step by step approach to first calculate the simple parameters and then increase the complexity. The experimental database published using torsion based stress relaxation studies were discarded from consideration due to the presence of strain and strain rate gradient in the radial direction which will introduce additional effects.

For the calculation of parameter K_1 in the subgrain growth model and in activation volume for recovery calculation Eq. 49, experimental database of Kwon and DeArdo [130] at 1000^{o}C and 900^{o}C was used. For the case of 900^{o}C dynamic recrystallization was not reported and hence the database could be used to calculate K_{ad} in the subgrain growth equation (Eq. 69). To calculate K_2 in Eq. 49, again Kwon and DeArdo [130] database for a 0.042 wt % Nb steel deformed at 1000^{o}C was used. Under these conditions precipitation is possible but its kinetics at this temperature will be far slower than that of recrystallization. Fitting this data allowed calculation of parameter K_2. The fit is reproduced in **Figure 27**. These values of K_1, K_2 and K_{ad} were further refined by simultaneously fitting all of the available experimental data.

3.2. Model Validation

The experimental literature on recrystallization of micro-alloyed steels is very vast. In what follows we have only used experimental data wherein optical metallography was used to measure the recrystallization kinetics or at least used in conjunction with the mechanical tests to determine recrystallization kinetics. We have intentionally discarded experimental database generated solely from torsional studies as the presence of strain gradient within the specimen is unavoidable and hence does not reveal the true picture. The model predictions are shown in **Figure 27-Figure 33** for temperatures ranging between 900°C to 1050°C. In addition results from other researchers have been used, notably those of Yamamoto et al. [29] and Kang et al.[129] as they have also used optical metallography along with double-hit compression tests. The softening data were fitted using the 2% offset method [84] which is defined as:

$$S = \frac{\sigma_1 - \sigma_3}{\sigma_1 - \sigma_2} \qquad \text{Eq. 105}$$

σ_1 is the flow stress which is obtained by extrapolating the stress–strain curve during the first deformation by 2%. It represents the flow stress of the as-deformed material. σ_2 is the stress obtained corresponding to strain of 2% in the original stress strain plot. This represents flow stress of the completely recrystallized material. And, σ_3 is the stress obtained from the second deformation at 2% strain and represents the flow stress of the partially softened material.

The flow stress for the as-deformed material as a function of processing parameters, grain size and solute content is calculated using Yoshie’s equation.

$$\sigma = 22.7\,\varepsilon^{0.223}\dot{\varepsilon}^{0.048}D_{\gamma}^{-0.07}exp\left(\frac{2880}{T}\right)exp(3.01\,C_{Nb}) \qquad \text{Eq. 106}$$

The calculation of σ_3 from the microstructure model is done using the method described by Zurob et al[5]. The chemistries of the alloys tested are given in **Table 3**. **Figure 27** to **Figure 42** shows the model prediction for recrystallization/softening kinetics and **Figure 31** to **Figure 33** shows the model prediction for austenite grain coarsening kinetics.

Alloy [Ref]	C	Si	Mn	P	S	Nb	Al	N	Ti	Mo
N1[130]	0.1	0.46	1.6	0.004	0.006	0	0.01	0.008		
N2 [130]	0.1	0.46	1.6	0.004	0.006	0.042	0.01	0.008		
N3 [29]	0.002	0.29	1.54	0.005	0.006	0.05	0.033	0.0023		
N4 [29]	0.002	0.25	1.5	0.005	0.006	0.097	0.033	0.0027		
N5 [129]	0.076	0.06	1.34	0.005	0.002	0.03		0.0061		
N6 [122]	0.04	0.22	1.75			0.1	0.03	0.004	0.015	
N7 [119]	0.05	0.04	1.88	0.005	0.007	0.048	0.05	0.004		0.49

Table 3: Alloy compositions (weight percent) used to validate the model.

Remarkably all the predicted curves are in good agreement with the experimental values, which strongly supports the model.

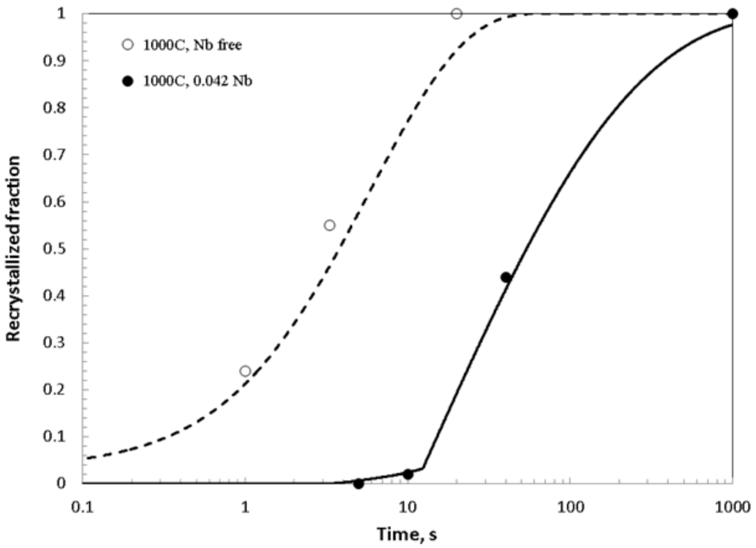

Figure 27: Predicted and experimentally measured recrystallized fraction for steel N1 and N2 [130] at 1000°C (strain = 0.3, strain rate = 0.1 s^{-1}). Note the effect of solute niobium on recrystallization kinetics.

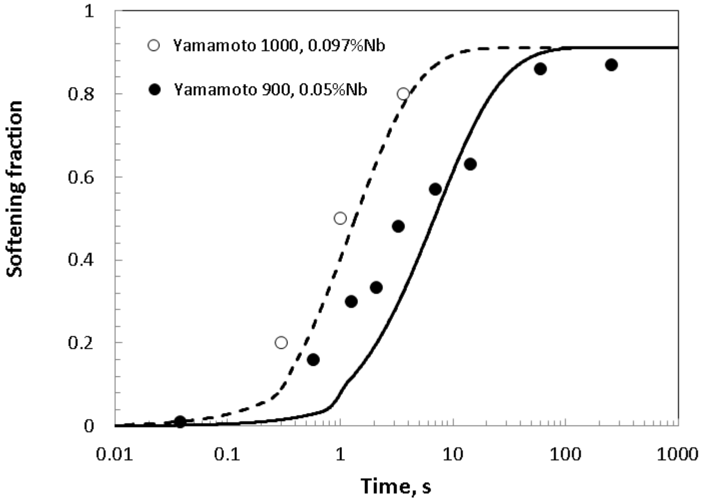

Figure 28: Predicted and experimentally measured softening fraction for alloy N3 and N4 (strain = 0.69, strain rate = 10 s^{-1})[29].

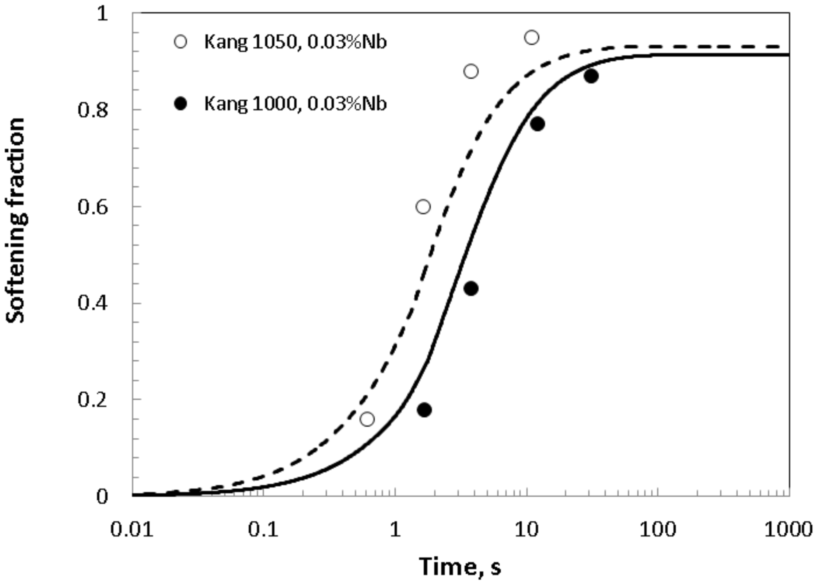

Figure 29: Predicted and experimentally measured softening fraction for alloy N5 [129] (strain = 0.3, strain rate = 10 s^{-1}).

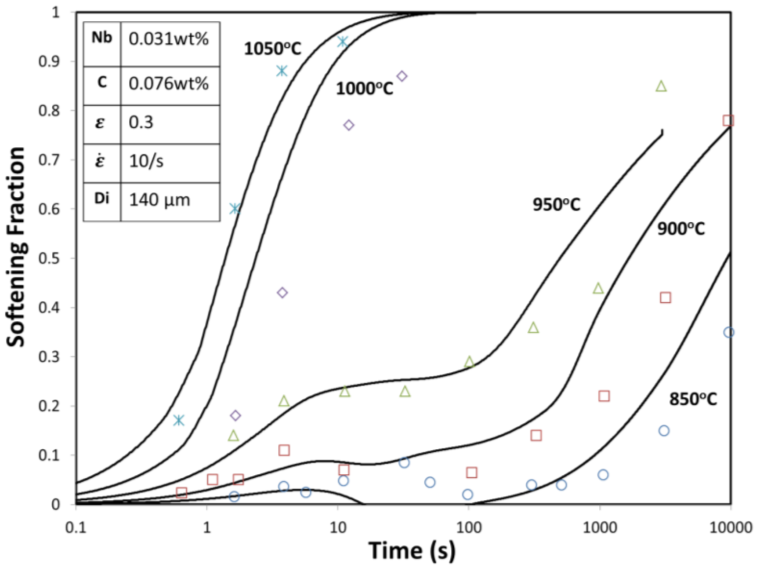

Figure 30: Predicted and experimentally measured softening fraction for alloy N5 [129].

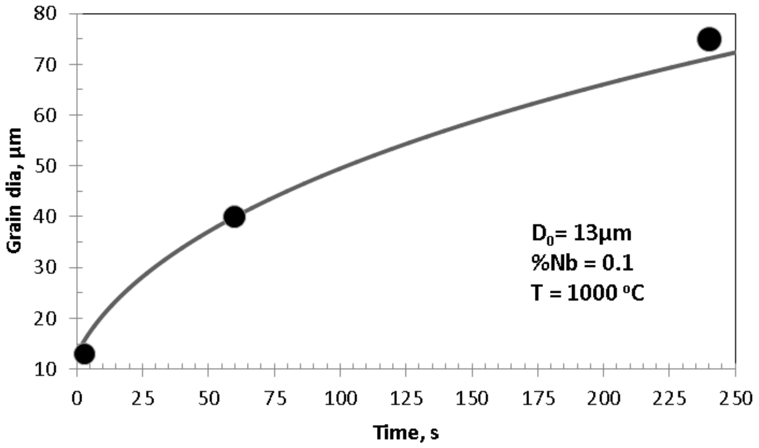

Figure 31: Predicted and experimentally measured coarsening kinetics of austenite grains for alloy N6 at 1000^{o}C coarsening[122].

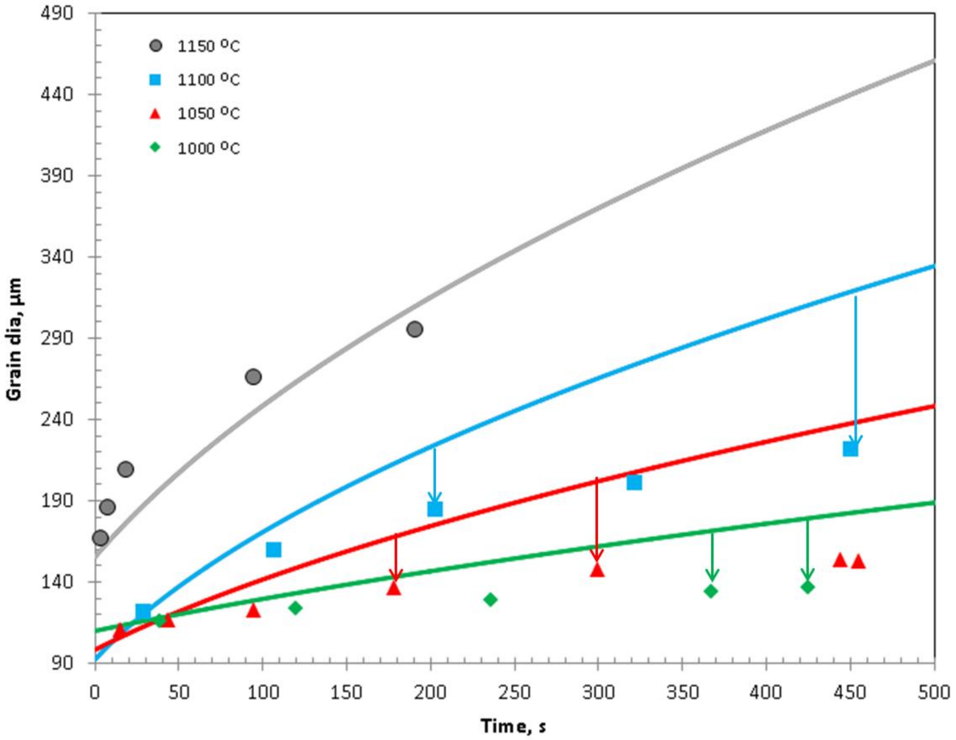

Figure 32: Predicted and experimentally measured coarsening kinetics of austenite grains for alloy N7[119] at 1150^{o}C, 1100^{o}C, 1050^{o}C and 1000^{o}C. The deviation from predicted to actual is shown by arrows. Its clear that deviation at lower temperatures are more pronounced,which can be attributed to the solute drag effect of 0.49 wt % Mo which the present model does not take into consideration.

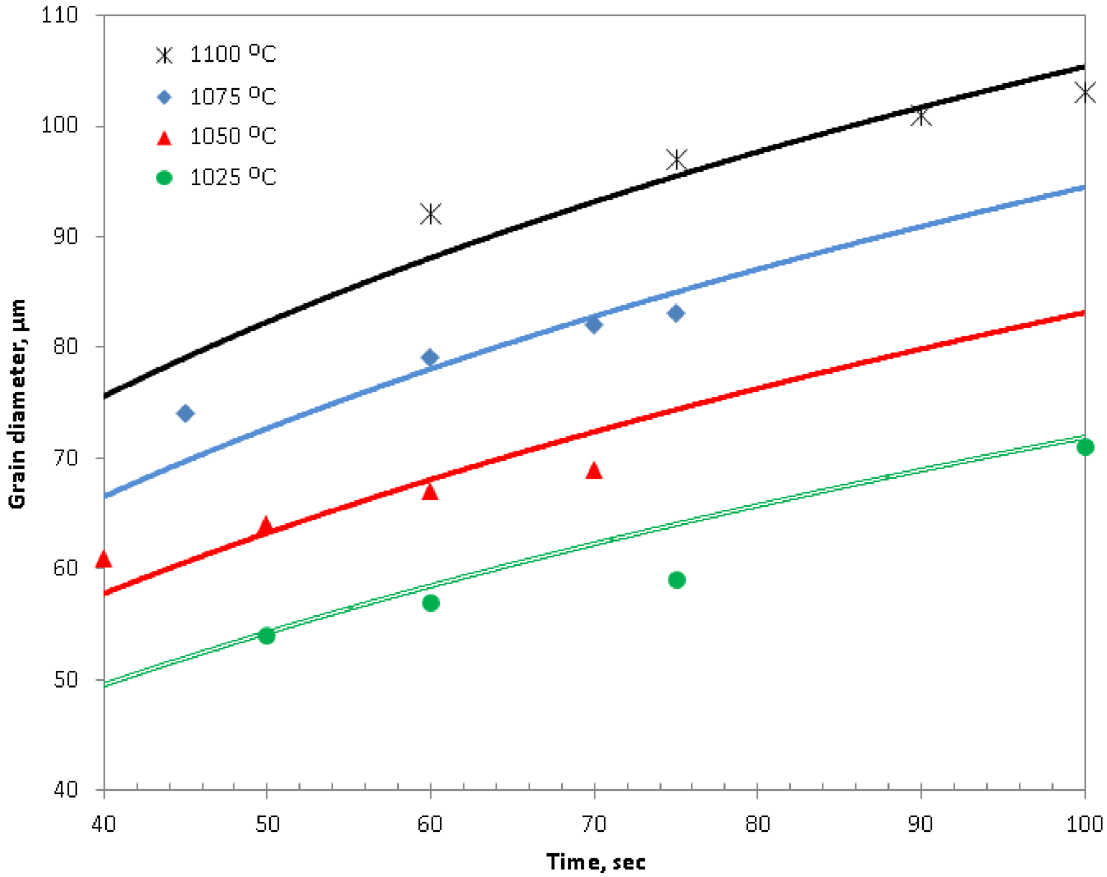

Figure 33: Comparison of model prediction of coarsening kinetics of austenite grains for a 0.05 Nb alloy at various temperatures with the database reported by Hodgson et al.[9, 10].

3.3. Multi Pass Modeling

The model described in the previous section calculates microstructure evolution after single pass deformation. However, all commercial steel rolling operation involves a series of deformation given in successive passes which are separated by some time intervals.

Due to the difficulty and in some cases the impossible nature of sampling from industrial rolling mill, researchers use lab scale knowledge to extract various trends and dependencies which can then be exploited in actual operation.

In what follows we have attempted to extend the single pass deformation model to multi pass and have analyzed a typical hot strip mill rolling schedule in this light.

3.3.1. Average method

In this method the entire microstructural parameters are treated as having an average value. At the start of each deformation pass an average value of the microstructure is calculated which is then used as an input to the single pass deformation model [10, 142-144]. Sellars [19] argued that this is a valid approach as it is self-reinforcing. That is to say that the region which remains non-recrystallized at the beginning of second pass deformation will have increased local strain after deformation leading to increased recrystallization kinetics compared to the region which was completely recrystallized before second pass deformation. Sellars further argued that the microstructure evolves in such a way so as to minimize the total inhomogeneity at any given instant.

In literature, this approach as well as minor variations of it, remains the most widely used methodology to extend a single pass model to a multi-pass one. Sellars et al [19]used a law of mixture approach wherein it is assumed that recrystallized fraction X, after first pass deformation, will recrystallize independently with a strain of ε_2 (second pass deformation strain) after second pass deformation, whereas the non-recrystallized fraction (1-X) after first pass will recrystallize with a strain of $\varepsilon_1 + \varepsilon_2$. Militzer[145] in his review paper of multi pass modeling argues that in the context of industrial processing this approach is quite pragmatic given the statistical noise in data collection. The overall kinetics is then obtained by calculating the weighted average of the volume fraction by its fractional softening. This strategy works well, when either the interpass time is less or the rolling temperatures are low as the recovery kinetics is inherently assumed to be negligible when adding the two strains together in the non-recrystallized region. The next improvement in this approach was due to Hodgson, Gibbs, Ibabe, Jonas et al. [10, 142, 143, 146]by taking into consideration the effect of recovery by introducing a factor before ε_1 .

$$\varepsilon_{eff} = \varepsilon_2 + \varphi(1 - X)\varepsilon_1 \qquad \text{Eq. 107}$$

They demonstrated in their experiments that for short interpass time, low temperature and high Nb content λ approaches unity. For C-Mn steels they found ϕ to be close to 0.5 under typical processing conditions [10, 142, 143, 146].

For the effective grain size calculation Pereda et al. [110] proposed to use the recrystallized grain size as the effective grain size. The assumption is quite reasonable as in commercial rolling during intermediate deformation passes the average grain size is quite small and the number density of recrystallized grains are much higher than that of non-recrystallized ones, due to which the number-averaged grain size is closer to the recrystallized grain size[110]. On the other hand, Sellars et al. [19] treated the two regions (recrystallized and non-recrystallized) as separate microstructure, the grain size of which evolves independently. Fulvio and Jonas [142]used a geometrical consistent approach and used the following relationship.

$$d_{o,i+1} = d_{rex,i}\, X_i^{\frac{4}{3}} + \ d_{o,i}(1 - X_i)^2 \qquad \text{Eq. } 108$$

where, $d_{rex,i}$ is the recrystallized grain size after rolling pass i, $d_{o,i}$ is average grain size entering pass deformation i and $d_{o,i+1}$ is the effective average grain size entering deformation pass $i + 1$.

3.3.1.1. Modeling Framework

Flow Stress: The approach we have taken to model multi-pass slightly defers from what is discussed in the previous section. The decay in flow-stress due to various softening mechanisms is calculated using the approach mentioned in section 3.2 [132]. The flow stress before second pass deformation has been used to calculate the retained strain in the microstructure. To this retained strain the second pass strain is added. This total strain gives the initial stored energy after second pass deformation which is used for softening kinetics calculation after second pass.

Equivalent grain size is calculated using the above uniform softening equation Eq. 108. The equations developed here are for isothermal conditions. However, discretizing temperature with respect to time one can extend the model for non-isothermal conditions. Using this approach we have modeled the microstructure evolution in multi pass rolling and have analyzed typical rolling schedules for conventional strip rolling as discussed in section 5.1.

The key complication in extending the single pass model to multi-pass is the treatment of partial recrystallization regime. In partial recrystallization, the microstructure is composed of non-homogeneous mixture of soft (recrystallized) and hard (work hardened) grains. When deformation is applied to this composite microstructure, the challenge is to partition applied strain in the hard and soft regions. Conventionally either iso-stress or iso-strain conditions are used but they are not strictly applicable, as the softer grains deform more compared to work hardened grains. We tried to address this by using a fractional softening based approach as detailed in section 3.2. Another pertinent issue in treatment of partial recrystallization with mean field based approach is lack of detail of spatial distribution of strain across the microstructure. In other words, consider a case of partial recrystallized microstructure wherein the stored energy (strain) in work hardened grains is just below the critical strain for recrystallization. A small deformation in next pass rolling will be sufficient to trigger recrystallization in these work hardened grains, as they will easily overcome the critical strain required. However the effective stored energy (effective strain) calculated by averaging it over the entire microstructure will be lower than what is present in the work hardened grains. A case may arise that a second pass deformation when applied, the work hardened grains would have recrystallized whereas the calculations would show no recrystallization as the effective stored energy (strain) is lower than the critical value needed for recrystallization. This will lead to erroneous results. We have tried to analyze this situation by using a similar modeling framework as reported by Sellers and Whiteman [19], wherein the recrystallized and non-recrystallized regions are treated separately for next pass deformation.

In spite of the various modeling approaches taken tracking the microstructure evolution and its modelling in case of partial recrystallization is difficult which is further exacerbated due to stochastic nature of the problem. Consequently, the trend in commercial rolling of microalloyed steels is to completely avoid this scenario by not rolling in that temperature window, as partial recrystallization has been associated with poor fracture properties by creating non-homogeneous microstructure. The new concept of O-HTP (optimized high temperature processing) of Nb microalloyed steels[3] and HOP process for seismic grade line pipes[147, 148], demonstrates that rolling should not be done in partial recrystallization window for enhanced mechanical properties hence evolution of microstructure during deformation in partially recrystallized condition becomes ineffective from industrial processing scenario.

Since the model predicts the flow stress evolution[149] we have used this to predict rolling forces using Sim's model[150], the details of which are given in Chapter 9.

3.3.2. Quasi-Mean field approach

As a means of incorporating the distribution of physical parameters (strain, grain size etc) a modified version of a mean field model has been employed:

This approach is largely based upon the work of Cram et al. [134]. In this approach, a polycrystalline microstructure is represented by a set of grains embedded in a medium with average properties same as that of the bulk material state properties such as grain size, dislocation density etc are assigned to each of the grains.

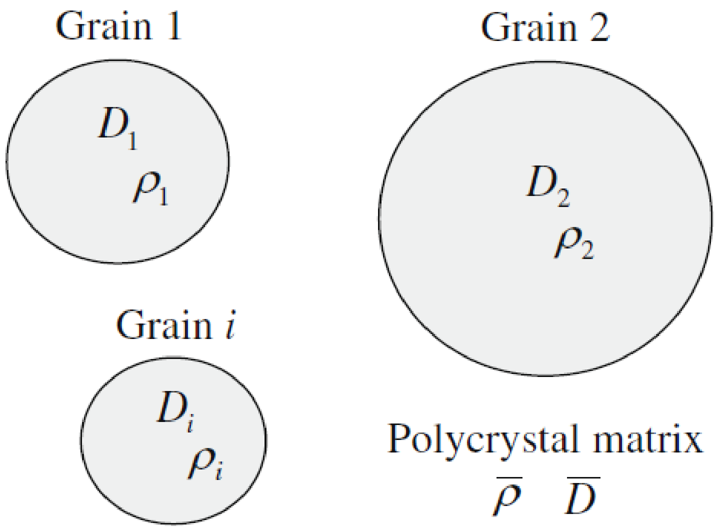

Figure 34 : Schematic diagram of grains immersed within an average matrix. Di is the grain size and ρ_i is the dislocation density[134].

In the present case we have created a distribution of grains and assigned an initial value to them. Once deformation is applied to the grain ensemble, the macroscopic strain applied is partitioned into each grain using the Iso-Work principles developed by Bouaziz et al.[151]. The idea behind this is that each grain deforms to a strain $\boldsymbol{\varepsilon_i}$ such that the total work done by all the grains remains the same. In other words

$$d\varepsilon_i = \frac{K}{\sigma_i} \qquad \text{Eq. 109}$$

where K is the work done by each grain and the subscript i represents the grain index. In this description the softer grains deform more compared to the harder grains. The partitioning occurs in such a way that the total macroscopic strain remains conserved.

$$\varepsilon_{mac} = \frac{\sum V_i d\varepsilon_i}{\sum V_i} \qquad \text{Eq. 110}$$

where V_i is the volume of grain i.

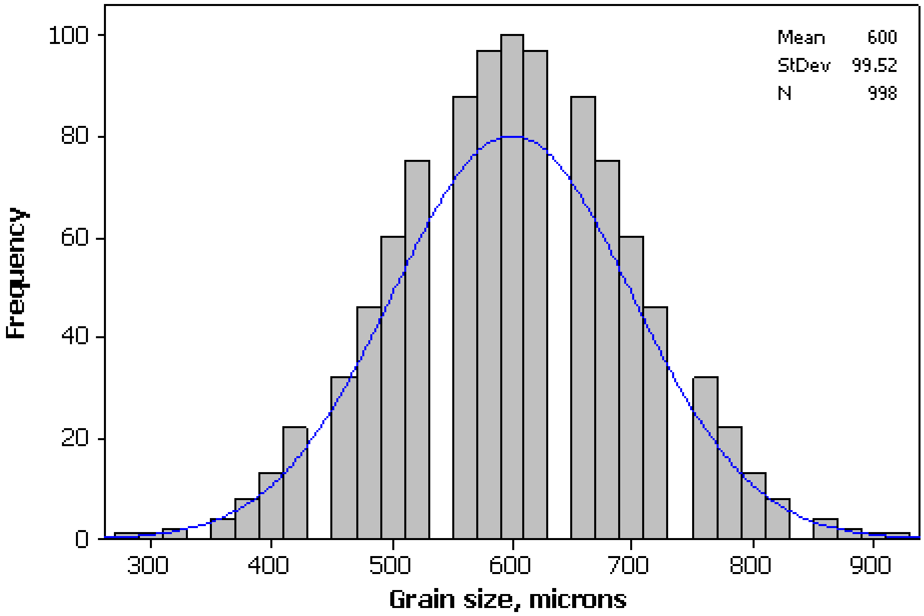

Figure 35: Plot of grain size distribution entered into the model. The mean grain size is 600μm having a standard deviation of 99.52 μm with the maximum and minimum size being 925 μm and 275 μm.

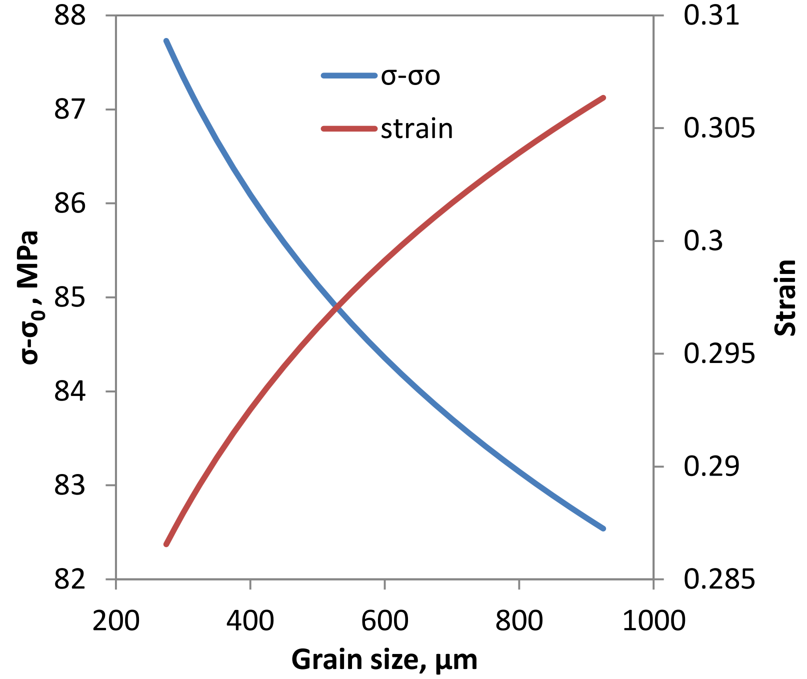

Figure 36: Strain and plastic stress (stress due to dislocation) of the grains when the ensemble was deformed to a macroscopic strain of 0.3 at a rate of 10/sec at 1100 ^{o}C having 0.05 Nb. The starting grain size distribution is shown in **Figure 35**.

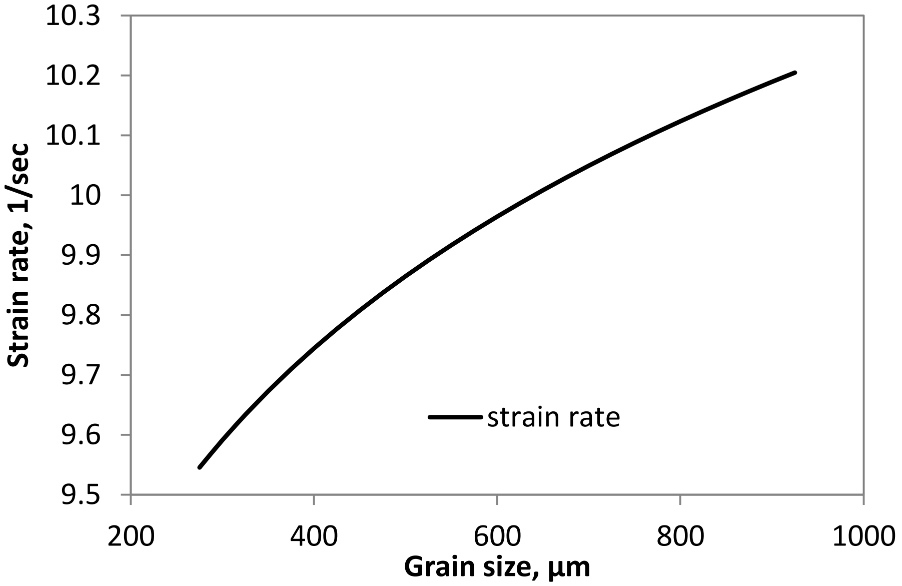

Figure 37: Strain rate experienced by each grain when the ensemble was deformed to a macroscopic strain of 0.3 at a rate of 10/sec at 1100 ^{o}C having 0.05 wt % Nb.

A grain ensemble of 998 grains having 0.05 Nb was created having a mean grain size of 600 µm with a standard deviation of 99.52 µm. The maximum and minimum grain sizes in the distribution are 925 µm and 275 µm **Figure 35**. The grain ensemble was subjected to a strain of 0.3 at a strain rate of 10s^{-1}. Using Iso-Work principles the macroscopic strain applied partitions in such a manner that the total work done remains the same. **Figure 36** shows the microscopic plastic stress and the corresponding strain of each grain. The microscopic strain and macroscopic strain rate applied determines the microscopic strain rate experienced by each of the grain as shown in **Figure 37**.

During first pass deformation, the larger grains are softer (as yield stress is low, hall-petch relationship) and hence deform more. This decides the microscopic stress for each grain at the end of deformation which is then used to calculate the recovery kinetics for each grain separately using Eq. 111.

$$\frac{d\sigma_{D,i}}{dt} = -\frac{64\sigma_D^2 \upsilon_d}{9M^3\alpha E} exp\left(-\frac{U_a}{k_b T}\right) sinh\left(\frac{\sigma_D V_a}{k_b T}\right)\left(1-\frac{n_{ppt}}{n_c}\right) \qquad \text{Eq. 111}$$

Figure 38 shows the recovery kinetics for the smallest and largest grain. The plot for rest of the grains lies between the two curves. The difference between the plastic stress as a function of grain size after deformation is shown in **Figure 36** . This initial difference in stress leads to the difference in recovery kinetics at earlier times as is shown in **Figure 38**. Since recovery kinetics is proportional to the initial stress, it causes accelerated decay in higher stressed ones, leading to similar value of stress among all the grains at later times. This observation is in line with Sellars [19] statement that *microstructure evolves in such a way so as to cancel the inhomogeneity between them*.

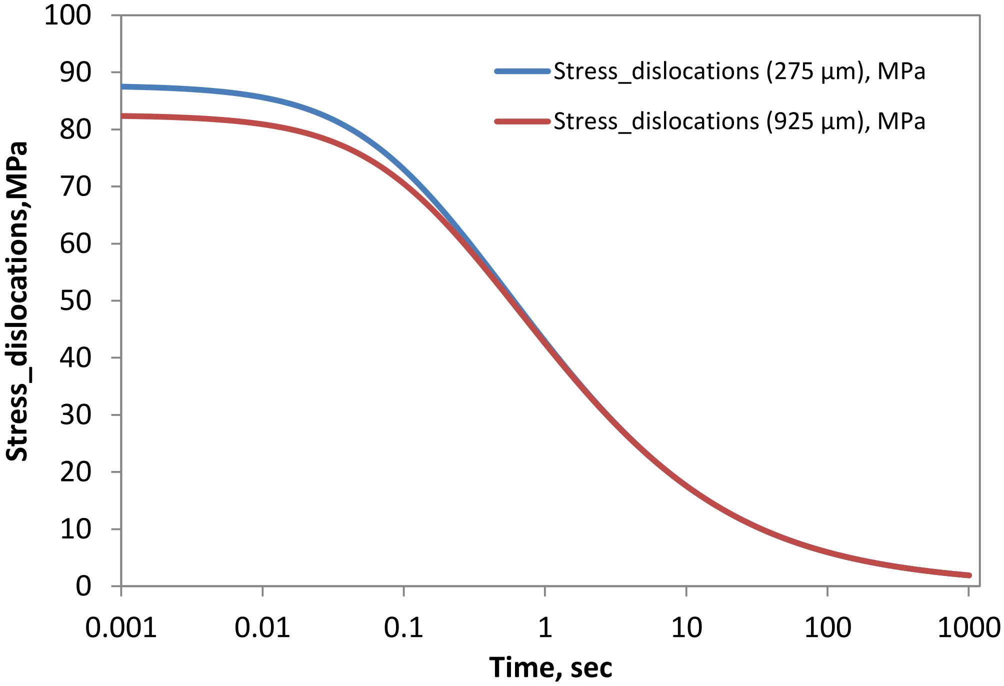

Figure 38: Stress relaxation due to recovery for the largest and smallest grains in the distribution. The plot for intermediate sizes lies between the two curves.

Recrystallization is modeled using the same approach as described in Section 3.1.3. Nucleation is calculated using Bailey Hirsch criterion for all the grains.

$$\boldsymbol{r_{c,i} = \frac{2\gamma}{G_i}}$$

Eq. 112

Similarly the recrystallization kinetics is calculated for the entire ensemble of grains. **Figure 39** shows the evolution of microscopic recrystallization volume fraction evolution for the smallest and the largest grain. Similarly to **Figure 38** the recrystallization kinetics for other grains lies between the two. The macroscopic volume fraction of recrystallization will be the volume average for each grain. The distribution of recrystallized grains is shown in **Figure 41**. Comparing **Figure 41** and **Figure 35** one would observe that due to recrystallization the mean grain size and its standard deviation both have reduced considerably.

In Figure 40, one would observe significant difference in recrystallization kinetics for the largest and the smallest grains. However upon close scrutiny this doesn't appear to be the case. Recrystallization progress depends upon driving force and boundary mobility. The plot of stress (driving force) evolution for the two grains is shown in **Figure 38**. As recovery rate is proportional to the initial stress, hence the initial difference in stress is eliminated with the progress of recovery. Mobility of the boundary is only dependent upon temperature and solute content due to which it remains same for all the grain boundaries. As driving force is similar across all grains hence nucleation of recrystallization occurs at similar times. In case of larger grains, total nucleation volume is small compared to initial grain volume, hence in recrystallization volume fraction plot it is barely visible (X (925 µm), **Figure 39**), whereas for smaller grains it becomes visible at early times (X (275 µm), **Figure 39**). Similar is the case for recrystallization growth. The rate of advancement of recrystallization front is given by boundary mobility times driving force which remains almost same across all grains. The apparent difference observed in **Figure 39** is due to the fact that in case of larger grains (925µm) the recrystallization front needs to cover more distance (925/2 µm) whereas for smaller grains (275 µm) the front needs to cover much smaller distance (275/2 µm). Due to this even when recrystallization is over in smaller grains it is still going on in larger grains. **Figure 40** shows the rate of advancement of recrystallization front for the largest and smallest grains and as expected the plot for the two grains (925 and 275 µm) are almost identical.

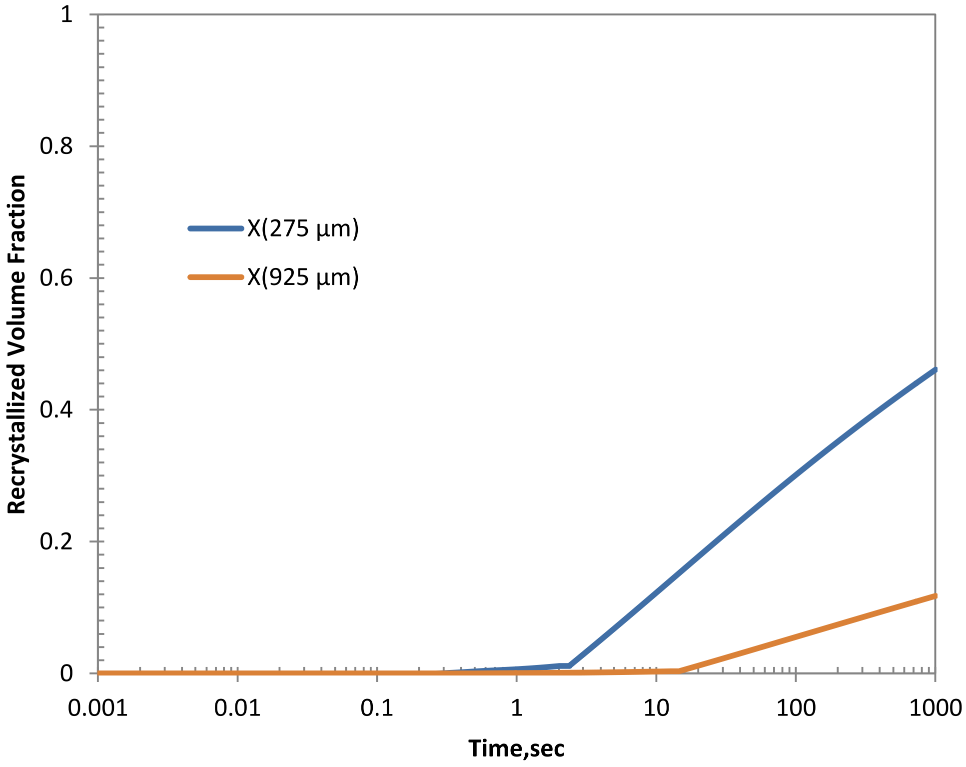

Figure 39: Recrystallized volume fraction evolution for the largest and smallest grains in the distribution. The plot for intermediate sizes lies between the two curves.

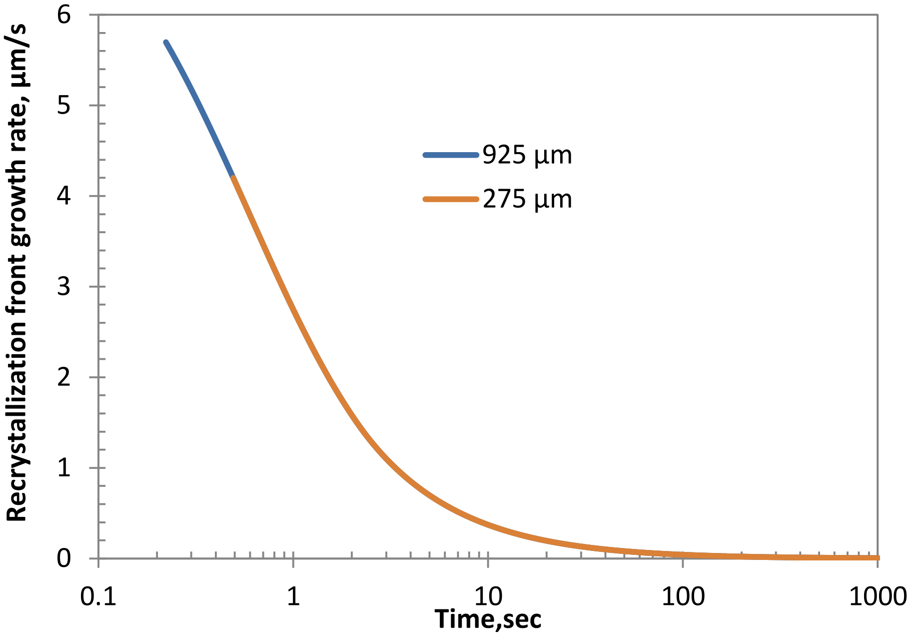

Figure 40: Plot of rate of advancement of recrystallization front for the largest and smallest grains in the distribution.

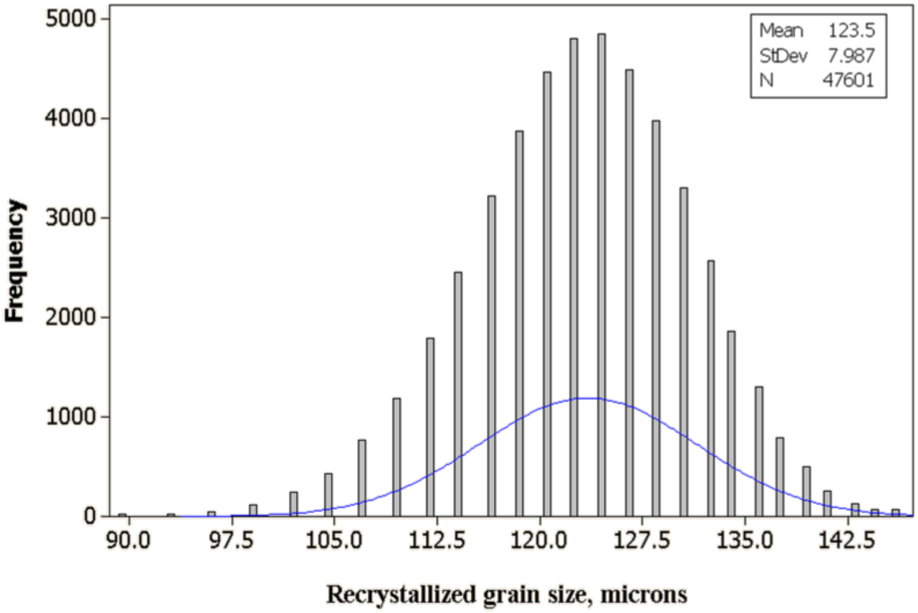

Figure 41: Recrystallized grain size distribution. Comparing with starting size distribution (**Figure 35**), both the mean and standard deviation has reduced considerably.

The key advantage of this approach is the ease with which the next pass deformation can be incorporated into it. The next pass deformation only updates the state parameters (dislocation density, strain, strain rate etc) to the existing values of the ensemble. The key disadvantage of this method is high computation time. The mean field approach described earlier takes only 1-2 seconds to run on a desktop computer whereas the current quasi-mean field model could take anywhere from 1 min to 15 minutes depending on the number of grains and annealing time used in the calculation. Further improvement to this approach can be done using a cellular automaton method. The drawback of the present method is its inability to address spatial in-homogeinity and tracking the neighbours. Spatial in-homogeinity refers to the effect of triple junctions, concave/convex grain boundary, dislocation density difference on two sides of grain boundary, local orientation gradient etc.

4. Discussion/Validation

In the previous chapter a coupled model of recrystallization, recovery, precipitation and grain coarsening was presented. As with any physically based modeling a number of unknown/fitting parameters have been used. Care has been taken to fix all the parameters by fitting the model onto various experimental databases reported in literature. A single set of these parameters could fit all the experimental data is very reassuring.

To further showcase the subtle features of the recrystallization model we have taken a specific case of C-Mn steel at 900 ^{o}C, the overall kinetics of is shown in Figure 42(a), and analyzed the various aspects of the model.

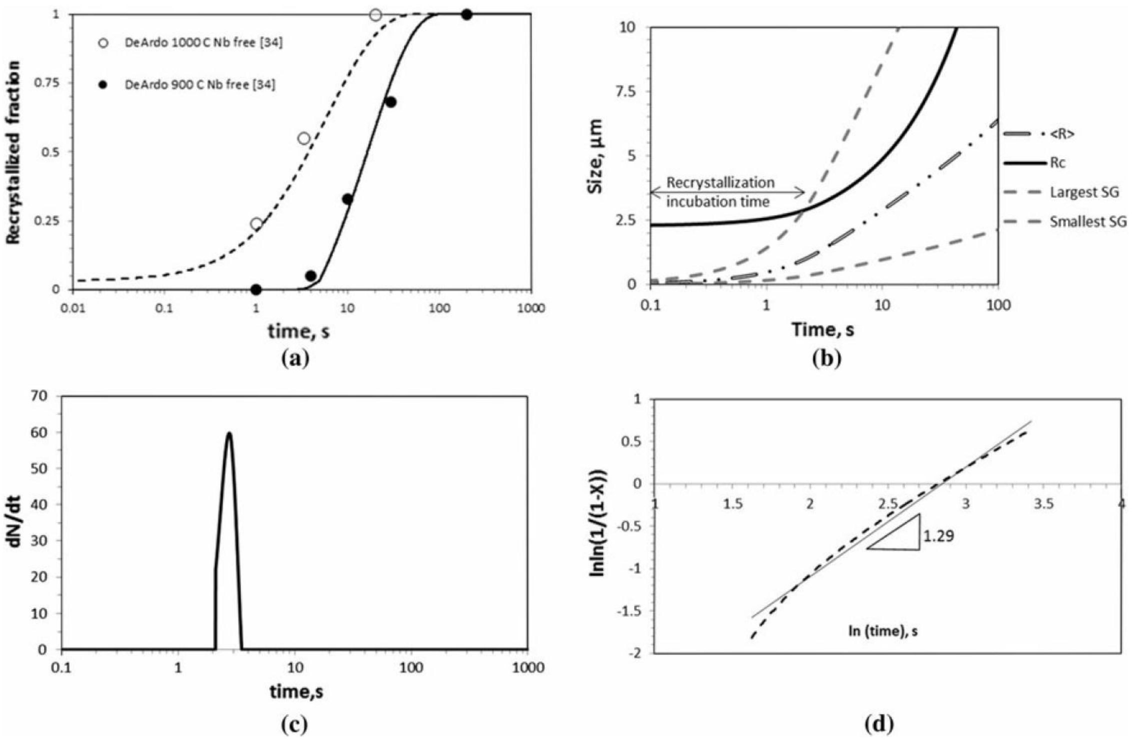

Figure 42: (a) Predicted and experimentally measured recrystallized fraction for steel N1[130] at 1000 ºC and 900 ºC (strain = 0.3, strain rate = 0.1 1/s). Note the effect of temperature on recrystallization kinetics. (b) Plot showing the evolution of sub-grain sizes (largest, mean) and the critical radius for recrystallization nucleation. (c) Plot showing the evolution of nucleation rate. Note that site saturation is quickly achieved leading to nucleation rate dropping down to zero. (d) Plot showing the evolution of Avrami exponent. Note the Avrami exponent changes with the progress of recrystallization.

4.1. Nucleation Module

Figure 42(b), shows the kinetics of subgrain growth. The plot shows the evolution of mean grain size, the maximum grain size and the critical condition for nucleation. The maximum subgrain size is calculated to be three times that of mean at any given time instant as shown in the plot. Nucleation starts when the largest subgrain overcomes the critical condition which in the present case is 3 sec. **Figure 42(c)** shows the nucleation rate (calculated) as a function of time. The initial increase in nucleation rate is due to the fact that with time more and more subgrains overcome the criticality condition barrier due to subgrain growth.

Once nucleation rate reaches to a maximum, it starts decreasing rapidly due to the competition between increased number of sub-grain having the size advantage and the decrease in the available recrystallization nucleation sites at the grain boundary.

Another very important deduction from the modeling is that in the case of static recrystallization the total time for nucleation, i.e total time taken for site saturation condition to achieve is a small fraction of time it takes for recrystallization to be complete. In other words, it means that in the case of static recrystallization nucleation rate is very high and site-saturation occurs quickly. Because of this reason and despite of the assumption of site-saturation taken by lot of researchers they are able to predict recrystallization kinetics with reasonable accuracy. In the present example, total of 25 new grains are formed from one deformed grain. The mean grain size decreased from 200µm to approximately 70µm at the end of recrystallization.

4.2. Avrami plot

For recrystallization growth analysis JMAK plot for this case has been plotted in **Figure 42(d)**. From the figure it is evident that the growth exponent continuously changes throughout the recrystallization evolution; the value of which depends upon the nucleation rate, driving force and growth dimensionality. An effective Avrami exponent of 1.3 has been extracted from the plot. Ideally the Avrami exponent should be 2 when site-saturation assumption and recrystallization growth is assumed to originate from the outer shell and grows inwards. The actual exponent is however lower due to the fact that nucleation is non-random, site-saturation assumption has not been made and the driving force is non-constant and decreases continuously due to recovery. Experimentally for the case of low carbon steels Avrami exponent has been found to be between 1 and 2. The reproduction of established trends by the model has developed our confidence in it.

Subsequently we compared the effect of chemistry and processing parameters in recrystallization kinetics.

4.3. The effects of Solute Nb

Figure 8 shows the effect of solute Nb on the recrystallization kinetics. As is evident from the experimental results, Nb delays both the growth kinetics as well as nucleation kinetics. In our modelling both of these effects has been captured.

The effect of solute Nb on increase in incubation time for recrystallization is due to slower subgrain growth (section 3.1.3.1). The solute Nb atoms pins the extrinsic dislocations, thereby slowing the subgrain growth.

The effect of solute Nb on recrystallization growth is due to reduced grain boundary mobility from solute drag effect[29]. This is captured using Cahn's model of solute drag through Eq. 87.

If one looks into activation volume equation (Eq. 50) in recovery module (Eq. 90), one will notice that addition of solute Nb slows down recovery kinetics which will lead to increase in recrystallization driving force and consequently increased recrystallization kinetics. However this effect is weaker compared to solute drag effect due to which the net result is slower recrystallization kinetics in presence of solute Nb.

From the experimental data base (**Figure 27**), it is worth pointing out that addition of 0.04 wt% Nb lead to decrease in $t_{50\%}$ recrystallization by an order of magnitude.

4.4. Effect of grain size

In steel processing recrystallization is the only mechanism to refine grain size in single phase which has led to lot of effort in the past to understand the kinetics. Effect of starting grain size for complete recrystallization ($t_{95\%}$) was investigated by lot of researchers. Sellars et al. [19] reported that $t_{95\%}$ is proportional to square of initial grain size, as it reflects the available area for recrystallization nucleation [152]. To compare with Sellars model we have generated a similar plot under the same conditions as used by Sellars as shown in **Figure 43** .

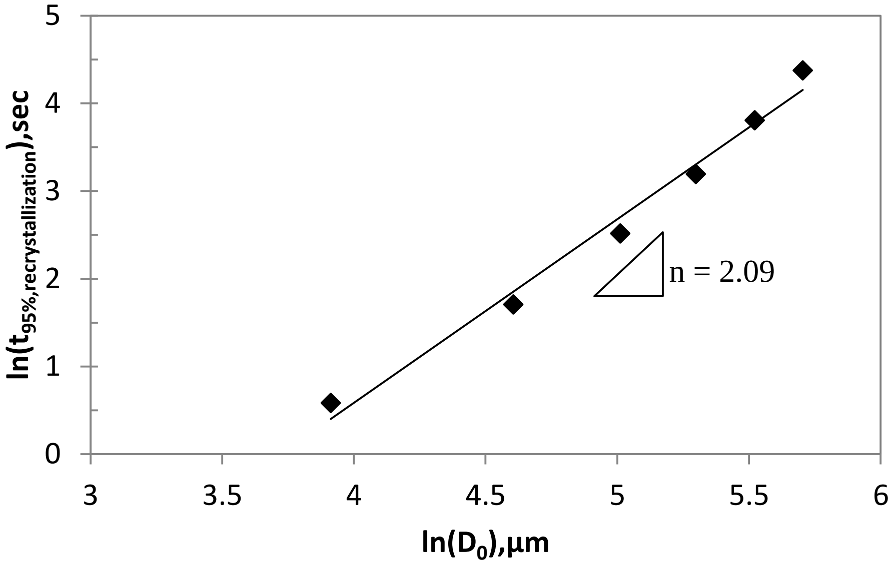

Figure 43: Plot showing the dependence of time for 95 pct recrystallization on initial grain size.

From the plot (**Figure 43**), the initial grain size exponent (2.09) matches well with the validated semi-empirical model of Sellars and other researchers [10, 19].

4.5. Effect of strain

Figure 27 to Figure 42 shows the effect of strain on static recrystallization kinetics. The figures are plotted for strain varying from 0.3 to 0.8. From a preliminary analysis of the experimental database, one may observe that increasing strain leads to increase in recrystallization kinetics. However attempting to make a comparison between the current model with semi-empirical model published in literature does not provide a unique correlation. Applied total strain being not a state variable is the key reason behind this. The relevant parameters which effect microstructure evolution are dislocation density and surface to volume ratio of the deformed grain (Sv factor). The relationship between applied strain and dislocation density is not unique as it is affected by strain rate, strain, grain size, solute content and evolves with time due to recovery. As such it is not possible to develop a unique relationship between the two.

This is also reflected in the fact that different researchers have reported different expressions for recrystallization time ($t_{95\%}$, $t_{50\%}$, $t_{5\%,}$) on strain; including some cases where the exponent were a function of Nb and grain size. Reproducing $t_{5\%}$ as reported by Hodgson et al. [10], wherein the strain exponent is a function of Nb;

$$t_{5\%} = (-5.24 + 550[Nb])10^{-18}\, D_0^2\, \varepsilon^{(-4+77[Nb])} \exp\left(\frac{330{,}000}{RT}\right)$$

Eq. 113

Similarly, Fernandez et al. [11]reported strain exponent to be a function of starting grain size.

$$t_{5\%} = 9.92 * 10^{-11}\, D_0\, \varepsilon^{-5.6 D_0^{-0.15}} \dot{\varepsilon}^{-0.53} exp\left(\frac{180{,}000}{RT}\right) exp\left(\left(\frac{2.75 * 10^5}{T} - 185\right)([Nb] + 0.374[Ti])\right)$$

Eq. 114

We have attempted to make a limited comparison for C-Mn steels for grain size of 200 µm and subjected to strain rate of 10/s. The obtained strain exponent for $t_{95\%}$ recrystallization is -1.6. Using the expressions mentioned above (Eq. 113, Eq. 114) the strain exponent is found to be -1.69 and -2.5 for the case of 0.03 wt % Nb and 200µm grain diameter. The model obtained strain exponent is in reasonable agreement with the values reported in literature.

4.6. Nucleation Parameter (F_N)

The parameter F_N in Eq. 58 in the precipitate nucleation module relates to the total number of precipitates. In the classical nucleation model an Avrami term$\left(1 - {}^{n}/_{n_{total}}\right)$ was used by Zurob et al. [5] to take into account the progressive decay in available nucleation sites. n_{total} is the total number of nucleation sites which is approximated by the following relationship.

$$n_{total} = F_N \, \frac{\rho}{b}$$

Eq. 115

Where ${}^{\rho}/_{b}$ relates to the maximum possible number density of precipitates accommodated in the current strain, F_N is a parameter smaller than unity which relates to minimum distance between precipitates on a dislocation line. The parameter is estimated by fitting the precipitate diameter and number density concurrently. The adjustable parameter F_N varied from 0.0018 at 850 ^{o}C to 0.009 at 1050 ^{o}C. From the values of F_N obtained by fitting the data, it is clear that the recrystallization kinetics is not very sensitive to the F_N values.

4.7. Recrystallized grain size

Nucleation module is an important feature of the present recrystallization model. Knowing the total number of nuclei per deformed grain one could predict the recrystallized grain size.

For the experimental studies to which the model has been validated against i.e. **Figure 27** to Figure 42, the recrystallized grain size was not reported. However looking at the softening curve one would notice that softening is never 100% complete as grain refinement leads to hardening of the microstructure. The current model is able to reproduce these trends accurately.

By comparing the prediction from the current model to the semi-empirical relationship reported in literature additional validation of the present model can be done keeping in consideration the effect of recovery in recrystallization driving force and hence recrystallized grain size. The effect of recovery has not been captured in the semi-empirical work. In widely cited work of Sellars et al. the recrystallized grain size is expressed as a function of initial grain size and total strain;

$$d_{rex} = \frac{1}{2}\frac{d_0^n}{\varepsilon^p} \qquad \text{Eq. 116}$$

Where, $n = 0.67$ and $p = 1$ for the case of C-Mn steel, and $n, p = 0.67$ for the case of microalloyed steel.

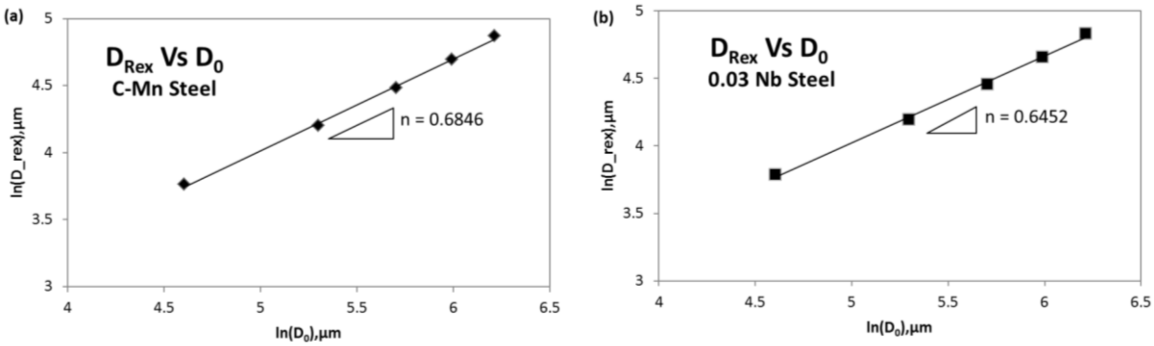

Figure 44: Plot showing the dependence of recrystallized grain size on the initial grain size for (a) C–Mn steel. (b) 0.03 Nb microalloyed steel.

Figure 44 shows the plot of recrystallized grain size as a function of initial grain size for both C-Mn and Nb microalloyed steels. From the plot, the exponent n of Eq. 116 is calculated to be 0.68 for C-Mn steel and 0.64 for Nb microalloyed steels. This is in excellent agreement with Sellars semi-empirical validated model.

Similarly a unique value for p cannot be established, as the number of nuclei formed is also dependent upon recovery kinetics. This leads to p being a function of temperature, strain, Nb as well as Sv factor rather than a unique number. In the work of Perdrix et al.[153] p is expressed as a function of Sv and temperature.

5. Technological Application: Thermo mechanical Processing

The schematic of thermo-mechanical processing is shown in **Figure 1**. The first set of deformations is applied at high temperature, followed by second set of deformation performed at relatively lower temperature. In between the bar is held for certain period of time to drop the temperature below the no recrystallization temperature or recrystallization stop temperature. After the second set of deformation also known as finish rolling the bar is cooled at an accelerated rate. The deformation below RST leads to accumulation of stored energy in the form of dislocation tangles and micro-bands. This increased strain followed by accelerated cooling leads to refinement of transformed microstructure. This refinement of transformed microstructure without the need of separate heat treatment schedule is known as thermo-mechanical processing of steels. In this processing scenario a small amount of alloying leads to large increase in strength by precipitation strengthening. Further increase in strength is due to the effect of ultra-fine precipitate in providing grain size control.

The two important variables in thermo mechanical processing are the amount of deformation in rough rolling and finish rolling. Since the initial slab thickness is fixed from the caster mould thickness and final strip thickness is fixed by the customer, one cannot independently partition the percentage deformation in rough and finish rolling. Generally speaking a maximum of 75% deformation in roughing and finishing is preferred, however if the above is not achievable one need to optimize the schedule based on the amount of grain refinement and pancaking achieved, the details of each aspect is discussed in detail subsequently.

Rough Rolling: The metallurgical objective of rough rolling in TMCP is to refine the austenite grain size. In time it became clear that low temperature fracture toughness, HAZ toughness, and other mechanical properties [154-157] relate to austenite grain size control. Since recrystallization is the only mechanism for grain refinement, hence for complete recrystallization rough rolling should be done at high enough temperature where there is no thermodynamic potential for strain induced precipitation of Nb, and where the recrystallization is fast enough to completely refine the coarse as-cast grain size (~1500 µm).

Delay Table: The objective of introducing a delay is to drop the temperature below RST. However this leads to significant coarsening of recrystallized austenite grains, which in the case of C-Mn steels occurs without any hindrance from precipitates. It has been reported [158] that in commercial processing of C-Mn steels, AlN doesn't precipitate during hot rolling. The same is true for V microalloyed steels [144]. In the case of Ti microalloyed steels it has been suggested that either due to their low volume fraction used in commercial alloys or due to their coarse size they have limited effectiveness in pinning grain boundaries [144, 159] as the driving force for grain coarsening is higher for smaller grains than that of larger grains as given by Eq. 41 (see **Figure 45**). For a commercial Nb microalloyed steel, significant precipitation is not expected in the given temperature window (1100 ^{o}C-1000 ^{o}C) [160, 161]. Due to this significant grain coarsening takes place the rate of which is proportional to mobility times driving force. Boundary mobility for grain coarsening is same as that for recrystallization and the driving force is due to curvature.

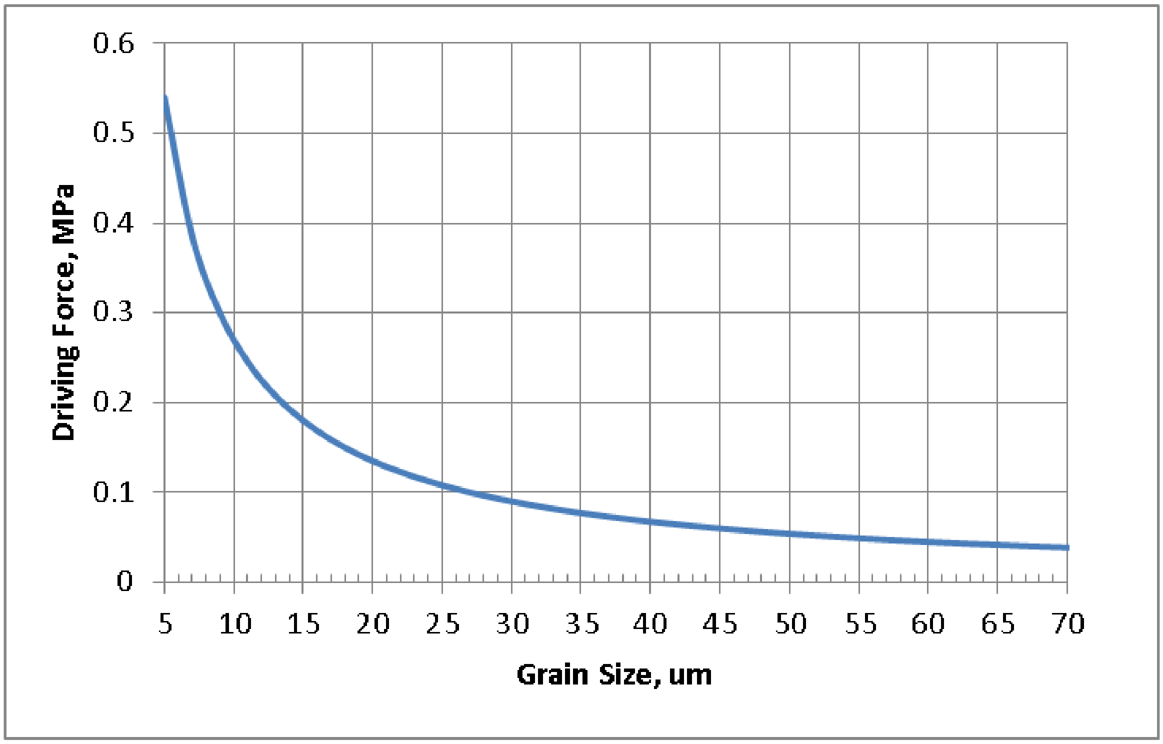

Figure 45: Plot of driving force for grain coarsening as a function of recrystallized grain size.

The grain coarsening rate is given by;

$$D_f = \sqrt{D_i^2 + 16\,\gamma_{gb} M_{gb} (t_f - t_i)} \qquad \text{Eq. 117}$$

This gives isothermal grain coarsening. The effect of temperature enters the above equation through M_{gb} and γ_{gb}. Writing temperature as a function of time one could extend the above equation to non-isothermal cooling as well.

The effect of varying solute Nb, cooling temperature window and cooling rate on non-isothermal grain coarsening kinetics is shown in **Figure 46** using Eq. 117. A starting grain size of 15µm has been considered for the calculation. From the figure one could observe that the effect of lowering the temperature window on grain coarsening is same as that of an increase in solute Nb. Also it is evident from the figure that high solute Nb coupled with low temperature window and high cooling rate gives maximum reduction in coarsening kinetics.

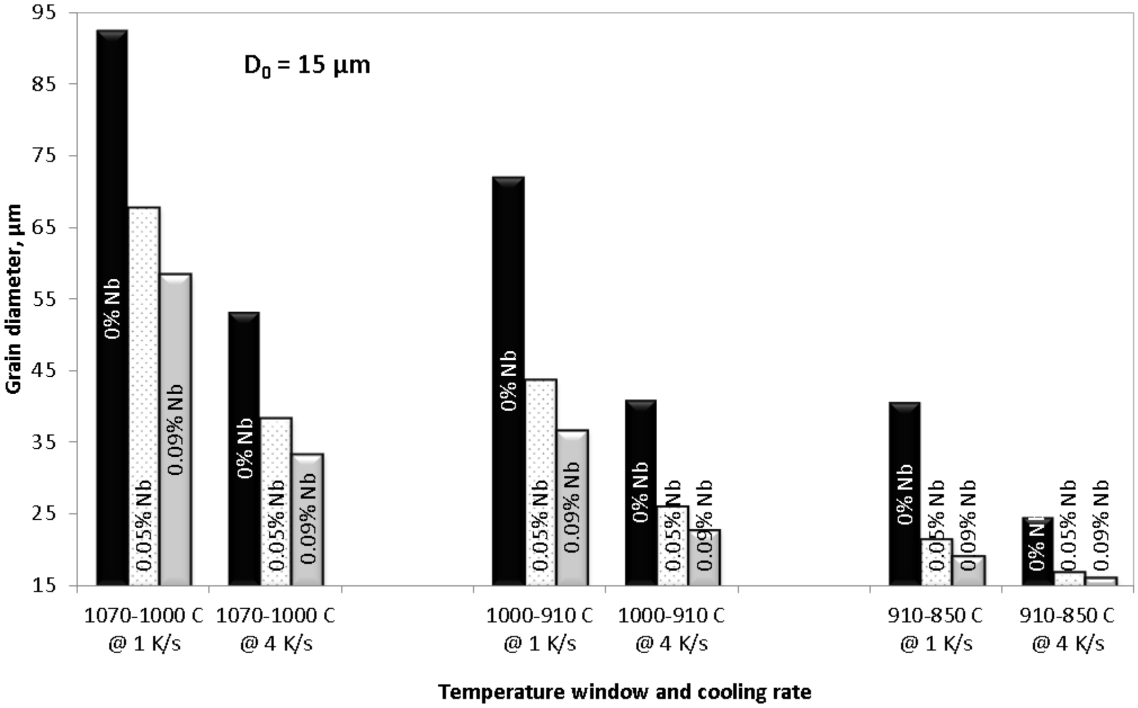

Figure 46: Effect of cooling rate, temperature window and solute Nb on grain coarsening kinetics.

In a typical rolling mill setup one cannot independently decrease the finishing mill entry temperature or increase cooling rate, without increasing delay time, as only ambient air cooling is used in most of the rolling mill.

We are proposing use of a water based accelerated cooling system on delay table at the exit of roughing mill. The schematic of this system is shown in **Figure 47**. To keep the engineering design simple, slight modification of existing laminar headers which are used after finish rolling will be sufficient for this purpose.

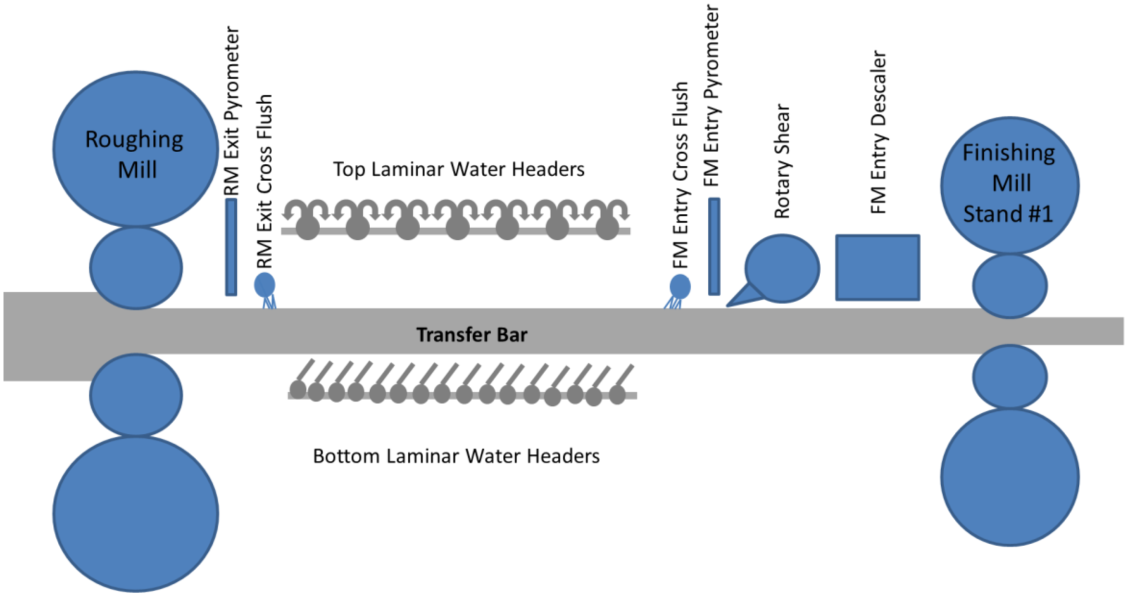

Figure 47: Schematic of proposed accelerated cooling system between rough and finish rolling to minimize grain coarsening and independently target finishing mill entry temperature.

Finish Rolling: From TMCP (**Figure 1**) the objective of finish rolling is to accumulate strain. This is achieved by rolling below RST (recrystallization stop temperature). RST can be achieved by allowing carbo-nitride precipitation to come out at higher temperatures by increasing the interstitial level. This leads to an increase in precipitate volume fraction which prevents recrystallization. This is not a preferred route as the precipitate which comes out at higher temperature exhibits enhanced coarsening due to increased diffusion rates leading to a reduced number density of large size particles. These hard and large particles act as crack nucleation sites during deformation leading to poor fracture toughness, hence should be completely avoided.

The other mechanism to stop recrystallization is to slow down boundary mobility by reducing the bar temperature as it is temperature dependent (Eq. 86). By preventing precipitation to take place in austenite at higher temperature one can conserve the solute to precipitate out during transformation. This can be achieved by lowering the interstitial content. The advantage of this methodology is that Nb being in solution will be able to (i) further slow boundary mobility by its solute drag effect, (ii) promote transformation hardening by promoting diffusionless products such as acicular/banitic ferrite, (iii) enhanced strengthening by inter-phase precipitation leading to nano-scale precipitates.

Advanced line-pipe steels based upon high Nb low interstitial design wherein low temperature fracture properties are essential exploit these concepts. Stress relaxation studies have shown that the precipitation is not significant enough to arrest softening (see **Figure 48**). However older alloy designs based upon high interstitial content can arrest the softening kinetics. A RPTT plot for 0.066 Nb steel containing 0.29 C and 62 ppm N is shown in **Figure 49**. Another important feature to observe is the incubation time for precipitation. In **Figure 49** precipitation starts around 10 sec and finishes at close to 50 sec. In modern high productivity tandem strip mills the total time for finish rolling is 10-15 sec in 5-7 passes with per pass deformation 15-20% and inter-pass time decreasing from 4 to 0.5 seconds in finish rolling hence significant volume fraction of static precipitation is not expected.

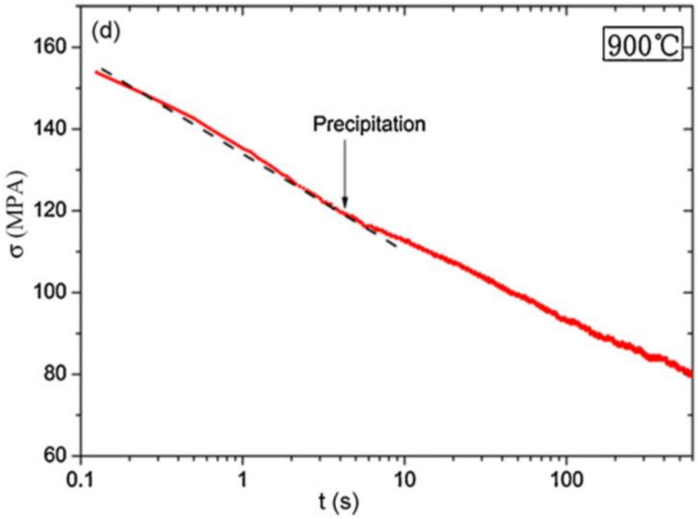

Figure 48: Stress relaxation plot of 0.1 Nb steel containing 0.04C and N≤40ppm deformed to 18% at 900^{o}C [122]

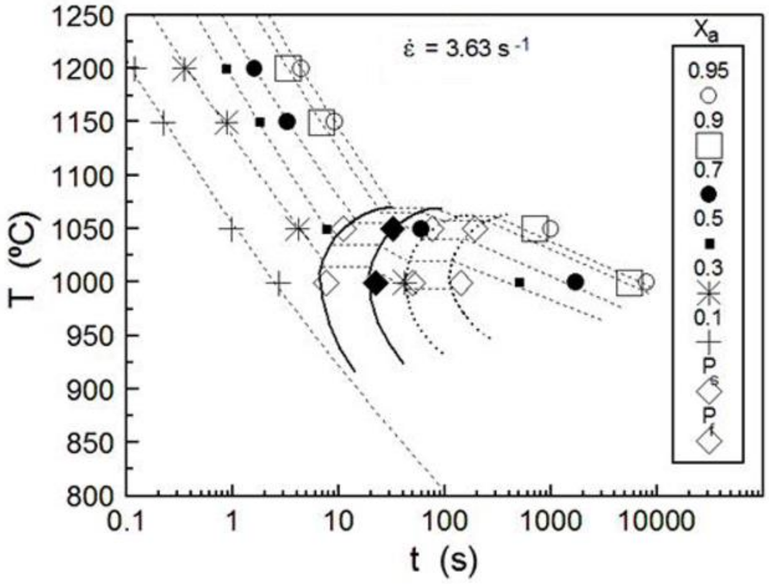

Figure 49: RPTT plot for 0.066 Nb steel containing 0.29C and 62ppm N deformed to 26.5% [161]

Rolling below RST during finish rolling leads to marked changes in microstructure viz. (i) Geometric effect and (ii) Strain accumulation.

(i) **Geometric effect:** Rolling below RST leads to elongation of equiaxed grain. Since transformation nucleates from boundary these elongated grains provide increased nucleation sites, leading to finer transformed products. This is quantified by the parameter (S_V) surface to volume ratio. It can be expressed by the equation of Yoshie et al. [162].

$$S_V = \left(\frac{24}{\pi D_i}\right)(0.491\, e^{\varepsilon} + 0.155\, e^{-\varepsilon} + 0.143\, e^{-3\varepsilon}) \qquad \text{Eq. } 118$$

(ii) **Strain accumulation:** This relates to the increase in dislocation density due to deformation below RST which is analogous to cold rolling. This is carried out mostly during finish rolling of hot rolling process. Here the temperature is relatively lower compared to rough rolling along with presence of strain induced precipitation recovery kinetics is minimized. This leads to rapid build-up of dislocations. The increased accumulated strain increases driving force for austenite to ferrite transformation at a higher rate leading to finer ferrite grain size. Sellers and Banyon[128], Gladman[4], Kozazu[2] and others have demonstrated that for any given S_V, increase in accumulated strain is accompanied by increase grain refinement (**Figure 50**).

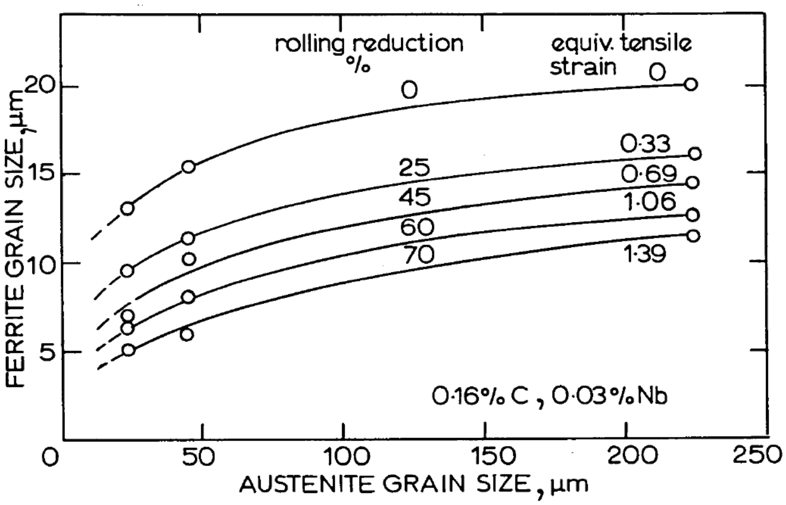

Figure 50: Dependence of ferrite grain size on austenitic grain size and retained strain in Nb-steel plate [2].

5.1. Comparison

In this section with the help of microstructure modeling developed earlier. We will try to analyze microstructure evolution of a typical case (S1) and compare it with a proposed schedule with reduced alloying content (S2). Chemistry of S1 and S2 are mentioned in **Table 4** and their rolling schedules are tabulated in **Table 5**.

Steel	C, wt%	Mn,wt %	Nb, wt%	N, ppm
S1	0.06	1.57	0.06	60
S2	0.05	1.57	0.03	60

Table 4: Alloy chemistries for the two steel samples S1 and S2. For steel S2 interstitial control is preferred.

Sample-S1

Stand	Thk,mm	%redn	Temp,C	Time,s
RME	210			
R1	188.8	10.1	1180	0
R2	158.6	16.0	1165	16.4
R3	126.6	20.2	1140	31.1
R4	98.5	22.2	1125	46.4
R5	77.4	21.4	1110	60
R6	57.7	25.5	1095	78.3
R7	41.8	27.6	1080	97.7
F1	23.4	44.0	1014	177.7
F2	17.1	27.1	994	182.1
F3	13.5	20.7	965	185.4
F4	11.8	12.8	941	187.8
F5	10.2	13.4	922	189.9
F6	9.3	8.7	902	191.8

Sample-S2

Stand	Thk,mm	%redn	Temp,C	Time,s
RME	210			
R1	157	25	1180	0
R2	117	25	1140	16.4
R3	93	21	1110	31.1
R4	75	19	1090	46.4
R5	58	23	1060	60
R6	43	26	1030	78.3
R7	30	30	1000	97.7
F1	21	30	910	177
F2	17	19	895	182
F3	14	16	870	185
F4	12	16	860	188
F5	11	8	850	190
F6	10	9	840	192

Table 5: Hypothetical rolling schedule for the two cases of S1 and S2. The rolling schedule is of conventional hot strip mill.

Figure 51 shows the austenite grain size evolution during rough rolling due to static recrystallization. The temperature window of rough rolling is selected so as not to have any strain induced precipitation of Nb(C,N) which otherwise will interfere with the recrystallization process. The grain size evolution is dependent on strain as temperature is sufficiently high. The rough rolling schedule of S2 has higher strain leading to more grain size refinement as shown in **Figure 51**(b). The high strain is also expected to improve strain penetration.

Once recrystallization is over, fine recrystallized grains tend to coarsen. For low C systems in the temperature window (900-1100 ^{o}C) and the absence of strain, strain induced precipitation is not able to pin the grains which leads to grain coarsening.

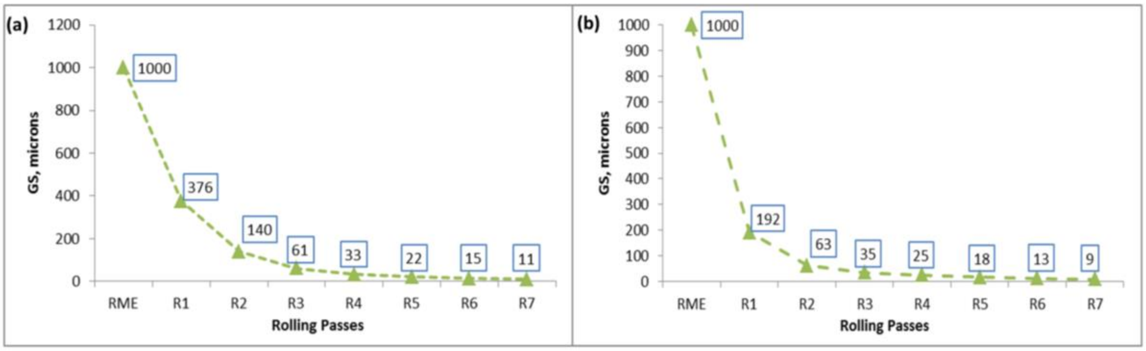

Figure 51: Grain refinement by static recrystallization during rough rolling. (a) For steel S1 and (b) for steel S2.

Due to high temperature and sufficient long time (~60s) at the delay table significant grain coarsening takes place.

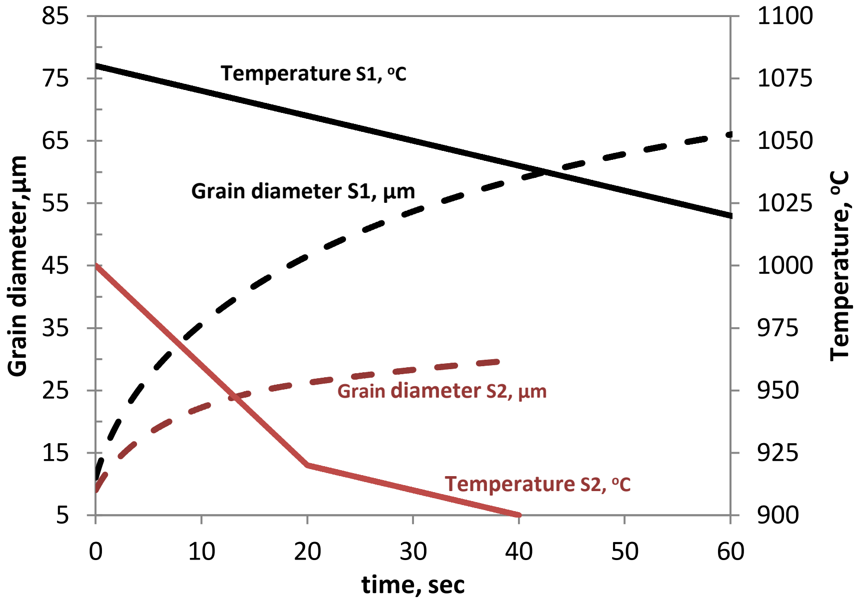

Figure 52: Plot showing the grain coarsening for steel S1 and S2. S2 is cooled initially at an accelerated rate of 4K/sec.

To minimize grain coarsening, lowering the temperature window at delay table is preferred. However care has to be taken that RM exit temperature should not be such to cause incomplete grain refinement. Accelerate cooling using water, air mist or compressed air is preferable as it will rapidly cool through the high mobility temperature window. As shown in **Figure 52** a combination of accelerated cooling less total time has drastically reduced the grain coarsening of sample s2. Increasing solute Nb is beneficial due to its solute drag effect, but it necessarily imposes an upper limit on allowable C and N content which usually is a challenge.

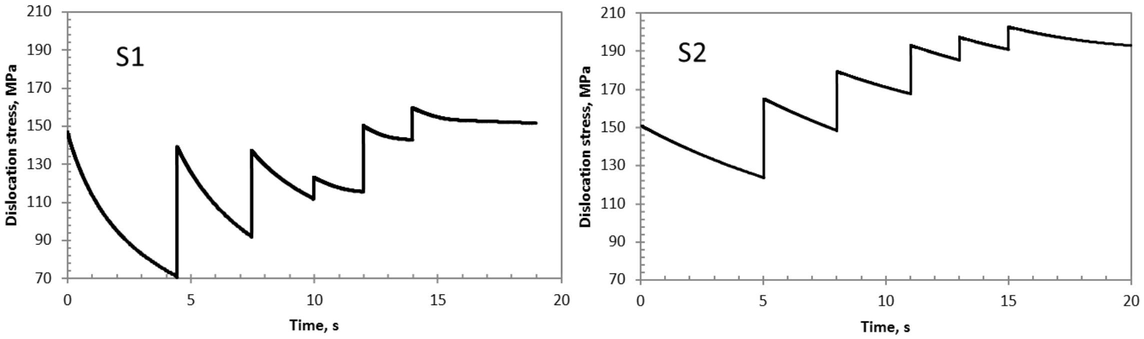

Figure 53: Plot showing the accumulation of plastic stress as a function of time for steel S1 and S2. Zero time corresponds to start of finish rolling.

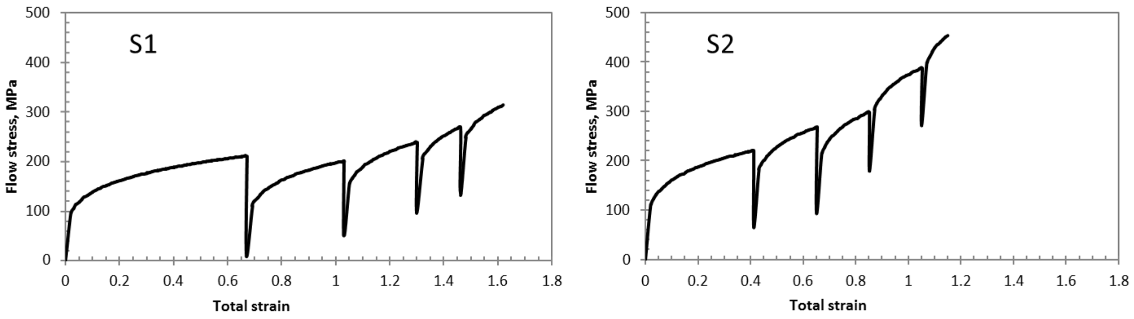

Figure 54: Plot showing the evolution of stress as a function of strain for steel S1 and S2. The plot is for finish rolling.

From thermo-mechanical rolling perspective, the objective of finish rolling is to accumulate strain and increase S_V factor.

Figure 53 and

Figure 54 show the accumulation of stress as a function of time and strain for both steel S1 and S2. The plot shows considerable inter-pass softening in case of S1. This is due to increased recovery kinetics because of high temperature.

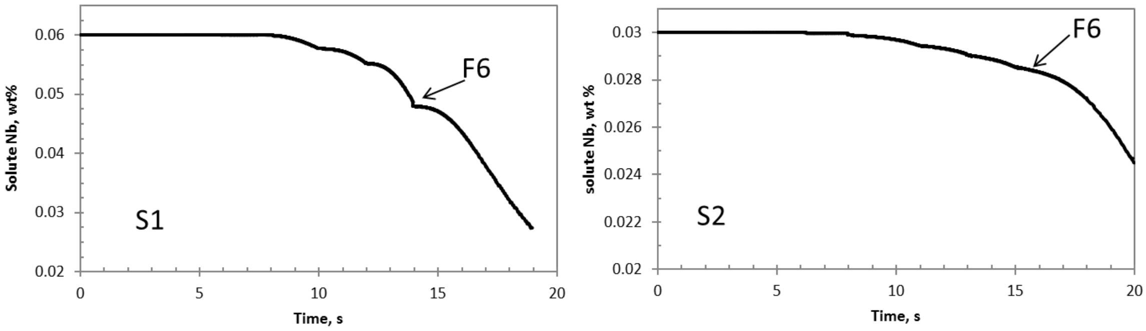

Figure 55: Solute Nb evolution as a function of finish rolling time for alloy S1 and S2. Irrespective of the initial solute Nb content maximum precipitation occurs between F6 exit and laminar cooling.

Figure 55 shows the amount of Nb remaining in solution in finished rolling. Due to low inter-pass time static precipitation of Nb during rolling is very low. However during the time when the bar leaves the last rolling stand and hits accelerated cooling, maximum strain induced precipitation takes place. This is due to the fact that during this time, the accumulated strain is maximum and temperature is minimum resulting in enhanced driving force for precipitation. For steel S2 the amount of Nb precipitated out is less because of low supersaturation. Increased solute Nb in finished rolling is preferred as it leads to transformation hardening and interface precipitation contributing to the strength and ductility.

S_v factor relates to the geometric measure of pancaking and has been related to the transformed ferrite grain size (see **Figure 50**). As shown previously that Sv depends both on starting austenite grain size and percentage reduction below RST, the implication of which is shown in **Figure 56**. The prior austenite grain size of S2 being smaller leads to a higher final S_v than S1 although the total deformation given in finish rolling is higher in S2 than in S1.

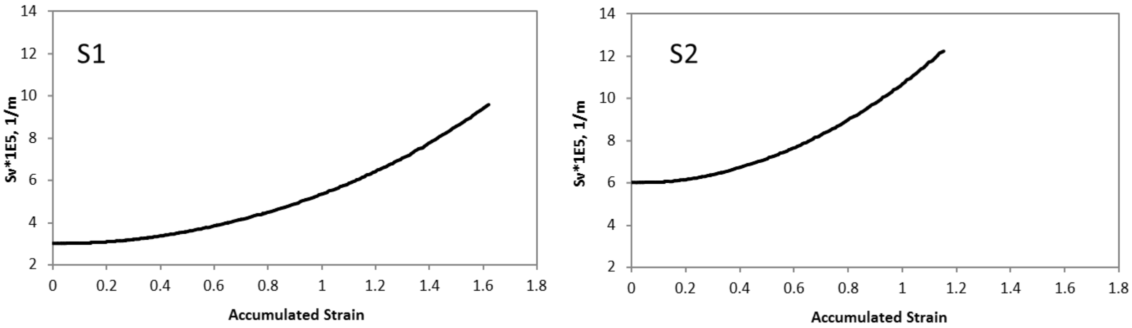

Figure 56: Evolution of S_V as a funtion of applied strain in finish rolling using Eq. 118. Smaller austenite grains in S2 leads to increase in S_V even with low total strain.

Summary: Room temperature mechanical properties have been correlated with transformed grain size and inter-phase precipitation volume fraction and low temperature fracture properties have been correlated with austenite grain size[4].

Figure 53 and

Figure 54 show increased amount of accumulated strain, solute Nb for S2 which will give increased strength after transformation for the same cooling rate. Whereas **Figure 52** and **Figure 56** shows that final prior austenite grain size for S2 is much smaller compared to S1. This will give better resistance to ductile fracture and increased low temperature brittle fracture resistance. Hence the rolling schedule of S2 is better than S1.

5.2. Strategies for TMC processing of thicker gauges

Processing of thicker gauges of steel presents an additional challenge for microstructure control. Due to the market focus on thicker gauge, higher strength steels, metallurgists are presented with an additional challenge. Slab thickness being fixed limits the total reduction possible when compared to thinner gauge. The deterioration in mechanical properties is due to insufficient grain refinement in rough rolling and low strain accumulation, along with inadequate pancaking in finish rolling, as a rule of thumb, a minimum of 75% reduction in roughing and finishing is necessary. In what follows we have tried to come up with various strategies to overcome the above mentioned constraints.

Geometrical Effects of Pancaking: Rolling below RST leads to elongation of austentite grains, thereby increasing the grain boundary area and flattening of the austenite grains, S_v as a function of starting grain size and rolling reduction is shown in **Figure 57**. It can be expressed by Eq. 118. Control of upstream grain size is one possible way to substitute for deformation. Point A corresponds to S_V of 80 obtained by rolling 60% below RST on a grain size of 45μm. The same S_V can be obtained by rolling 30% on a grain size of 30 µm. This means if one is able to enter Finishing Mill with smaller grain size one can achieve the same S_V with less total reduction.

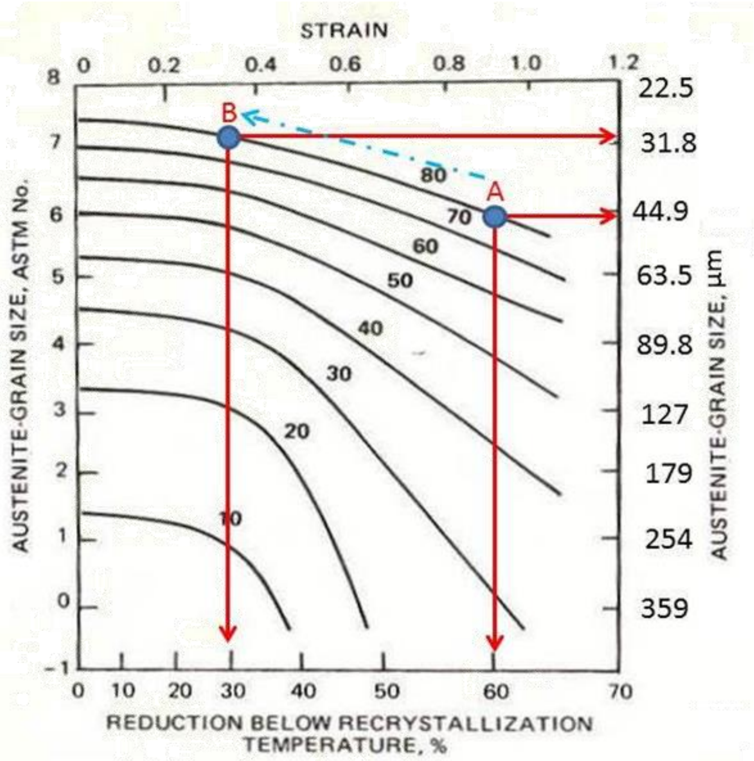

Figure 57: Plot of SV as a function of initial austenite grain size and percentage reduction below RST. After Kozasu et al. [2]

Strain Accumulation: As explained earlier rolling below RST leads to increase in dislocation density. Lowering the temperature window for finish rolling leads to increase in strain accumulation due to suppression of recovery. However the rolling schedule designers are not comfortable in rolling at low temperatures, due to expected increase in work hardening and hence mill forces. From **Eq. A119** (Appendix 1) it is clear that for thicker gauges where total reduction in finishing mill is low, reducing finishing mill entry temperature to below 850 °C will not cause any substantial increase in mill forces. This is due to the effect of thickness reduction in total reduction is more dominant on mill forces than the increase in flow stress. Keeping all other parameters constant, increasing strain accumulation by rolling at lower temperature window is expected to improve the low temperature fracture properties.

Recrystallized assisted Rolling (RAR):

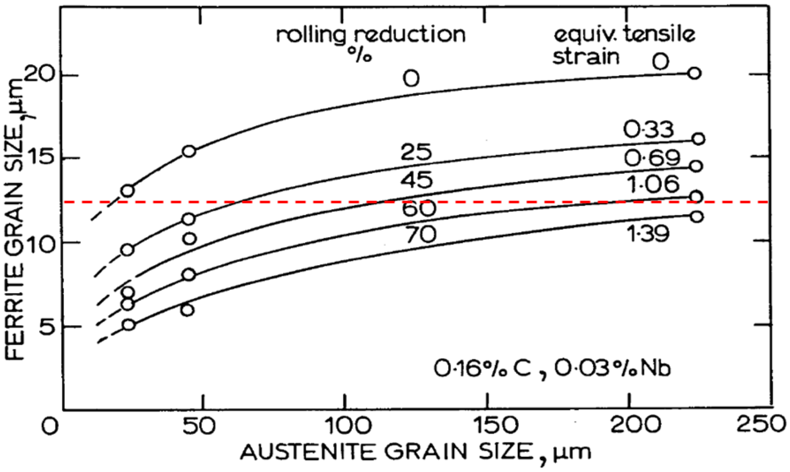

Figure 58: Dependence of ferrite grain size on austenitic grain size and retained strain in Nb-steel plate [2]

For design of rolling schedule in case of industrial processing, an additional constraint of high rolling loads are usually encountered. This has prevented underpowered mills to produce grades based upon severe thermo-mechanical controlled processing [163]. In what follows, we tried to come up with an alternative rolling design to reduce high rolling load associated with severe TMCP practice and thinner gages of steel.

In the case of industrial rolling of steels the starting slab thickness is usually fixed and the final strip thickness is variable. The usual rolling practice suffers from high rolling load in case of low strip thickness as the total deformation given becomes high and low strain accumulation while rolling thicker gages as the total deformation is low. In the traditional practice, finish rolling is done below RST so as to accumulate strain. In RaR, instead of rolling below RST it is proposed to roll above RLT at a substantial higher temperature preferably greater than 1050 ^{o}C. This will lead to grain refinement of austenite instead of strain accumulation. For a given transformation cooling rate the transformed ferrite grain size depends upon accumulated strain and austenite grain size [128]. From **Figure 58**, to produce 12 µm ferrite grains, either a 60% reduction on a 200 µm grain, 45% reduction on a 130 µm grain, a 25% reduction on 60 µm grain or a 0% reduction on a 20 µm grain is needed. This allows one to obtain similar mechanical properties by promoting grain refinement. In thicker gage steel where due to current thickness restrictions insufficient strain accumulation occurs one could aim for grain refinement instead. To promote grain refinement one could aim for higher finishing temperatures. This has a beneficial effect on reducing rolling loads while rolling thinner gages, as the decrease in flow stress due to increase in temperature is much more prominent than the increase in yield stress due to grain refinement. Keeping the flow stress low allows for low rolling load[164]. This strategy could be exploited in cases when either high rolling load or insufficient pancaking of the microstructure is the main problem.

6. Conclusion

In the present contribution, a physically based model of static recrystallization of microalloyed austenite has been developed. The model predictions are in agreement with semi-empirical models for the recrystallization time and grain size and experimentally reported recrystallization kinetics as a function of processing parameters. The key features of the model are as follows:

1. Detailed description of the nucleation process is available, thereby eliminating the need to employ the assumptions of site saturation or constant nucleation rate which is present in most of the recrystallization models.
2. Model captures the effect of recovery and precipitation on both nucleation and growth of recrystallization.
3. Model incorporates the effect of solute Nb on recovery as well as the nucleation and growth stages of recrystallization. This makes it quite suitable for describing the roughing operation of hot strip and plate mill as repeated recrystallization without significant precipitation happens there.
4. Coarsening of recrystallized grains has also been modeled and has been found to be in agreement with experimental database reported in literature. This model can be used to predict coarsening kinetics at delay table of hot strip mill.
5. A special case wherein recrystallization takes place at an extremely slow rate when global zener drag force is higher than the driving force for recrystallization has been described. This is found to be when particle coarsening at grain boundary is controlling the recrystallization growth.

6. Since the effect of precipitation on both recrystallization and recovery kinetics has been considered, it allows calculation of strain accumulation during finish rolling operation of Hot Strip and Plate Mill.
7. The model takes into account recovery, recrystallization and precipitation, thereby allowing accurate calculation of the softening fraction. This has been used to predict Rolling Mill Forces.
8. The model has been used to analyze industrial rolling schedules and using the modeling output a hypothetical rolling schedule has been proposed as well.
9. Based upon various influential parameters of specific metallurgical process as identified by the model, new rolling strategy has been proposed as well to promote grain refinement, when high deformation is not possible in thicker gages of steels.

7. Future Work

Current version of the developed model has been able to predict experimental observations in a wide range of chemistry and processing conditions making them quite suitable to investigate industrial rolling schedule, there still exists some limitations/unknowns which are worth to be addressed in future versions. Some of the possible areas in which the model can be further refined are listed below:

1. A correct expression of mobility of high angle boundary is essential to have a good predictive capability for recrystallization and grain coarsening. In present case we have incorporated the role of Nb. However commercial alloys also contain Mn and Mo which are expected to give significant solute drag to boundary mobility. This should be addressed in future version of the model.

2. The present model considers strain induced precipitation of Nb. In commercial alloys Nb is usually used in conjunction with Ti. It has been shown that Nb can precipitate epitaxially on pre-existing TiN particles [165]. This will give incorrect calculation for microstructure evolution as epitaxial nucleation and growth will raise RST. This is not considered in present model.

3. Recrystallized grain size depends upon the nucleation kinetics. Since nucleation kinetics is difficult to observe directly one may back calculate it from recrystallized grain size. There is no complete experimental database reported in the studies which has been referred to, wherein the researchers have looked at recrystallization kinetics along with recrystallized grain size and its coarsening, thereby not allowing the complete validation

of the model. This fundamental database generation is essential to further enhance the model.

4. In the current recrystallization model nucleation is assumed to be SIBM. As explained in text, boundary bulges due to dislocation density difference across the two sides of the boundary. Tracking of dislocation density evolution in neighbouring grains becomes important for a better prediction of recrystallization incubation time. Similarly triple junctions are also potential nucleation sites from recrystallization. Quasi-mean field model takes into consideration the effect of grain size distribution but to incorporate the effect of neighbour either a cellular automaton or phase field based modeling is needed.

5. Our understanding of precipitation evolution in multi-pass deformation is still not complete. The effect of deformation on growth/coarsening of pre-existing precipitates warrant further investigation. It has been remarked that each deformation pass leads to formation of new dislocation network, due to which the solute diffusivity can vary between that of bulk diffusion to pipe diffusion. This will lead to significant difference in time evolution of precipitate number density and its size. Proper design of experiments along with fundamental database generation is required.

6. Our understanding of effect of alloy chemistry and thermo-mechanical processing schedule on mechanical properties such as yield to tensile ratio, DBTT, anisotropy (longitudinal, transverse and 15-50^o) is still not complete which warrants further investigation[166, 167].

8. References

1. Bai, D., M.A. Cooke, J. Asante, and J. Dorricott, 2004, Google Patents.
2. Kozasu, I., C. Ouchi, I. Sampei, and T. Okita. Microalloying '75, Union Carbide, New York, 1977: p. 120.
3. Nie, W.J., W.F. Xin, T.M. Xu, P.J. Shi, and X.B. Zhang. Advanced Materials Research, 2011. **194**: p. 1183-1191.
4. Gladman, T., *The physical metallurgy of microalloyed steels*1997, London: Institute of Materials.
5. Zurob, H.S., C.R. Hutchinson, Y. Brechet, and G. Purdy. Acta Mater, 2002. **50**(Compendex): p. 3075-3092.
6. Andrade, H.L., M.G. Akben, and J.J. Jonas. Metallurgical Transactions A (Physical Metallurgy and Materials Science), 1983. **14A**(10): p. 1967-77.
7. Bai, D., S. Yue, W. Sun, and J. Jonas. Metallurgical and Materials Transactions A, 1993. **24**(10): p. 2151-2159.
8. Cho, S.-H., K.-B. Kang, and J.J. Jonas. Isij Int, 2001. **41**(Compendex): p. 63-69.
9. Hodgson, P.D. Metals forum, 1993. **17**(4): p. 403-408.
10. Hodgson, P.D. and R.K. Gibbs. Isij Int, 1992. **32**(12): p. 1329-1338.
11. Fernandez, A.I., P. Uranga, B. Lopez, and J.M. Rodriguez-Ibabe. Isij Int, 2000. **40**(9): p. 893-901.
12. Humphreys, F.J. and M. Hatherly, *Recrystallization and related annealing phenomena*. 2nd ed2004, Amsterdam ; Boston: Elsevier. xxx, 628 p.
13. Sandsttröm, R. Acta Metall Mater, 1977. **25**(8): p. 905-911.
14. C.M.Sellars. AGARD Conference Proceedings, 1980(Compendex).
15. Dutta, B., E.J. Palmiere, and C.M. Sellars. Acta Mater, 2001. **49**(Compendex): p. 785-794.
16. Dutta, B. and C.M. Sellars. Mater Sci Tech Ser, 1986. **2**(2): p. 146-153.
17. Sellars, C.M. Mater Sci Tech Ser, 1990. **6**(11): p. 1072-1081.
18. Sellars, C.M. *The kinetics of softening processes during hot working of austenite*. in *Proceedings of the 3rd International Symposium on Recent Problems in Plasticity of Metals and Alloys, 10-12 Sept. 1984*. 1985. Czechoslovakia.
19. Sellars, C.M. and J.A. Whiteman. Met Sci, 1979. **13**(3-4): p. 187-194.
20. Zheng, C., N. Xiao, D. Li, and Y. Li. Computational Materials Science, 2008. **44**(2): p. 507-514.
21. Thiessen, R. and I. Richardson. Metallurgical and Materials Transactions B, 2006. **37**(4): p. 655-663.
22. Nes, E. Acta metallurgica et materialia, 1995. **43**(Compendex): p. 2189-2207.
23. Mecking, H. and U.F. Kocks. Acta Metall Mater, 1981. **29**(Copyright 1982, IEE): p. 1865-75.
24. Vervynckt, S., K. Verbeken, P. Thibaux, and Y. Houbaert. Steel Research International, 2010. **81**(Compendex): p. 234-244.
25. Vervynckt, S., K. Verbeken, P. Thibaux, and Y. Houbaert. Steel Research International, 2011. **82**(4): p. 369-378.
26. Homsher, C.N. M.S Thesis, Colorado School of Mines, 2013.
27. McQueen, H. and J. Jonas. Plastic deformation of materials.(A 75-46501 24-26) New York, Academic Press, Inc., 1975, 1975: p. 393-493.

28. Zadeh, A.A. Ph.D Thesis, 1996. **University of Wollongong**.
29. Yamamoto, S., C. Ouchi, and T. Osuka. *EFFECT OF MICROALLOYING ELEMENTS ON THE RECOVERY AND RECRYSTALLIZATION IN DEFORMED AUSTENITE*. in *Thermomechanical Processing of Microalloyed Austenite: Proceedings of the International Conference.* 1982. Pittsburgh, PA, USA: Metallurgical Soc of AIME.
30. Jonas, J.J. and M.G. Akben. Metals Forum 4, 1981: p. 92.
31. McElroy, R.J. and Z.C. Szkopiak. International Metallurgical Reviews, 1972. **17**(Copyright 1972, IEE): p. 175-202.
32. Martinez, L.G., K. Imakuma, and A.F. Padilha. Steel Research, 1992. **63**(Copyright 1992, IEE): p. 221-3.
33. Friedel, J., *Dislocations*. [1st English ed. International series of monographs on solid state physics,1964, Oxford, New York,: Pergamon Press; U.S.A. ed. distributed by Addison-Wesley Pub. Co., Reading. xxi, 491 p.
34. Maruyama, N., R. Uemori, and M. Sugiyama. Materials Science and Engineering: A, 1998. **250**(1): p. 2-7.
35. Li, J.C.M. Can J Phys, 1967. **45**(2): p. 493-509.
36. Prinz, F., A.S. Argon, and W.C. Moffatt. Acta Metall Mater, 1982. **30**(4): p. 821-830.
37. Castro-Fernáandez, F.R. and C.M. Sellars. Philosophical Magazine A, 1989. **60**(4): p. 487-506.
38. Verdier, M., Y. Brechet, and P. Guyot. Acta Mater, 1998. **47**(1): p. 127-134.
39. Hasegawa, T., T. Yakou, and U.F. Kocks. Acta Metall Mater, 1982. **30**(Copyright 1982, IEE): p. 235-43.
40. Sharma, R.C., V.K. Lakshmanan, and J.S. Kirkaldy. Metallurgical Transactions A (Physical Metallurgy and Materials Science), 1984. **15A**(Copyright 1984, IEE): p. 545-53.
41. Fujita, N. and H.K.D.H. Bhadeshia. Mater Sci Tech Ser, 2001. **17**(Copyright 2001, IEE): p. 403-8.
42. Perrard, F., A. Deschamps, and P. Maugis. Acta Mater, 2007. **55**(Compendex): p. 1255-1266.
43. Fratzl, P. and O. Penrose. Physical Review B (Condensed Matter), 1994. **50**(Copyright 1994, IEE): p. 3477-80.
44. Soisson, F., A. Barbu, and G. Martin. Acta Mater, 1996. **44**(Copyright 1996, IEE): p. 3789-800.
45. Clouet, E., M. Nastar, and C. Sigli. Physical Review B (Condensed Matter and Materials Physics), 2004. **69**(Copyright 2004, IEE): p. 64109-1.
46. Kampmann, R., T. Ebel, M. Haese, and R. Wagner. Physica Status Solidi B, 1992. **172**(Copyright 1992, IEE): p. 295-308.
47. Hardouin Duparc, A., C. Moingeon, N. Smetniansky-de-Grande, and A. Barbu. Journal of Nuclear Materials, 2002. **302**(Copyright 2002, IEE): p. 143-55.
48. Christien, F. and A. Barbu. Journal of Nuclear Materials, 2004. **324**(Compendex): p. 90-96.
49. Wagner, R. and R. Kampmann, *Materials science and technology: a comprehensive treatment*. Vol. 5. 1991, Weinheim: Wiley–VCH.
50. Myhr, O.R. and O. Grong. Acta Mater, 2000. **48**(Copyright 2000, IEE): p. 1605-15.
51. Nicolas, M. and A. Deschamps. Acta Mater, 2003. **51**(Copyright 2004, IEE): p. 6077-94.
52. Robson, J.D. Acta Mater, 2004. **52**(Compendex): p. 1409-1421.

53. Balasubramanian, K. and J.S. Kirkaldy. Calphad, 1985. **9**(2): p. 103-115.
54. Sharma, R.C., V.K. Lakshmanan, and J.S. Kirkaldy. Metallurgical transactions. A, Physical metallurgy and materials science, 1984. **15 A**(Compendex): p. 545-553.
55. T.Mori, M.Tokizane, K.Yamaguchi, E. Sumani, and Y.Nakazima. tetsu-to-hagne, 1968. **54**: p. 763.
56. Palmiere, E.J., C.I. Garcia, and A.J. DeArdo. Metallurgical and Materials Transactions A (Physical Metallurgy and Materials Science), 1994. **25A**(Copyright 1994, IEE): p. 277-86.
57. Dutta, B., E.J. Palmiere, and C.M. Sellars. Acta Mater, 2001. **49**(Copyright 2001, IEE): p. 785-94.
58. Perez, M., E. Courtois, D. Acevedo, T. Epicier, and P. Maugis. *Precipitation of niobium carbonitrides: Chemical composition measurements and modeling*. in *5th International Conference on Processing and Manufacturing of Advanced Materials - THERMEC'2006, July 4, 2006 - July 8, 2006*. 2007. Vancouver, Canada: Trans Tech Publications Ltd.
59. Xu, Y.-b., Y.-m. Yu, X.-h. Liu, and G.-d. Wang. J Iron Steel Res Int, 2006. **13**(Copyright 2007, The Institution of Engineering and Technology): p. 53-6.
60. Okaguchi, S. and T. Hashimoto. Isij Int, 1992. **32**(Compendex): p. 283-290.
61. Hillert, M. and L.I. Staffanson. Acta Chemica Scandinavica, 1970. **24**: p. 3618.
62. Maugis, P. and M. Goune. Acta Mater, 2005. **53**(Compendex): p. 3359-3367.
63. Irvine, K., F. Pickering, and T. Gladman. IRON STEEL INST J, 1967. **205**(2): p. 161-182.
64. Koyama, S., T. Ishii, and K. Narita. Journal of the Japan Institute of Metals, 1971. **35**(Copyright 1972, IEE): p. 1089-94.
65. Hansen, S.S., J.B. Vander Sande, and M. Cohen. Metallurgical transactions. A, Physical metallurgy and materials science, 1980. **11 A**(3): p. 387-402.
66. Dutta, B. and C.M. Sellars. Mater Sci Tech Ser, 1987. **3**(Copyright 1987, IEE): p. 197-206.
67. Liu, W.J. and J.J. Jonas. Metallurgical Transactions A (Physical Metallurgy and Materials Science), 1988. **19A**(Copyright 1988, IEE): p. 1415-24.
68. Liu, W.J. and J.J. Jonas. Metallurgical transactions. A, Physical metallurgy and materials science, 1989. **20 A**(Compendex): p. 689-697.
69. Park, S.H., S. Yue, and J.J. Jonas. Metallurgical transactions. A, Physical metallurgy and materials science, 1992. **23 A**(Compendex): p. 1641-1651.
70. Hua, M., A.J. DeArdo, C.I. Garcia, V. Thillou, and C. Perdrix. *Precipitation of NbC and effect of Mn on the strength properties of hot strip HSLA low carbon steel*. in *Materials Science Forum*. 1998. Trans Tech Publ.
71. DeArdo, A.J., J.M. Gray, and L. Meyer. *FUNDAMENTAL METALLURGY OF NIOBIUM IN STEEL*. in *Niobium, Proceedings of the International Symposium.* 1984. San Francisco, CA, USA: Metallurgical Soc of AIME.
72. Cohen, M. and S.S. Hansen. ASTM Special Technical Publication, 1979(Compendex): p. 34-52.
73. Chilton, J.M. and M.J. Roberts. Metallurgical transactions. A, Physical metallurgy and materials science, 1980. **11 A**(Compendex): p. 1711-1721.
74. Jones, A.R., P.R. Howell, and B. Ralph. J Mater Sci, 1976. **11**(9): p. 1593-1599.
75. Jones, A.R., P.R. Howell, and B. Ralph. J Mater Sci, 1976. **11**(9): p. 1600-1606.
76. Cottrell, A.H. and B.A. Bilby. Proceedings of the Physical Society. Section A, 1949. **62**(1): p. 49.
77. Ham, F.S. J Appl Phys, 1959. **30**(6): p. 915-926.

78. Vodopivec, F. and L. Kosec. Metall, 1974. **28**(Compendex): p. 572-574.
79. Jonas, J.J. and I. Weiss. *Effect of precipitation on recrystallization in microalloyed steels*. in *Proceedings of Conference on Recrystallization in the Development of Microstructure, 4-6 April 1978*. 1979. UK.
80. Deschamps, A. and Y. Brechet. Acta Mater, 1998. **47**(1): p. 293-305.
81. Rios, P.R., F. Siciliano Jr, H.R.Z. Sandim, R.L. Plaut, and A.F. Padilha. Materials Research, 2005. **8**: p. 225-238.
82. Doherty, R.D., D.A. Hughes, F.J. Humphreys, J.J. Jonas, D.J. Jensen, M.E. Kassner, W.E. King, T.R. McNelley, H.J. McQueen, and A.D. Rollett. Materials Science & Engineering A (Structural Materials: Properties, Microstructure and Processing), 1997. **A238**(Copyright 1998, FIZ Karlsruhe): p. 219-74.
83. Burke, J.E. and D. Turnbull. Progress in Metal Physics, 1952. **3**(0): p. 220-292.
84. Hurley, P.J. and F.J. Humphreys. Acta Mater, 2003. **51**(Compendex): p. 3779-3793.
85. Zurob, H.S., Y. Brechet, and J. Dunlop. Acta Mater, 2006. **54**: p. 3983-3990.
86. Beck, P.A., P.R. Sperry, and H. Hu. J Appl Phys, 1950. **21**(5): p. 420-425.
87. Beck, P.A. and P.R. Sperry. J Appl Phys, 1950. **21**(2): p. 150-152.
88. Bailey, J.E. Philosophical Magazine, 1960. **5**(56): p. 833-842.
89. Humphreys, F.J. *Nucleation in recrystallization*. in *Second Joint International Conference on Recrystallization and Grain Growth, ReX & GG2, SF2M, 30 Aug.-3 Sept. 2004*. 2004. Switzerland: Trans Tech Publications.
90. Bate, P. and B. Hutchinson. Scripta Mater, 1997. **36**(Compendex): p. 195-198.
91. Lauridsen, E.M., H.F. Poulsen, S.F. Nielsen, and D. Juul Jensen. Acta Mater, 2003. **51**(Copyright 2003, IEE): p. 4423-35.
92. Turnbull, D. Trans AIME, 1951. **191**: p. 661.
93. Speer, J.G. and S.S. Hansen. Metallurgical transactions. A, Physical metallurgy and materials science, 1989. **20 A**(Compendex): p. 25-38.
94. Cuddy, L. The Metallurgical Society/AIME, 1982: p. 129-140.
95. Cahn, J.W. Acta Metall Mater, 1956. **4**(5): p. 449-459.
96. Lucke, K. and H.P. Stuwe. Acta Metall Mater, 1971. **19**(Copyright 1971, IEE): p. 1087-99.
97. Hillert, M. and B. Sundman. Acta Metall Mater, 1976. **24**(Copyright 1976, IEE): p. 731-43.
98. Gómez, M., L. Rancel, B.J. Fernández, and S.F. Medina. Materials Science and Engineering: A, 2009. **501**(1–2): p. 188-196.
99. Cahn, J.W. Acta Metall Mater, 1962. **10**(9): p. 789-798.
100. Dunlop, J.W.C., Y.J.M. Bréchet, L. Legras, and H.S. Zurob. Journal of Nuclear Materials, 2007. **366**(1-2): p. 178-186.
101. Zurob, H.S., G. Zhu, S.V. Subramanian, G.R. Purdy, C.R. Hutchinson, and Y. Brechet. Isij Int, 2005. **45**(5): p. 713-722.
102. Nes, E., N. Ryum, and O. Hunderi. Acta Metall Mater, 1985. **33**(1): p. 11-22.
103. Smith, C.S. Trans. metall. Soc. A.I.M.E., 1948. **175**: p. 15-970.
104. Hutchinson, B., S. Jonsson, and L. Ryde. Scripta metallurgica, 1989. **23**(Compendex): p. 671-676.
105. Sellars, C.M. Mater Sci Tech Ser, 1990. **6**(11): p. 1072-1081.
106. Medina, S.F. and P. Fabregue. J Mater Sci, 1991. **26**(Copyright 1991, IEE): p. 5427-32.
107. Sun, W.P. and E.B. Hawbolt. Isij Int, 1997. **37**(Compendex): p. 1000-1009.

108. Cho, J.R., H.S. Jeong, D.J. Cha, W.B. Bae, and J.W. Lee. J Mater Process Tech, 2005. **160**(1): p. 1-8.
109. Humphreys, F.J. Acta Mater, 1997. **45**(12): p. 5031-5039.
110. Pereda, B., J.M. Rodriguez-Ibabe, and B. López. Isij Int, 2008. **48**: p. 1457.
111. Bailey, J.E. and P.B. Hirsch. Proceedings of the Royal Society of London. Series A. Mathematical and Physical Sciences, 1962. **267**(1328): p. 11-30.
112. Backe, L. Isij Int, 2010. **50**(Compendex): p. 239-247.
113. Hillert, M. Acta Metall Mater, 1965. **13**(3): p. 227-238.
114. Gladman, T. J. Iron Steel Inst., 1967. **205**: p. 653.
115. Zhou, T., R.J. O'Malley, and H.S. Zurob. Metallurgical and Materials Transactions A: Physical Metallurgy and Materials Science, 2010. **41**(8): p. 2112-2120.
116. Feltham, P. Acta Metall Mater, 1957. **5**(2): p. 97-105.
117. Weygand, D., Y. Bréchet, and J. Lépinoux. Acta Mater, 1999. **47**(3): p. 961-970.
118. Tweed, C.J., B. Ralph, and N. Hansen. Acta Metall Mater, 1984. **32**(9): p. 1407-1414.
119. Sarkar, S., A. Moreau, M. Militzer, and W.J. Poole. Metallurgical and Materials Transactions A, 2008. **39**(4): p. 897-907.
120. Manohar, P., D. Dunne, T. Chandra, and C. Killmore. Isij Int, 1996. **36**(2): p. 194-200.
121. Militzer, M., E.B. Hawbolt, T.R. Meadowcroft, and A. Giumelli. Metallurgical and Materials Transactions A, 1996. **27**(11): p. 3399-3409.
122. Miao, C.L., C.J. Shang, G.D. Zhang, and S.V. Subramanian. Materials Science and Engineering: A, 2010. **527**(18–19): p. 4985-4992.
123. Shang, C. and C. Miao, *Refinement of Prior Austenite Grain in Advanced Pipeline Steel*

Advanced Steels, Y. Weng, H. Dong, and Y. Gan, Editors. 2011, Springer Berlin Heidelberg. p. 341-356.

124. Maalekian, M., R. Radis, M. Militzer, A. Moreau, and W.J. Poole. Acta Mater, 2012. **60**(3): p. 1015-1026.
125. Smith, A., G. te Birmingham, and V. Koninkrijk, *Recovery and recrystallization in C-Mn steels following hot deformation*2006: phD-thesis, Delft University of Technology, Delft, the netherlands, iSBn 9077172203.
126. Nanba, S., M. Kitamura, M. Shimada, M. Katsumata, T. Inoue, H. Imamura, Y. Maeda, and S. Hattori. Isij Int, 1992. **32**(3): p. 377-386.
127. Senuma, T., H. Yada, Y. Matsumura, and T. Futamura. Tetsu to Hagane, 1984. **70**: p. 2112.
128. Beynon, J.H. and C.M. Sellars. Isij Int, 1992. **32**(3): p. 359-367.
129. Kang, K.B., O. Kwon, W.B. Lee, and C.G. Park. Scripta Mater, 1997. **36**: p. 1303-1308.
130. Kwon, O. and A.J. DeArdo. Acta metallurgica et materialia, 1991. **39**(4): p. 529-538.
131. Russell, K.C. Advances in Colloid and Interface Science, 1980. **13**(3–4): p. 205-318.
132. Rehman, M.K. and H. Zurob. Metallurgical and Materials Transactions A, 2012: p. 1-10.
133. Winning, M., A.D. Rollett, G. Gottstein, D.J. Srolovitz, A. Lim, and L.S. Shvindlerman. Philosophical Magazine, 2010. **90**(22): p. 3107-3128.
134. Cram, D.G., H.S. Zurob, Y.J.M. Brechet, and C.R. Hutchinson. Acta Mater, 2009. **57**(17): p. 5218-5228.

135. Hughes, D.A. and N. Hansen. *Deformation structures developing on fine scales*. in *Multiscale Modelling of Nano- and Micro-mechanics of Materials*. 2003. Taylor and Francis Ltd.
136. Hughes, D.A., D.C. Chrzan, Q. Liu, and N. Hansen. Phys Rev Lett, 1998. **81**(Copyright 1998, IEE): p. 4664-7.
137. Yoshie, A., T. Fujita, M. Fujioka, K. Okamoto, and H. Morikawa. Isij Int, 1996. **36**(4): p. 467-473.
138. Rios, P.R. Acta Metall Mater, 1987. **35**(12): p. 2805-14.
139. Sinclair, C.W., C.R. Hutchinson, and Y. Bréchet. Metallurgical and Materials Transactions A, 2007. **38**(4): p. 821-830.
140. Kirchner, H. Metallurgical and Materials Transactions B, 1971. **2**(10): p. 2861-2864.
141. J.W.Martin, R.D.Doherty, and B.Cantor. 1997.
142. Siciliano, F. and J. Jonas. Metallurgical and Materials Transactions A, 2000. **31**(2): p. 511-530.
143. Abad, R., A. Fernandez, B. Lopez, and J. Rodriguez-Ibabe. Isij Int, 2001. **41**(11): p. 1373-1382.
144. Militzer, M., E. Hawbolt, and T. Meadowcroft. Metallurgical and Materials Transactions A, 2000. **31**(4): p. 1247-1259.
145. Militzer, M. Isij Int, 2007. **47**(1): p. 1-15.
146. Solhjoo, S. and R. Ebrahimi. J Mater Sci, 2010. **45**(21): p. 5960-5966.
147. Ishikawa, N., N. SHIKANAI, and J. KONDO. CURRENT ADVANCES IN MATERIALS AND PROCESSES, 2007. **20**(6): p. 1268.
148. Okatsu, M., N. Shikanai, and J. Kondo. JFE Technical Report, 2008. **12**: p. 8.
149. Samuel, F., S. Yue, J. Jonas, and B. Zbinden. Isij Int, 1989. **29**(10): p. 878-886.
150. Sims, R.B. Proceedings of the Institution of Mechanical Engineers, 1954. **168**(1): p. 191-200.
151. Bouaziz, O. and P. Buessler. Advanced Engineering Materials, 2004. **6**(1-2): p. 79-83.
152. Kundu, A., in *School of Metallurgy and Materials*2011, University of Birmingham. p. 354.
153. Perdrix, C. Report CECA No 7210 EA/311, IRSID, France, 1987.
154. Echeverrıa, A. and J. Rodriguez-Ibabe. Materials Science and Engineering: A, 2003. **346**(1): p. 149-158.
155. Han, S.Y., S.Y. Shin, C.-H. Seo, H. Lee, J.-H. Bae, K. Kim, S. Lee, and N.J. Kim. Metallurgical and Materials Transactions A, 2009. **40**(8): p. 1851-1862.
156. Subramanian, S., M.K. Rehman, H. Zurob, and J. Gray. International Journal of Metallurgical Engineering, 1926. **2**(1): p. 18-26.
157. Gray, J.M. and F. Siciliano. *High strength microalloyed linepipe: half a century of evolution*. in *Proceedings of the 5th International Conference on Pipeline Technology, Ostend, Belgium*. 2009.
158. Radis, R. and E. Kozeschnik. Modelling and Simulation in Materials Science and Engineering, 2010. **18**(5): p. 055003.
159. Militzer, M. and E. Hawbolt. Weiland, BL Adams and AD Rollett, TMS, Warrendale, PA, 1998. **639**.
160. Gómez, M., L. Rancel, and S. Medina. Metals and Materials International, 2009. **15**(4): p. 689-699.

161. Medina, S., A. Quispe, and M. Gomez. Metallurgical and Materials Transactions A, 2013: p. 1-16.
162. Yoshie, A., M. Fujioka, Y. Watanabe, K. Nishioka, and H. Morikawa. Isij Int, 1992. **32**(Compendex): p. 395-404.
163. Hulka, K. and J. Gray. *High Temperature Processing of Line Pipe Steels*. in *Proceedings of the International Symposium Niobium*. 2001.
164. Devadas, C., D. Baragar, G. Ruddle, I. Samarasekera, and E. Hawbolt. Metallurgical and Materials Transactions A, 1991. **22**(2): p. 321-333.
165. Subramanian, S., F. Boratto, J. Jonas, and C. Sellars. Microalloyed Bar and Forging Steels, 1990: p. 120-136.
166. Akbarzadeh, A., *Effect of thermomechanical processing on microstructure, texture, and anisotropy in two Nb microalloyed steels*1997.
167. Van Minnebruggen, K., W. De Waele, R. Denys, and P. Thibaux. *Strain based design considerations for spiral welded pipelines*. in *Sustainable Construction and Design (SCAD-2012)*. 2012. Ghent University, Laboratory Soete.

9. Appendix 1

Prediction of Rolling Mill Forces:

High rolling Mill forces are a major concern for commercial rolling operation. This problem is more severe for finish rolling stands in tandem hot strip mill.

Since, rolling forces are reactionary forces to deformation, hence knowing the metallurgical state of the rolling stock can allow us to predict rolling forces. Knowledge of expected rolling forces is advantageous to both product development/process optimization teams to optimize/check feasibility of a rolling schedule.

The softening mechanism operating (recovery, recrystallization and precipitation) decides the flow stress evolution of the rolling stock. The metallurgical state of the rolled stock can be represented by the instantaneous flow stress. Since the objective of the rolling force is to overcome the flow stress, hence higher the flow stress, higher will be the rolling load. The multi pass modeling explained in Section 3.3 can predict flow stress of the material. This flow stress includes the effect of grain size refinement, precipitate hardening, temperature, recovery etc. The parameter σ_{FS} is responsible for the difference observed in rollability of IF steel vis-a-vis high Nb steel.

The effect of geometrical parameters/mechanical parameters affecting the rolling force can also be incorporated in the Sim's model.

$$F = \sigma_{FS} \, W \, Q_p \sqrt{R' \, \Delta h} \qquad \textbf{Eq. A119}$$

where, F is rolling force, σ_{FS} is mean flow stress, W is strip width, Q_p is a shape factor, $R'$is effective roll radius and Δh is total reduction.

$$R' = R\left[1 + 0.0225\frac{F}{W\Delta h}\right] \qquad \textbf{Eq. A120}$$

And

$$Q = \frac{1}{2}\sqrt{\frac{1}{r} - 1}\,(T_1 - T_2) - \frac{1}{1.27} \qquad \textbf{Eq. A121}$$

where

$$T_1 = 3.14\ \tan^{-1}\sqrt{\frac{r}{1-r}} \qquad \textbf{Eq. A122}\text{(a)}$$

$$T_2 = \sqrt{\frac{R'}{h}}\ ln\left((1-r)\left(\frac{\phi}{h}\right)^2\right) \qquad \textbf{Eq. A122(b)}$$

$$\phi = h + 2R'\left[1 - \cos\left(\sqrt{\frac{h}{4R'}}\ \tan\left(\frac{1}{2.55}\sqrt{\frac{h}{4R'}}ln(1-r) + \frac{1}{2}\tan^{-1}\left(\sqrt{\frac{r}{1-r}}\right)\right)\right)\right] \qquad \textbf{Eq. A122(c)}$$

$$r = \frac{\Delta h}{H} \qquad \textbf{Eq. A122(d)}$$

$$\Delta h = H - h \qquad \textbf{Eq. A122(e)}$$

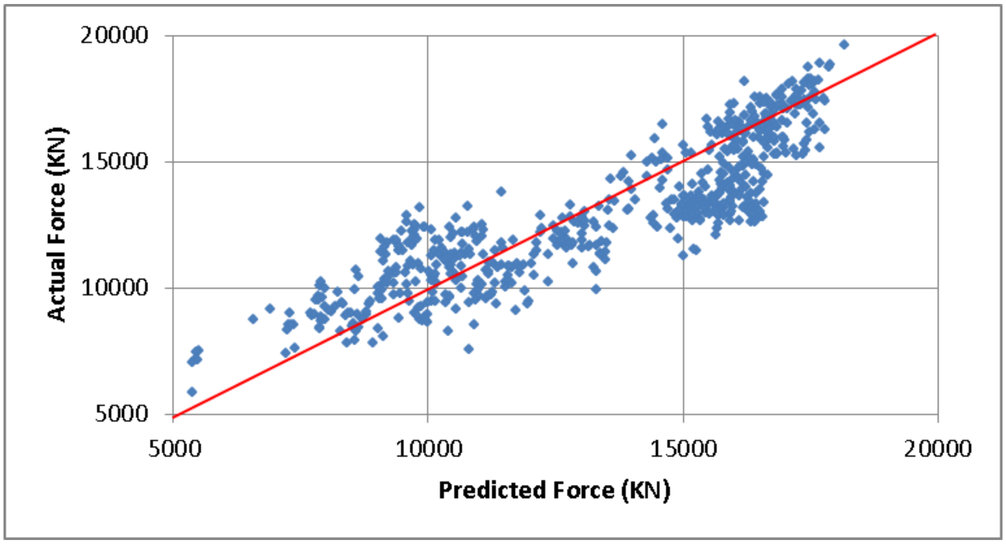

Figure 59: Plot of measured force in finish rolling vs model predicted forces for C-Mn steels.

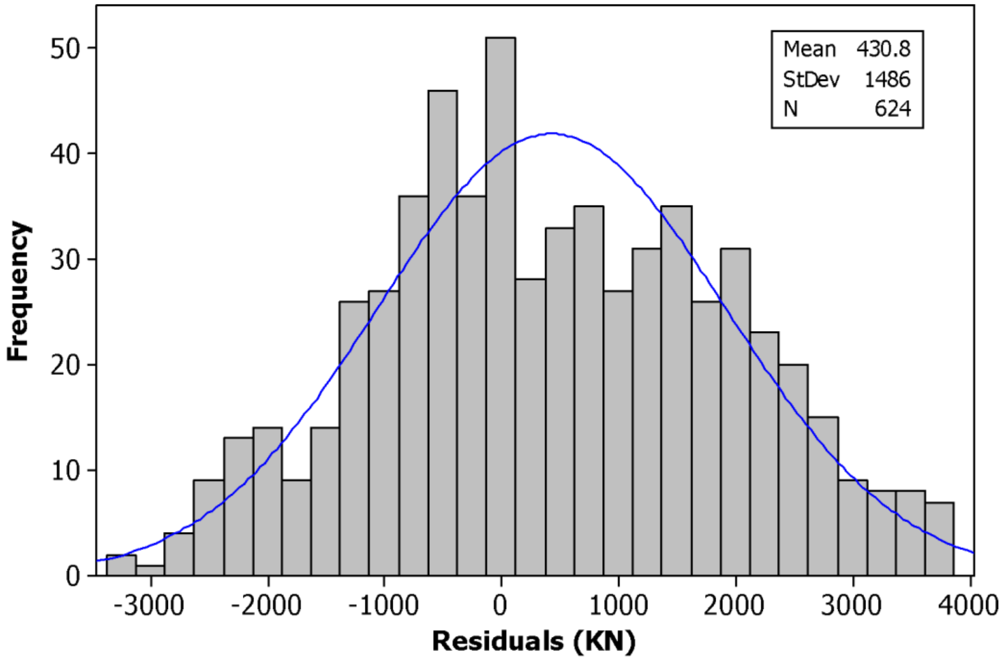

Figure 60: Histogram of residuals (predicted force – actual force) in finish rolling for C-Mn steels

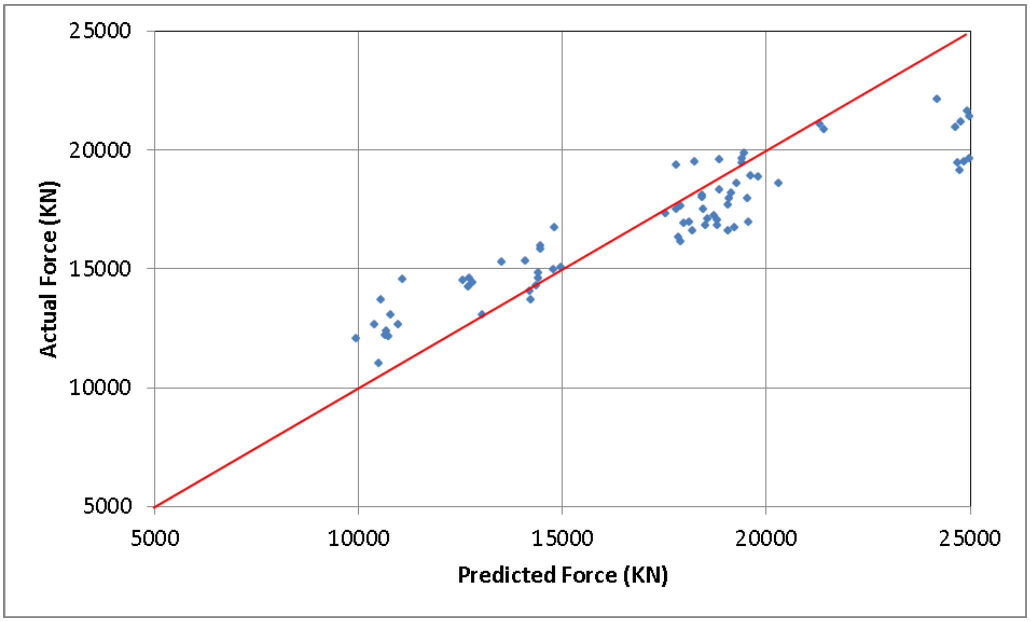

Figure 61: Plot of measured force in finish rolling vs model predicted forces for Nb(<0.07 wt%) microalloyed steels.

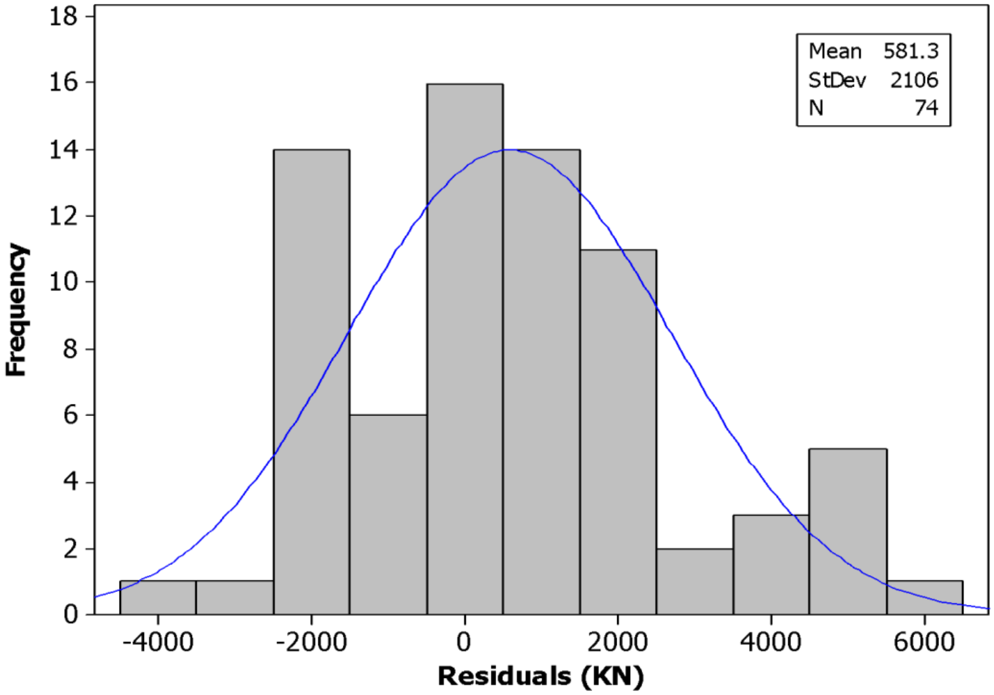

Figure 62: Histogram of residuals (predicted force – actual force) in finish rolling for Nb(<0.07 wt%) microalloyed steels.

10. Appendix 2

The model has been coded in Microsoft Visual Basic 2010. The graphical user interface for single pass deformation is shown below along with the codes.

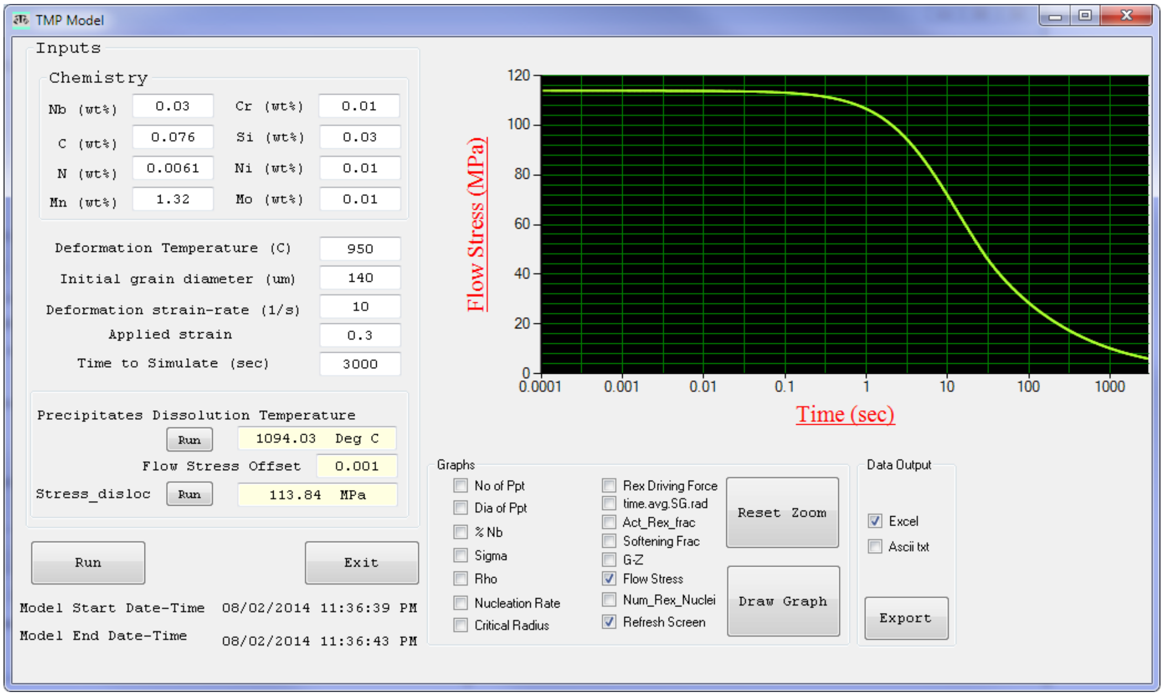

TMP Model

Inputs

Chemistry

Nb (wt%) 0.03
C (wt%) 0.076
N (wt%) 0.0061
Mn (wt%) 1.32
Cr (wt%) 0.01
Si (wt%) 0.03
Ni (wt%) 0.01
Mo (wt%) 0.01

Deformation Temperature (C) 950
Initial grain diameter (um) 140
Deformation strain-rate (1/s) 10
Applied strain 0.3
Time to Simulate (sec) 3000

Precipitates Dissolution Temperature 1094.03 Deg C
Flow Stress Offset 0.001
Stress_disloc 113.84 MPa

Model Start Date-Time 08/02/2014 11:36:39 PM
Model End Date-Time 08/02/2014 11:36:43 PM

Graphs
☐ No of Ppt
☐ Dia of Ppt
☐ % Nb
☐ Sigma
☐ Rho
☐ Nucleation Rate
☐ Critical Radius
☐ Rex Driving Force
☐ time.avg.SG.rad
☐ Act_Rex_frac
☐ Softening Frac
☐ G-Z
☑ Flow Stress
☐ Num_Rex_Nuclei
☑ Refresh Screen

Data Output
☑ Excel
☐ Ascii txt

Figure 63: Screenshot of the model interface highlighting the input and output.

```
Imports System
Imports Microsoft.VisualBasic
Imports System.IO
Imports System.Collections
Imports System.Drawing
Imports System.Drawing.Imaging
Imports System.Drawing.Image
Imports System.Drawing.Text
Imports System.Drawing.Drawing2D
Imports System.Windows.Forms.DataVisualization.Charting

Public Class Form1
    Dim Tsol, NbT, CT, NT, NBT0, NT_temporary, MnT, Di, strainrate, astrain,
fraction_Nb_dis, Uo, Vo, QS, FZ, b, Rg, Dv, Db, Dp, Deff, alpha, SE, GB, mu, Y_mod,
rhot, a, ab, Vm, density, MW, k, M_Taylor, alpha_Taylor, Debye, M_NbT, AR, dSdt, inc As
Double
    Dim cells As Integer = 1000000
    Dim pi As Double = Math.PI
    Dim sqrt_half_pi = Math.Sqrt(pi / 2)
    Dim sqrt_pi = Math.Sqrt(pi)
```

```
    Dim R, Nc(cells), time(cells), Radius(cells), N(cells), dRdt(cells), dNdt(cells),
Nbl(cells), FN, Temp, dNdt2(cells), Zener(cells), Force(cells), X(cells), SIGMA(cells),
rho(cells), Rzero(cells), dNdtC(cells), Rstar(cells), coarsef(cells), Vf(cells),
Vfc(cells), S3T(cells) , K1, K2, K3, K4, Nbo, Nb0, Nb1, Nb2, Nb3, Nb4, w, ke, dNb,
ks_general, ks_bulk As Double
    Dim R0t, Rt, FvEq, Ntot, NbEqR, fcoarse, dNtdt, Avrami, dNtdt2, dRtdtc, R0, NbR,
dNtdtC, dRtdt, dRtdtg, dRtdt2, NbEqRbar, radius_temp, x1, x2, x_intermediate, counter,
f1, f_intermediate, C, Nb, Ns, NbEq, f, ks, Gv, Vol, Area, RC, dGt, dGtdr, r_nt, G_nt,
dGtdr_for_R0, r_nt0, flow, FC, this2, PR, PR2, Nbtemp, this, Pnet, VV, kf, V1, V2, P1,
P2, sflimit, Sv, Dcrt, Num_rex, Eb, beta, Mi, GR(cells), G_Z(cells), S1, S2, samplingF,
j, kshear, strainT, RcH, STDEV, STDEVR, Kd, intI, intII, Spptn(cells) , DRf, c1_AR, c2,
nbx(6000, 6000), table(500000, 1), F_left, F_right, l1, l2, l3, l4, Rtemp, Ntemp,
GNoutB, GRoutB, CNoutB, CRoutB, NoutB, RoutB, incs, Nst, Rst, NbsT, h As Double
    Dim Niterations, time2simulate, Nbtime_coarsening_flag As Integer
    Dim temporary4, temporary5, temporary1, temporary2, temporary3, temporary0,
rec_contribution(cells), rex_contribution, k1x, k1y, k2x, k2y, k3x, k3y, k4x, k4y,
S3_with_rex As Double
    Dim interval As Double = 0.0000000000000001
    Dim dC1, dC2, dC2a, dC3, dC4, dC5, Ca, Cb, Ns_a, Ns_b, c_equv, Ns_equv, C_Ns_Eq,
d2GtdrdNb_c1, radius_sb(cells), Non_Rex_R(cells), ppt_VF(cells),
radius_critical(cells), R_subgrain_avg(cells), Rex_subgrain_mob_fit1,
Mobility_LowAngle(cells), rho_integral, N_nuclei(cells), chi_critical(cells),
Act_Rex_Vol_frac(cells),M_HAG(cells), appld_stress, softening_fraction(cells),
A_coarsening(cells), B_coarsening(cells), kC_Maple(cells), rho_zero As Double
    Dim phase2_growth(cells), film_nucleation(cells), flow_softening(cells),
Nucleation_Volume(cells), rc1, c1, l(cells), R0_plus_MGdt(cells),ppt_spacing,
SG_Driving_force(cells), Growth_Driving_Force(cells),nuclei_fraction_cumu(cells),
nuclei_fraction_const, R_Eqv, zener_new(cells),Act_L(cells), N_nuclei_cumu(cells),
growth_rate(cells) As Decimal
    Dim N_available_per_grain(cells), Nucleation_V_cumu(cells), Growth_velocity,
RrexN(cells), Growth_Vol(cells) As Double
    Dim pi_sp As Double = (4 / 3) * pi

    Private Sub Button1_Click(ByVal sender As System.Object, ByVal e As
System.EventArgs) Handles Button1.Click 'Run button
        Process.GetCurrentProcess().PriorityClass = ProcessPriorityClass.High
        Button1.Visible = False : btn_Exit.Visible = False : Label1.Visible = False :
Label2.Visible = False : Label17.Text = Date.Now : Label17.Visible = False :
Label18.Visible = False
        Call initialise_variables()
        Call data_reader_and_initialize_constants()
        M_NbT = (NbT * 55.85) / (100 * 92.9) 'weight percent Nb is converted to atomic
fraction to be used in Cahn's eq
        K1 = 10 ^ ((-7900 / Temp) + 3.42) 'solubility product of NbC.
        K2 = 10 ^ ((-8500 / Temp) + 2.8) 'solubility product of NbN.
        'Solving for dNb('Equilibrium Nb in solution) using bisection method
        x1 = 0 : x2 = NbT
        While (Math.Abs(x2 - x1) > 2 * 0.00000001)
            Dim kk As Decimal = dNb_func(x2)
            x_intermediate = (x1 + x2) / 2
            If ((dNb_func(x1) * dNb_func(x_intermediate)) < 0) Then
                x2 = x_intermediate
            ElseIf ((dNb_func(x2) * dNb_func(x_intermediate) < 0)) Then
                x1 = x_intermediate
            End If
        End While
        dNb = (x1 + x2) / 2 'Equilibrium Nb in solution
```

```
        w = CT / (K1 / dNb + 12 * (NbT - dNb) / 93) 'mole fraction calculation
NbC(w)N(1-w)
        ke = (K1 ^ w) * (K2 ^ (1 - w)) * (w ^ w) * (1 - w) ^ (1 - w)    'Equilibrium
value of solubility constant for carbonitride
        d2GtdrdNb_c1 = (-4 * Rg * Temp * pi) / (3 * Vm)
        NbEq = dNb ';Equilibrium Nb in solution.
        r_nt0 = r_nt_func(NbT) ' initial critical radius r_nt0 calculated when Nb=NbT
        Radius(0) = r_nt0 'Initial value of critical radius (Nb=NbT)
        R0 = R0t_func(Radius(0), NbT)
        Nb = NbT
        Call NbEqR_sub(0) 'solving dGtdr_for_R0_func for Nb when the critical radius is
fixed
        Call NbEqRbar_sub(0)
        N(0) = 1.0E+15  'number of precipitates per m3, an initial guess.
        Call flowstress_calculation() 'sets the initial condition
        rho(0) = (flow / (M_Taylor * alpha_Taylor * mu * b)) ^ 2 'initial dislocation
density
        rho_zero = rho(0) 'Initializing
        Nc(0) = 1 * rho(0) ^ (1.5) ''Number of dislocation nodes.
        dNdt(0) = dNtdt_func(rho(0), N(0), NbT) ' Ppt dN/dt during nucleation and
growth.
        dNdt2(0) = dNtdt2_func(rho(0), Radius(0), N(0), NbT) ' Ppt dN/dt during growth
and coarsening.
        dNdtC(0) = dNtdtC_func(rho(0), Radius(0), N(0), NbT) 'Ppt number density
disappearance during coarsening.
        dRdt(0) = dRtdt_func(rho(0), Radius(0), N(0), NbT)   'dR/dt during nucleation
and growth.
        Vf(0) = N(0) * (4 / 3) * pi * ((Radius(0)) ^ 3) 'Volume fraction of the
precipitates
        SIGMA(0) = rho(0) ^ (1 / 2) * b * mu * alpha_Taylor * M_Taylor 'dislocation
stress at a given time t
        Nbl(0) = NbT
        time(0) = 0 'array for keeping time
        inc = 0.000000000001 'time increment
        FC = 0 'variable to identify the completion of precipitation.
        this2 = 0
        PR = 0 : PR2 = 0 '(introduced to help with programming).
        ab = 0 '(introduced to help with programming, ab=1 means nucleation+growth).
        Nbtemp = NbR
        appld_stress = nippon_func(NbT, astrain) 'empirical equation of Yoshie
describing stress-strain.
        Sv = ((24 / (pi * Di)) * (0.491 * Math.Exp(astrain) + 0.155 * Math.Exp(-1 *
astrain) + 0.143 * Math.Exp(-3 * astrain))) 'surface to volume ratio of the deformed
grains.
        Eb = (QS / 6.023E+23) 'Nb binding energy in J/atom.
        'Start of big step in Rouge-Kutta method __________growth first:
        For i As Integer = 1 To cells
            If (-1 < (CDbl(dNdt(i - 1) + dNdt2(i - 1)))) Then
                '============= GROWTH COARSENING MODE=========================
                ab = 1
                Nb = Nbl(i - 1)
                Ntemp = N(i - 1)
                Rtemp = Radius(i - 1)
                l1 = inc * CDbl(dNtdt_func(rho(i - 1), N(i - 1), Nb))
                K1 = inc * CDbl(dRtdt_func(rho(i - 1), Radius(i - 1), N(i - 1), Nb))
                Ntemp = N(i - 1) + l1 / 2
                Rtemp = Radius(i - 1) + K1 / 2
                Nb = CDbl(Nbtime_func(Ntemp, Rtemp, i))
```

```
l2 = inc * CDbl(dNtdt_func(rho(i - 1), Ntemp, Nb))
K2 = inc * CDbl(dRtdt_func(rho(i - 1), Rtemp, Ntemp, Nb))
Ntemp = N(i - 1) + l2 / 2
Rtemp = Radius(i - 1) + K2 / 2
Nb = CDbl(Nbtime_func(Ntemp, Rtemp, i))
l3 = inc * CDbl(dNtdt_func(rho(i - 1), Ntemp, Nb))
K3 = inc * CDbl(dRtdt_func(rho(i - 1), Rtemp, Ntemp, Nb))
Ntemp = N(i - 1) + l3
Rtemp = Radius(i - 1) + K3
Nb = CDbl(Nbtime_func(Ntemp, Rtemp, i))
l4 = inc * CDbl(dNtdt_func(rho(i - 1), Ntemp, Nb))
K4 = inc * CDbl(dRtdt_func(rho(i - 1), Rtemp, Ntemp, Nb))
GNoutB = N(i - 1) + l1 / 6.0 + l2 / 3.0 + l3 / 3.0 + l4 / 6.0
GRoutB = Radius(i - 1) + K1 / 6.0 + K2 / 3.0 + K3 / 3.0 + K4 / 6.0
NoutB = GNoutB : RoutB = GRoutB
incs = inc / 2.0
Nb = Nbl(i - 1)
l1 = incs * CDbl(dNtdt_func(rho(i - 1), N(i - 1), Nb))
K1 = incs * CDbl(dRtdt_func(rho(i - 1), Radius(i - 1), N(i - 1), Nb))
Rtemp = Radius(i - 1) + K1 / 2.0
Ntemp = N(i - 1) + l1 / 2.0
Nb = CDbl(Nbtime_func(Ntemp, Rtemp, i))
l2 = incs * CDbl(dNtdt_func(rho(i - 1), Ntemp, Nb))
K2 = incs * CDbl(dRtdt_func(rho(i - 1), Rtemp, Ntemp, Nb))
Rtemp = Radius(i - 1) + K2 / 2.0
Ntemp = N(i - 1) + l2 / 2.0
Nb = CDbl(Nbtime_func(Ntemp, Rtemp, i))
l3 = incs * CDbl(dNtdt_func(rho(i - 1), Ntemp, Nb))
K3 = incs * CDbl(dRtdt_func(rho(i - 1), Rtemp, Ntemp, Nb))
Rtemp = Radius(i - 1) + K3
Ntemp = N(i - 1) + l3
Nb = Nbtime_func(Ntemp, Rtemp, i)
l4 = incs * CDbl(dNtdt_func(rho(i - 1), Ntemp, Nb))
K4 = incs * CDbl(dRtdt_func(rho(i - 1), Rtemp, Ntemp, Nb))
Nst = N(i - 1) + l1 / 6.0 + l2 / 3.0 + l3 / 3.0 + l4 / 6.0
Rst = Radius(i - 1) + K1 / 6.0 + K2 / 3.0 + K3 / 3.0 + K4 / 6.0
NbsT = Nbtime_func(Nst, Rst, i)
Nb = NbsT
l1 = incs * CDbl(dNtdt_func(rho(i - 1), Nst, Nb))
K1 = incs * CDbl(dRtdt_func(rho(i - 1), Rst, Nst, Nb))
Rtemp = Rst + K1 / 2.0
Ntemp = Nst + l1 / 2.0
Nb = Nbtime_func(Ntemp, Rtemp, i)
l2 = incs * CDbl(dNtdt_func(rho(i - 1), Ntemp, Nb))
K2 = incs * CDbl(dRtdt_func(rho(i - 1), Rtemp, Ntemp, Nb))
Rtemp = Rst + K2 / 2.0
Ntemp = Nst + l2 / 2.0
Nb = CDbl(Nbtime_func(Ntemp, Rtemp, i))
l3 = incs * CDbl(dNtdt_func(rho(i - 1), Ntemp, Nb))
K3 = incs * CDbl(dRtdt_func(rho(i - 1), Rtemp, Ntemp, Nb))
Rtemp = Rst + K3
Ntemp = Nst + l3
Nb = CDbl(Nbtime_func(Ntemp, Rtemp, i))
l4 = incs * CDbl(dNtdt_func(rho(i - 1), Ntemp, Nb))
K4 = incs * CDbl(dRtdt_func(rho(i - 1), Rtemp, Ntemp, Nb))
N(i) = Nst + l1 / 6.0 + l2 / 3.0 + l3 / 3.0 + l4 / 6.0
Radius(i) = Rst + K1 / 6.0 + K2 / 3.0 + K3 / 3.0 + K4 / 6.0
Nbl(i) = Nbtime_func(N(i - 1), Radius(i - 1), i)
```

```
                Nb = Nbl(i)
            Else
                '======================= COARSENING MODE=====================
                ab = 0    'change done here
                PR = PR + 1
                Nb = Nbl(i - 1)
                l1 = inc * CDbl(dNtdt2_func(rho(i - 1), Radius(i - 1), N(i - 1), Nb))
                K1 = inc * CDbl(dRtdt2_func(rho(i - 1), N(i - 1), Radius(i - 1), Nb))
                Rtemp = Radius(i - 1) + K1 / 2.0
                Ntemp = N(i - 1) + l1 / 2.0
                l2 = inc * CDbl(dNtdt2_func(rho(i - 1), Rtemp, Ntemp, Nb))
                K2 = inc * CDbl(dRtdt2_func(rho(i - 1), Ntemp, Rtemp, Nb))
                Rtemp = Radius(i - 1) + K2 / 2.0
                Ntemp = N(i - 1) + l2 / 2.0
                l3 = inc * CDbl(dNtdt2_func(rho(i - 1), Rtemp, Ntemp, Nb))
                K3 = inc * CDbl(dRtdt2_func(rho(i - 1), Ntemp, Rtemp, Nb))
                Rtemp = Radius(i - 1) + K3
                Ntemp = N(i - 1) + l3
                l4 = inc * CDbl(dNtdt2_func(rho(i - 1), Rtemp, Ntemp, Nb))
                K4 = inc * CDbl(dRtdt2_func(rho(i - 1), Ntemp, Rtemp, Nb))
                CNoutB = N(i - 1) + l1 / 6.0 + l2 / 3.0 + l3 / 3.0 + l4 / 6.0
                CRoutB = Radius(i - 1) + K1 / 6.0 + K2 / 3.0 + K3 / 3.0 + K4 / 6.0
                NoutB = CNoutB : RoutB = CRoutB
                N(i) = CNoutB
                Radius(i) = CRoutB
                incs = inc / 2.0
                Nbl(i) = Nbtime_func(N(i), Radius(i), i)
                Nb = Nbl(i)
            End If
            If (Nc(i - 1) > N(i)) Then  'Nc is dislocation node density and N is ppt no
density
                Call Recovery_Module(i)
            Else
                SIGMA(i) = SIGMA(i - 1) ' Recovery is completely pinned
            End If
            rho(i) = (SIGMA(i - 1) / (M_Taylor * alpha_Taylor * mu * b)) ^ 2
            time(i) = time(i - 1) + inc ''Time and increment are determined here!
            If (Math.Abs((Radius(i) - RoutB) / Radius(i)) > 0.0002) Then
                inc = 1.5 * incs : ElseIf (time(i) < 0.0001) Then : inc = 4 * incs :
ElseIf (PR2 > 1) Then
                inc = 2.2 * incs : Else : inc = time(i) / 100
            End If
            inc = Math.Min(2, inc) 'Adaptive time increment steps used
            'Note that once we enter into the coarsening regime dNdt will be set to
zero.
            If (N(i) < Ntot_func(rho(i))) Then
                Avrami = CDbl(1 - (N(i) / Ntot_func(rho(i))))
            Else
                Avrami = 0
            End If
            If (dNdt(i - 1) > 1.0E-100) Then
                dNdt(i) = dNtdt_func(rho(i), N(i), Nb)
            Else
                dNdt(i) = 0
            End If
            dNdt2(i) = CDbl(dNtdt2_func(rho(i), Radius(i), N(i), Nb))
            Nc(i) = 0.5 * (rho(i) ^ (1.5))
            Vfc(i) = CDbl(Nc(i) * (4 / 3) * pi * 1.0E-27)
```

```
            ab = 0
            Call NbEqR_sub(i)     'Nb interface concentration in equilibrium with a
particle of size R
            Call NbEqRbar_sub(i)  'Nb matrix concentration when the average particle
size is R
            NT = N(i)
            coarsef(i) = CDbl(fcoarse_func(Radius(i), Nbl(i))) 'Coarsening function
used for switch from nucleation+growth to growth+coarsening
            If (coarsef(i) > 0.998 And FC = 0 And PR > 1) Then
                Nbtime_coarsening_flag = 1 : FC = 1
                PR2 = PR : Nbtemp = 0
                Rt = r_nt_func(Nb)
                R0 = CDbl(R0t_func(Radius(i), Nbl(i)))
                dNdt2(i) = CDbl(dNtdt2_func(rho(i), Radius(i), N(i), Nb))
                dNdtC(i) = dNdt2(i) 'reassign the whole funtion
            End If
            R0 = CDbl(R0t_func(Radius(i), Nb))
            Rzero(i) = R0
            r_nt = r_nt_func(Nb) 'radius of the critical nucleus.
            Rstar(i) = CDbl(r_nt)
            dNdtC(i) = CDbl(dNtdtC_func(rho(i), Radius(i), N(i), Nb))
            If (time(i) > time2simulate) Then   'Time at which we stop and exit the
loop
                this = i : i = cells : cells = this  '# of loops actually used.
            End If
        Next i
        Call recrystalization_model()
        Call Hardening_model()
        Label18.Text = Date.Now : Label1.Visible = True : Label2.Visible = True :
Button1.Visible = True : btn_Exit.Visible = True : Label17.Visible = True :
Label18.Visible = True : Process.GetCurrentProcess().PriorityClass =
ProcessPriorityClass.Normal
    End Sub
    Private Function C_func(ByVal Nb As Decimal) As Double 'C left in solution.
        NbT = NBT0
        C = CT - w * (NbT - Nb) * 12 / 93
        Return (C)
    End Function
    Private Function dsolve_dSdt_RK(ByVal i As Integer, ByVal y As Decimal) As Double
'recovery model
        Act_L(i) = Math.Min((35 * b), (b / (6.3 * b * Math.Sqrt(rho(i - 1)) + 0.042 *
(Nbl(1) ^ 0.3333))))   'Activation length
        If Act_L(i) = 0 Then Act_L(i) = Act_L(i - 1)
        Vo = Act_L(i) * b ^ 2
        c2 = Vo / (k * Temp)
        dSdt = ((N(i) * sizefactor_func(i) / Nc(i - 1)) - 1) * c1_AR * (y ^ 2) *
Math.Sinh(c2 * y)
        Return (dSdt)
    End Function
    Private Function dNb_func(ByVal x As Decimal) As Double  'Method described by
Gladman to calculate the solubility and composition of Nb carbonitrides
        Nbo = x
        Nb4 = -12 * 14 * Nbo ^ 4
        Nb3 = (2 * NbT * 12 * 14 - CT * 14 * 93 - NT * 12 * 93) * Nbo ^ 3
        Nb2 = (12 * 93 * K2 + NT * NbT * 12 * 93 - NbT ^ 2 * 12 * 14 + 93 * 14 * K1 +
CT * NbT * 14 * 93) * Nbo ^ 2
        Nb1 = (NT * K1 * 93 * 93 - NbT * K2 * 93 * 12 - NbT * K1 * 93 * 14 + CT * K2 *
93 * 93) * Nbo
```

```
        Nb0 = -(K1 * K2 * 93 * 93)
        Return (Nb4 + Nb3 + Nb2 + Nb1 + Nb0)
    End Function
    Private Function dGt_func(ByVal Nb As Decimal, ByVal r As Decimal) As Double
'energy balance for nucleation.
        Vol = (4 / 3 * pi * r ^ 3) ';volume of nucleus.
        Area = (4 * pi * r ^ 2) ';surface area of nucleus.
        ks = (Nb * (C_func(Nb) ^ w) * (Ns_func(Nb) ^ (1 - w)) / ke) ';solubility
constant of carbonitride.
        Gv = (Rg * Temp * Math.Log(ks)) / Vm 'Chemical driving force for precipitation.
        dGt = (-Vol * Gv) + (Area * SE) - ((r * mu * b ^ 2) * (0.2 + ((0.7142857143 /
pi) * (Math.Log(r / RC)))))  'energy balance for nucleation
        Return (dGt)
    End Function
    Private Function dGtdr_func(ByVal r As Decimal, ByVal Nb As Decimal) As Double
'Derivative of dGt wrt r
        ks = (Nb * (C_func(Nb) ^ w) * (Ns_func(Nb) ^ (1 - w)) / ke) ';solubility
constant of carbonitride.
        dC2 = dC2a * Math.Log(ks)
        dGtdr = (dC1 * r) - (dC2 * r ^ 2) - (dC3 * (dC4 + Math.Log(r))) - dC5
'deribative of dGt with respect to time.
        Return dGtdr
    End Function
    Private Function dGtdr_for_R0_func(ByVal Nb As Decimal, ByVal R As Decimal) As
Double
        Return (dGtdr_func(R, Nb)) 'derivative of dGt with respect to time
    End Function
    Private Function dgtdr_solver_Nb_func(ByVal x1 As Double, ByVal x2 As Double, ByVal
tol As Double, ByVal rad As Double) As Double
        'Solving dGtdr funtion
        Dim tolerance As Double = 0
        Dim stepsize = 0.00001
        Dim func As Double = 0
        Dim dfunc As Double = 0
        tolerance = Math.Abs(x2 - x1)
        While (tolerance > 2 * tol)
            func = dGtdr_func(rad, x1)
            dfunc = (dGtdr_func(rad, x1 + stepsize) - dGtdr_func(rad, x1 - stepsize)) /
(2 * stepsize)
            x2 = x1 - func / dfunc
            tolerance = Math.Abs(x2 - x1)
            x1 = x2
        End While
        Return (x2)
    End Function
    Private Function d2Gtdr2_func(ByVal x As Decimal, ByVal Nb As Decimal) As Double
        Return (dC1 - (2 * dC2 * x) - (dC3 / x)) 'double differential of dGt
    End Function
    Private Function Deff_func(ByVal rho As Decimal) As Double
        Dim constant As Double = pi * b ^ 2 * rho_zero
        Deff = (Dp * constant) + (Dv * (1 - constant))
        Return (Deff) 'effective diffusion const
    End Function
    Private Function dNtdt_func(ByVal rhot As Decimal, ByVal N As Decimal, ByVal Nb As
Decimal) As Double
        dNtdt = (0.01 * Avrami * FN * rhot * Nb * 55.85 * Dp * Math.Exp((-1 *
G_nt_func(Nb)) / (k * Temp))) / (b * a * a * 92.9)
        Return (dNtdt) 'dN/dt during nucleation and growth.
```

```
    End Function
    Private Function dNtdt2_func(ByVal rho As Decimal, ByVal r As Decimal, ByVal N As
Decimal, ByVal Nb As Decimal) As Double
        dNtdt2 = fcoarse_func(r, Nb) * dNtdtC_func(rho, r, N, Nb)
        Return (dNtdt2) 'dN/dt during growth and coarsening.
    End Function
    Private Function dNtdtC_func(ByVal rho As Double, ByVal r As Double, ByVal N As
Double, ByVal Nb As Double) As Double
        Dim temp_var1 As Double = (4 * pi * (r ^ 3) / 3)
        dNtdtC = (dRtdtc_func(rho, r) / r) * ((R0 * Nb / (r * (88 - NBT0))) *
(temp_var1 * N * N - (2 * N) + (1 / temp_var1)) - (3 * N)) 'NBT0 is amount of Nb in
solution for a givrn temperature. T represnts temp and t is time
        Return (dNtdtC) 'Rate at which nuclei disappear due to coarsening.
    End Function
    Private Function dRtdt_func(ByVal rho As Double, ByVal Rt As Double, ByVal NT As
Double, ByVal Nb As Double) As Double
        dRtdt = dRtdtg_func(rho, Rt) + ((dNtdt_func(rho, NT, Nb) * ((alpha *
r_nt_func(Nb)) - Rt) / NT)) 'dR/dt during nucleation & growth.
        Return (Math.Abs(dRtdt))
    End Function
    Private Function dRtdtg_func(ByVal rho As Double, ByVal Rt As Double) As Double
        dRtdtg = Deff_func(rho) * (Nb - NbEqR) / (Rt * (88 - NbEqR))
        Return (Math.Abs(dRtdtg))
    End Function
    Private Function dRtdtc_func(ByVal rho As Double, ByVal r As Double) As Double
        dRtdtc = (Deff_func(rho) * (NbEqR - NbEqRbar)) / (r * (88 - NbEq)) ':coarsening
contribution to dR/dt during growth & coarsening.
        Return (Math.Abs(dRtdtc))
    End Function
    Private Function dRtdt2_func(ByVal rho As Double, ByVal Nt As Double, ByVal Rt As
Double, ByVal niobium As Double) As Double
        dRtdt2 = ((1 - fcoarse_func(Rt, niobium)) * dRtdtg_func(rho, Rt)) +
(fcoarse_func(Rt, niobium) * dRtdtc_func(rho, Rt))
        Return (Math.Abs(dRtdt2))
    End Function
    Private Sub NbEqR_sub(ByVal i As Integer)
        x1 = 0.99 * NbEq : x2 = 2.01 * Nb
        While (Math.Abs(x2 - x1) > 2 * 0.00001)
            x_intermediate = (x1 + x2) / 2
            F_left = dGtdr_for_R0_func(x1, Radius(i))
            F_right = (dGtdr_for_R0_func(x2, Radius(i)))
            f_intermediate = dGtdr_for_R0_func(x_intermediate, Radius(i))
            If (F_left * f_intermediate < 0) Then
                x2 = x_intermediate
            ElseIf (F_right * f_intermediate < 0) Then
                x1 = x_intermediate
            End If
        End While
        NbEqR = (x1 + x2) / 2
    End Sub
    Private Sub NbEqRbar_sub(ByVal i As Integer)
        x1 = 0.8 * NbEq
        x2 = 1.1 * Nb
        x1 = 0
        x2 = 0.171
        While (Math.Abs(x2 - x1) > 2 * 0.00001)
            x_intermediate = (x1 + x2) / 2
```

```
            If ((dGtdr_for_R0_func(x1, Radius(i) * 27 / 23) *
dGtdr_for_R0_func(x_intermediate, Radius(i) * 27 / 23)) < 0) Then
                x2 = x_intermediate
            ElseIf ((dGtdr_for_R0_func(x2, Radius(i) * 27 / 23) *
dGtdr_for_R0_func(x_intermediate, Radius(i) * 27 / 23)) < 0) Then
                x1 = x_intermediate
            End If
        End While
        NbEqRbar = (x1 + x2) / 2
    End Sub
    Private Function erf_func(ByVal z As Decimal) As Double
        If z < 0 Then
            Return ((2 * gauss(z * Math.Sqrt(2))) - 1)
        Else
            Return (1 - (2 * gauss(-1 * z * Math.Sqrt(2))))
        End If
    End Function
    Private Function norm(ByVal z As Double) As Double
        Dim Q As Double = 0
        Q = z ^ 2
        If Math.Abs(z) > 7 Then
            Return ((1 - (1 / Q) + (3 / (Q ^ 2))) * (Math.Exp(-Q / 2)) / (sqrt_half_pi
* Math.Abs(z)))
        Else
            Return (chisq(Q, 1))
        End If
    End Function
    Private Function chisq(ByVal x As Double, ByVal n As Integer) As Double
        Dim alpha, q, t As Double
        Dim remainder, quotient, k, a As Integer
        alpha = 0 : q = 0 : t = 0 : remainder = 1 : quotient = 1 : k = 1 : a = 1
        If (x > 1000 Or n > 1000) Then
            alpha = ((2 / (9 * n)) - 1 + ((x / n) ^ (1 / 3))) / (Math.Sqrt(2 / (9 *
n)))
            q = 0.5 * norm(alpha)
            If (x > n) Then
                Return (q)
            Else
                Return (1 - q)
            End If
        Else
            Dim p As Double = 1 / (Math.Exp(0.5 * x))
            quotient = Math.DivRem(n, 2, remainder)

            If remainder = 1 Then
                p = p * Math.Sqrt(2 * x / pi)
            End If
            k = n
            While (k >= 2)
                p = p * x / k
                k = k - 2
            End While
            t = p
            a = n
            While (t > p * 0.000000000000001)
                a = a + 2
                t = t * x / a
                p = p + t
```

```
            End While
            Return (1 - p)
        End If
    End Function
    Private Function gauss(ByVal Z As Double) As Double
        If Z < 0 Then
            If Z < -10 Then
                Return (0)
            Else
                Return ((chisq(Z ^ 2, 1)) / 2)
            End If
        ElseIf Z > 10 Then
            Return (1)
        Else
            Return (1 - ((chisq(Z ^ 2, 1)) / 2))

        End If

    End Function
    Private Function fcoarse_func(ByVal Rt As Double, ByVal niobium As Double) As
Double
        Dim value As Decimal = 0
        If Nbtime_coarsening_flag = 1 Then
            Return (1)
        Else
            value = 4 * ((Rt / r_nt_func(niobium)) - 1)
            fcoarse = (1 - erf_func(value))
            Return (fcoarse)
        End If
    End Function
    Private Function G_nt_func(ByVal Nb As Decimal) As Double 'Activation energy for
nucleation
        radius_temp = r_nt_func(Nb)
        G_nt = dGt_func(Nb, radius_temp)
        Return (G_nt)
    End Function
    Private Function Nbtime_func(ByVal Nt As Double, ByVal Rt As Double, ByVal j As
Integer) As Double
        If Nbtime_coarsening_flag = 0 Then
            Return ((NBT0 - (88 * pi * Nt * (Rt ^ 3) * 4 / 3)) / (1 - (pi * Nt * (Rt ^
3) * (4 / 3))))
        Else
            Return (dgtdr_solver_Nb_func(0.001, 0.1, 0.00000001, Rt))
        End If
    End Function
    Private Function nippon_func(ByVal Nb As Decimal, ByVal strain As Decimal) As
Double
        Return ((8.630299296 * (strain ^ 0.223) * (strainrate ^ 0.048) * (Math.Exp(3.01
* Nb)) * (Math.Exp(2880 / Temp))) / (Di ^ 0.07))
    End Function
    Private Function Ns_func(ByVal Nb As Decimal) As Double
        NbT = NBT0
        NT = NT_temporary
        Ns = NT - (1 - w) * (NbT - Nb) * 14 / 93 ';Nitrogen left in solution.
        Return (Ns)
    End Function
    Private Function Ntot_func(ByVal rhot As Decimal) As Double 'Total nucleation sites
        Ntot = FN * rhot / b
```

```
        Return (Ntot)
    End Function
    Private Function R0t_func(ByVal Rt As Decimal, ByVal Nb As Decimal) As Double
        R0t = Rt * Math.Log(Nb / NbEq)
        Return (R0t)
    End Function
    Private Function r_nt_func(ByVal Nb As Decimal) As Double 'radius of the critical
nucleus, depends upon Nb concentration.
        Dim tol As Double = 0
        x1 = 0.000001 ' the initial value
        x2 = 0.000000000001 ' the initial value
        tol = Math.Abs(x2 - x1)
        While (tol > 2 * 0.0000000000001)
            x2 = x1 - (dGtdr_func(x1, Nb) / d2Gtdr2_func(x1, Nb))
            tol = Math.Abs(x2 - x1)
            x1 = x2
        End While
        Return (x2)
    End Function
    Private Function sizefactor_func(ByVal i As Integer) As Double 'Size factor takes
into account that fact that tiny precipitates (<2nm) can't completely pin dislocations.
It increase linearly with R becomes 1 at R>=1 nm.
        Dim SF As Decimal = 0
        SF = Math.Min(1, (1000000000.0 * Radius(i)))
        Return (SF)
    End Function
    Private Function strainT_func(ByVal i As Integer) As Double
        'newton raphson method with finite difference used
        Dim func, dfunc, h, tolerance, constant, tol As Double
        func = 0 : dfunc = 0 : h = 0 : tolerance = 0 : constant = 0 : tol = 0
        Dim flow_stress_offset As Decimal = CDec(TextBox16.Text)
        h = 0.0000001
        x1 = 0.000001
        x2 = 1
        tol = 0.00001
        constant = nippon_func(NBT0, flow_stress_offset) + (SIGMA(i) / 1000000.0)
        tolerance = Math.Abs(x2 - x1)
        While (tolerance > 2 * tol)
            func = nippon_func(NBT0, x1) - constant
            dfunc = (nippon_func(NBT0, x1 + h) - nippon_func(NBT0, x1 - h)) / (2 * h)
            x2 = x1 - func / dfunc
            tolerance = Math.Abs(x2 - x1)
            x1 = x2
        End While
        Return (x2)
    End Function
    Private Function Nb0_func(ByVal t1 As Decimal, ByVal Nb As Decimal) As Double
        Nb0 = -(93 * 93 * K1_func(t1) * K2_func(t1))
        Return (Nb0)
    End Function
    Private Function Nb1_func(ByVal t1 As Decimal, ByVal Nb As Decimal) As Double
        Nb1 = ((NT * 93 * 93 * K1_func(t1)) - (93 * 12 * Nb * K2_func(t1)) - (93 * 14 *
Nb * K1_func(t1)) + (93 * 93 * CT * K2_func(t1))) * Nb
        Return (Nb1)
    End Function
    Private Function Nb2_func(ByVal t1 As Decimal, ByVal Nb As Decimal, ByVal CT As
Decimal, ByVal NT As Decimal) As Double
```

```
        Nb2 = ((12 * 93 * K2_func(t1)) + (NT * Nb * 12 * 93) - (12 * 14 * Nb ^ 2) + 93
* 14 * K1_func(t1) + (CT * Nb * 14 * 93)) * Nb ^ 2
        Return (Nb2)
    End Function
    Private Function Nb3_func(ByVal t1 As Decimal, ByVal Nb As Decimal, ByVal CT As
Decimal, ByVal NT As Decimal) As Double
        Nb3 = ((2 * 12 * 14 * Nb) - (CT * 14 * 93) - (NT * 12 * 93)) * Nb ^ 3
        Return (Nb3)
    End Function
    Private Function Nb4_func(ByVal Nb As Decimal) As Double
        Return (-168 * Nb ^ 4)
    End Function
    Private Function K1_func(ByVal t1 As Decimal) As Double
        K1 = 10 ^ (3.42 - (7900 / t1))
        Return (K1)
    End Function
    Private Function K2_func(ByVal t1 As Decimal) As Double
        K2 = 10 ^ (2.8 - (8500 / t1))
        Return (K2)
    End Function
    Private Function Tsolution_func(ByVal t1 As Decimal, ByVal NbT As Decimal, ByVal CT
As Decimal, ByVal NT As Decimal) As Double
        Return (Nb0_func(t1, NbT) + Nb1_func(t1, NbT) + Nb2_func(t1, NbT, CT, NT) +
Nb3_func(t1, NbT, CT, NT) + Nb4_func(NbT))
    End Function
    Private Sub Tsol_calculation()  'Solutionizing temperature calculation
        NbT = CType(TextBox2.Text, Decimal)
        NT = CType(TextBox4.Text, Decimal)
        CT = CType(TextBox3.Text, Decimal)
        x1 = 600 : x2 = 1500
        While (Math.Abs(x2 - x1) > 2 * 0.000000001)
            x_intermediate = (x1 + x2) / 2
            If ((Tsolution_func(x1, NbT, CT, NT) * Tsolution_func(x_intermediate, NbT,
CT, NT)) < 0) Then
                x2 = x_intermediate
            ElseIf ((Tsolution_func(x2, NbT, CT, NT) * Tsolution_func(x_intermediate,
NbT, CT, NT)) < 0) Then
                x1 = x_intermediate
            End If
        End While
        Tsol = (x1 + x2) / 2
    End Sub
    Private Function Grt_func(ByVal Rho As Decimal) As Double ''driving force for
recrsytallization.
        Return CDec(0.5 * Rho * mu * b ^ 2)
    End Function
    Private Function SE_SG_func(ByVal temp As Decimal) As Double '' Surface Energy of
Subgrains
        Return (0.75 - (0.0005 * (temp - (850 + 273)))) 'Grain boundary energy (J/m2).
    End Function
    Private Sub recrystalization_model()
        cells = this 'number of loops actually used.
        Dim alpha_D_factor As Decimal = 2 'the pipe diffusion is this factor multiplied
with bulk diffusion
        Dim Dself As Decimal = 0.00007 * Math.Exp(-285000 / (Rg * Temp))
        Dim frac, Nucleation_V(cells), D_Eqv, Shell_V, Rex_V(cells), V_DG_Eqv, V_DG,
surface_area As Decimal
        Dim initiation_flag As Integer
```

```
        Dim shell_width As Decimal = 0.0000025
        Dim surface_vol_available(cells) As Double
        'local coarsening declarations
        Dim local_coarse_Flag, R0 As Decimal : Zener(cells) = 0 : local_coarse_Flag = 0
: R0 = 0
        Dim delta_nuclei_fraction(cells) As Decimal
        Dim delta_growth_vol As Double = 0
        N_nuclei(0) = 0 : chi_critical(0) = 100 : Rex_V(cells) = 0 :
N_nuclei_cumu(cells) = 0 : Non_Rex_R(cells) = 0 : delta_nuclei_fraction(cells) = 0 :
frac = 110 : initiation_flag = 1 : local_coarse_Flag = 0
        D_Eqv = 3 / Sv
        R_Eqv = (D_Eqv / 2) : V_DG_Eqv = pi_sp * (R_Eqv ^ 3)
        V_DG = pi_sp * ((Di / 2) ^ 3)
        surface_area = 4 * pi * (R_Eqv ^ 2) : nuclei_fraction_const = (Math.Exp(-pi * 9
/ 4))
        Shell_V = surface_area * shell_width
        alpha = 0.000000004 * (k ^ 2) * (Temp ^ 2) * (Math.Sinh(Eb / (k * Temp)) - (Eb
/ (k * Temp))) / ((b * Math.Sqrt(2)) ^ 3 * Eb * alpha_D_factor * Dv)  'alpha in Cahn's
equation.
        Mi = CDbl(((0.192 / Temp) * Math.Exp(-20837.14 / Temp)))    'Tom's C-Mn
Mobility.
        Zener(0) = 6.283185308 * FZ * (Radius(0) ^ 2) * N(0) * GB   'Zener
        M_HAG(0) = (1 / (alpha * 0.006011840689 * Nbl(1) + (1 / Mi)))
        R_subgrain_avg(0) = 0
        chi_critical(0) = 100
        Growth_Vol(0) = Shell_V
        radius_critical(0) = 2 * GB / (0.5 * Grt_func(rho(0))) ' 0.5 factor signifies
that each buldge has only half the effective dislocation density for a particular grain
        RrexN(0) = radius_critical(0)
        Dim V_temp As Double = 0
        For i = 1 To cells
            Growth_velocity = 0 : delta_growth_vol = 0 'initializing it in every loop

            ppt_VF(i) = pi_sp * (Radius(i) ^ 3) * N(i)
            ' Zener(i) = FZ * CDbl((2 * pi * (Radius(i) ^ 2) * N(i) * gamma)) 'Zener
pressure  FZ is the no of times of classical value. FZ is the no of times of classical
value.
            Zener(i) = FZ * (3 / 2) * ppt_VF(i) * GB / Radius(i)
            GR(i) = CDbl(Grt_func(rho(i)))
            G_Z(i) = (GR(i) - Zener(i) + Math.Abs(GR(i) - Zener(i))) / 2
'driving force - Zener drag
            M_HAG(i) = (1 / (alpha * 0.006011840689 * Nbl(i) + (1 / Mi)))
' high angle grain boundary mobility.

            '======================== 1. Rex Nucleation Model
            radius_critical(i) = 2 * GB / (0.5 * GR(i)) ' 0.5 tells that each buldge
has only half the effective dislocation density for a particular grain
            If Act_L(i) = 0 Then Act_L(i) = Act_L(i - 1) 'sometimes the act length
suddenly becomes 0. To counteract that problem.
            R_subgrain_avg(i) = R_subgrain_avg(i - 1) + _
                (((2 * (Dself / Act_L(i)) * (time(i) - time(i - 1)) * _
                  Math.Sinh(frac * 0.054 * SIGMA(i) * b ^ 2 * Act_L(i) / (M_Taylor * k
* Temp)))) * (rho(i) * Dself * 1.0E+22 * 1.85 / N(i)))  'New subgrain growth model
            chi_critical(i) = Math.Min((radius_critical(i) / R_subgrain_avg(i)), 3) :
chi_critical(i) = Math.Min(chi_critical(i - 1), chi_critical(i))
            N_available_per_grain(i) = (V_DG * Sv / (pi * radius_critical(i) ^ 2)) *
Math.Max(0, (1 - (Nucleation_V_cumu(i - 1) / Shell_V)))
```

```
            nuclei_fraction_cumu(i) = (Math.Exp(-pi * ((chi_critical(i)) ^ 2) / 4)) -
nuclei_fraction_const
            delta_nuclei_fraction(i) = nuclei_fraction_cumu(i) - nuclei_fraction_cumu(i
- 1)
            N_nuclei(i) = delta_nuclei_fraction(i) * N_available_per_grain(i)
'N_nuclei is the no of new grains nucleated in that time step(t(i)-t(i-1).
            N_nuclei_cumu(i) = N_nuclei_cumu(i - 1) + N_nuclei(i)
            If G_Z(i) > 0 Then
                '+ve driving force
                If chi_critical(i) < 3 Then
                    RrexN(i) = RrexN(i - 1) + M_HAG(i) * G_Z(i) * (time(i) - time(i -
1))
                Else
                    RrexN(i) = RrexN(i - 1) + 0
                End If
                Nucleation_V_cumu(i) = N_nuclei_cumu(i) * 0.5 * pi_sp * (RrexN(i) ^ 3)
                If Nucleation_V_cumu(i) > Shell_V Then
                    'Site Saturation- Pure Growth
                    Growth_Vol(i) = Growth_Vol(i - 1) + 4 * pi * (Non_Rex_R(i - 1) ^ 2)
* M_HAG(i) * G_Z(i) * (time(i) - time(i - 1))
                Else
                    Growth_Vol(i) = Shell_V
                End If
            Else
                'Over pinned Microstructure.
                If chi_critical(i) < 3 Then
                    RrexN(i) = RrexN(i - 1) + rex_local_growth(i) * (time(i) - time(i -
1))
                Else
                    RrexN(i) = RrexN(i - 1) + 0
                End If
                Nucleation_V_cumu(i) = N_nuclei_cumu(i) * 0.5 * pi_sp * (RrexN(i) ^ 3)
                If Nucleation_V_cumu(i) > Shell_V Then
                    'Site Saturation- Pure Growth
                    Growth_Vol(i) = Growth_Vol(i - 1) + 4 * pi * (Non_Rex_R(i - 1) ^ 2)
* rex_local_growth(i) * (time(i) - time(i - 1))
                Else
                    Growth_Vol(i) = Shell_V
                End If
            End If
            If Nucleation_V_cumu(i) < Shell_V Then
                V_temp = Nucleation_V_cumu(i)
            Else
                V_temp = Growth_Vol(i)
            End If
            If V_temp < V_DG_Eqv Then
                Non_Rex_R(i) = ((V_DG_Eqv - V_temp) / pi_sp) ^ 0.3333

                Non_Rex_R(i) = Math.Min(R_Eqv, Non_Rex_R(i))
                Non_Rex_R(i) = Math.Max(0, Non_Rex_R(i))
                Act_Rex_Vol_frac(i) = 1 - (Non_Rex_R(i) / R_Eqv) ^ 3
            Else
                Act_Rex_Vol_frac(i) = 1
            End If
        Next i
        Dim Rex_GS As Decimal
        Rex_GS = 2000000.0 * (Di / 2) / (N_nuclei_cumu(cells - 1) ^ 0.333333)
    End Sub                                                  'Recrystallization Model
```

```
    Private Function rex_local_growth(ByVal i As Integer)
        Dim Rnew, t_1, t_2, temp1, Db_sellars, FvEq As Double
        Rnew = 0 : t_2 = 0 : temp1 = 0 : Db_sellars = 0
        Dim fgb As Decimal = 0.6
        Dim Diffusivity As Double
        Diffusivity = 0.00041 * Math.Exp(-172500 / (Rg * Temp))
        Call NbEqR_sub(i)
        FvEq = (NbT - NbEqR) / (88 - NbEqR)
        If FvEq = 0 Then FvEq = 2.71828 ' when Fveq =0 it makes subsequent calculation
diverge, hence done to fix it.
        ppt_spacing = (1 / N(i)) ^ 0.3333
        temp1 = GB / (2 * SE)
        A_coarsening(i) = (2 / 3) + (temp1) + ((temp1 ^ 3) / 3)
        B_coarsening(i) = -0.5 * Math.Log(FvEq)
        kC_Maple(i) = fgb * (0.000000009 * Diffusivity * SE * Nbl(cells - 2) * (55 /
9300) * Math.Exp(Eb / (k * Temp)) * 0.00000685) / (32 * A_coarsening(i) *
B_coarsening(i) * Rg * Temp)
        Rnew = FZ * (3 / 2) * GB * ppt_VF(i) / GR(i)
        t_1 = (Rnew ^ 4 - Radius(i) ^ 4) / (kC_Maple(i))
        t_2 = t_up_bisection_method(i, ppt_spacing, t_1) ' Analogous to t1+t2 in maple
        growth_rate(i) = ppt_spacing / (t_2)  'velocity m/sec
        Growth_velocity = 0.5 * (growth_rate(i - 1) + growth_rate(i))
        Return (Growth_velocity)
    End Function
    Private Function t_up_bisection_method(ByVal i As Integer, ByVal ppt_spacing As
Decimal, ByVal t_dash As Decimal) As Decimal
        x1 = t_dash
        x2 = x1 + 300
        While (Math.Abs(x2 - x1) > 2 * 0.0001)
            x_intermediate = (x1 + x2) / 2
            If ((local_coarse_func(x1, i, t_dash) * local_coarse_func(x_intermediate,
i, t_dash)) < 0) Then
                x2 = x_intermediate
            ElseIf ((local_coarse_func(x2, i, t_dash) *
local_coarse_func(x_intermediate, i, t_dash)) < 0) Then
                x1 = x_intermediate
            End If
        End While
        Return ((x1 + x2) / 2)
    End Function
    Private Function local_coarse_func(ByVal t_up As Decimal, ByVal i As Integer, ByVal
t_dash As Decimal) As Decimal
        Dim func As Double
        func = (M_HAG(i) * GR(i) * (t_up - t_dash) - M_HAG(i) * 2 * FZ * GB * ((4 / 3)
* pi * Radius(i) ^ 3 * N(i)) * (1 / kC_Maple(i)) * ((Radius(i) ^ 4 + kC_Maple(i) *
t_up) ^ (3 / 4) - (Radius(i) ^ 4 + kC_Maple(i) * t_dash) ^ (3 / 4))) _
         - (ppt_spacing)
        Return (func)
    End Function
    Private Sub Button3_Click(ByVal sender As System.Object, ByVal e As
System.EventArgs) Handles Button3.Click
        Call flowstress_calculation()
        TextBox9.Text = CStr(CType(Math.Round(flow / 1000000.0, 2), String) + "  " +
CStr("MPa"))
    End Sub 'flow stress button
```

```
    Private Sub Button4_Click(ByVal sender As System.Object, ByVal e As
System.EventArgs) Handles Button4.Click
        Call Tsol_calculation()
        TextBox12.Text = CStr(Math.Round((Tsol - 273), 2)) + "  " + CStr("Deg C")
    End Sub 'Tsol button
    Private Sub data_reader_and_initialize_constants()
        NbT = CDec(TextBox2.Text)
        NBT0 = NbT
        CT = CDec(TextBox3.Text)
        NT = CDec(TextBox4.Text)
        NT_temporary = NT
        MnT = CDec(TextBox5.Text)
        Call Tsol_calculation()
        Temp = (CDec(TextBox1.Text)) + 273 'temperature in Kelvin
        Di = CDec(TextBox6.Text) * 0.000001
        strainrate = CDec(TextBox7.Text)
        astrain = CDec(TextBox8.Text)
        time2simulate = CInt(TextBox19.Text)
        a = 0.000000000358 'Lattice Parameter.
        b = (a / Math.Sqrt(2)) 'Burger vector (m).
        fraction_Nb_dis = 1
        Uo = 285000
        FN = 0.0
        FZ = 4
        QS = 20000
        Rg = 8.314
        Nbtime_coarsening_flag = 0
        Dv = 0.000083 * Math.Exp(-266500 / (Rg * Temp)) ' bulk diffusion
        Db = 0.00041 * Math.Exp(-172500 / (Rg * Temp))  ' boundary diffusion
        Dp = 0.00041 * Math.Exp(-172500 / (Rg * Temp))  ' pipe diffusion.

        alpha = 1.05 'Constant in the Deschamps-Brechet Model. Appears in the growth
rate equation during nucleation and growth stage.
        SE = 0.000025 * ((Tsol - Temp) ^ 1.5) + 0.375 ' Expression for NbCN/Austenite
interphase energy as a function of T and composition (J/m2)
        GB = -0.0005 * (Temp - (850 + 273)) + 0.75    'Grain boundary energy (J/m2).
        mu = 81000000000.0 * (1 - (0.91 * (Temp - 300) / 1810)) 'Shear modulus of
austenite (Pa).
        Y_mod = (mu * 8) / 3 'Y_mod is the same variable what E was in maple
originally(youngs modulus).
        RC = b ';Cut of radius for dislocation stress field.
        Vm = 0.0000128
        density = 7900
        MW = 0.093 'Molecular Weight of Niobium (kg/mole)
        k = 1.38E-23 'boltzman const
        M_Taylor = 3.1
        alpha_Taylor = 0.15
        Debye = 1500 / (2 * a)
        c1_AR = (64 * Debye * Math.Exp(-Uo / (Rg * Temp)) / (9 * (M_Taylor ^ 3) *
(alpha_Taylor ^ 2) * Y_mod))
        c2 = Vo / (k * Temp)
        Avrami = 1
        dC1 = 8 * pi * SE
        dC2a = 4 * pi * Rg * Temp / Vm
        dC3 = 0.714285 * mu * b * b / pi
        dC4 = 1 - Math.Log(b)
        dC5 = mu * b * b / 5
        rc1 = Di / 2
```

```
    End Sub
    Private Sub Recovery_Module(ByVal i As Integer)
        table(0, 0) = time(i - 1)                         'initial condition for the
table,
        table(0, 1) = SIGMA(i - 1)                        'initial condition for the
table
        h = inc / 2
        Niterations = 3
        For loop_runge_kutta As Integer = 1 To Niterations
            k1x = table(loop_runge_kutta - 1, 0)
            k1y = table(loop_runge_kutta - 1, 1)
            K1 = dsolve_dSdt_RK(i, k1y)        'K1 is the const calculated in
Runge.Kutta method
            k2x = k1x + h / 2
            k2y = k1y + h * K1 / 2
            K2 = dsolve_dSdt_RK(i, k2y)        'K2 is the const calculated in
Runge.Kutta method
            k3x = k1x + h / 2
            k3y = k1y + h * K2 / 2
            K3 = dsolve_dSdt_RK(i, k3y)        'K3 is the const calculated in
Runge.Kutta method
            k4x = k1x + h
            k4y = k1y + h * K3
            K4 = dsolve_dSdt_RK(i, k4y)        'K4 is the const calculated in
Runge.Kutta method
            table(loop_runge_kutta, 0) = table(loop_runge_kutta - 1, 0) + h
            table(loop_runge_kutta, 1) = table(loop_runge_kutta - 1, 1) + (h * (K1 + K4
+ 2 * (K2 + K3)) / 6)
        Next loop_runge_kutta
        SIGMA(i) = table(2, 1)
    End Sub
    Private Sub flowstress_calculation() 'Stress due to dislocations calculated as
total stress - yield stress
        NbT = CType(TextBox2.Text, Double)
        astrain = CType(TextBox8.Text, Double)
        strainrate = CType(TextBox7.Text, Double)
        Di = CType(TextBox6.Text, Double) * 0.000001
        Temp = (CType(TextBox1.Text, Double)) + 273
        Dim carbon As Decimal = CDec(TextBox3.Text)
        Dim flow_stress_offset As Decimal = CDec(TextBox16.Text)
        flow = (nippon_func(NbT, astrain) - nippon_func(NbT, flow_stress_offset)) *
1000000.0
    End Sub
    Private Sub Hardening_model()
        Dim offset As Decimal = 0.01
        S1 = CDbl(nippon_func(NbT, astrain + offset))
        S2 = CDbl(nippon_func(NbT, offset))
        j = 1
        beta = 0.5
        kshear = 0.07 'Constants that enter into the Deschamps-Brechet hardening
model.'changes done in kshear from 0.06 to 0.08
        RcH = 0.8 * 2 * beta * b / kshear 'Transition radius from particle shear to by
pass.
        STDEVR = 2                        'Ratio of STDEV/R[1,i] = 2 in this case.
        For i = 1 To cells
            strainT = strainT_func(i)                    'Effective strain remaining
after a given amount of recovery.
```

```
            S3T(i) = nippon_func(Nbl(1), strainT_func(i) + offset) 'S3 calculated for
the recovered material with no precipitates.
            STDEV = Radius(i) / 2               'Standard deviation of the particle
size distribution.
            Kd = 2 / (STDEV * Math.Sqrt(pi) * (1 + erf_func(STDEVR)))
            intI = ((Kd * (STDEV) ^ 2 / 2) * (Math.Exp(-STDEVR ^ 2) - Math.Exp(-((RcH -
Radius(i)) / STDEV) ^ 2))) + _
                    Kd * (STDEV) * Radius(i) * (Math.Sqrt(pi) / 2) * (erf_func(STDEVR)
+ erf_func((RcH - Radius(i)) / (STDEV)))
            intII = Kd * STDEV * (Math.Sqrt(pi) / 2) * (1 - erf_func((RcH - Radius(i))
/ (STDEV)))
            Spptn(i) = M_Taylor * Math.Sqrt(2 * N(i) * (Radius(i) ^ 3)) * ((kshear * mu
* b * intI + kshear * mu * b * RcH * intII) ^ 1.5) / _
                        (1000000.0 * b * Radius(i) * Math.Sqrt(2 * beta * mu * b * b))
'This is the precipitation hardening in MPa
            ''''calculation of softening fraction
            rec_contribution(i) = Math.Sqrt(Spptn(i) ^ 2 + S3T(i) ^ 2) 'hardness of
recrysallized material taking account of precipitation.
            rex_contribution = Math.Sqrt(Spptn(i) ^ 2 + (nippon_func(Nbl(1), offset)) ^
2) 'hardness of recovered material taking account of precipitation.
            S3_with_rex = rec_contribution(i) * (1 - Act_Rex_Vol_frac(i)) +
rex_contribution * Act_Rex_Vol_frac(i) 'Final value of S3.
            softening_fraction(i) = ((S1 - S3_with_rex) / (S1 - S2)) 'Sofening
fraction.
            flow_softening(i) = Math.Sqrt(Spptn(i) ^ 2 + SIGMA(i) ^ 2)
        Next i
    End Sub
    Private Sub initialise_variables()
table(500000, 1) = 0 : nbx(6000, 6000) = 0 : interval = 0.0000000000000001 : cells =
1000000 : Tsol = 0 : NbT = 0 : CT = 0 : NT = 0 : NBT0 = 0 : NT_temporary = 0 : MnT = 0
: Di = 0 : strainrate = 0 : astrain = 0 : fraction_Nb_dis = 0 : Uo = 0 : Vo = 0 : QS =
0 : FZ = 0 : b = 0 : Rg = 0 : Dv = 0 : Db = 0 : Dp = 0 : Nbtime_coarsening_flag = 1 :
Deff = 0 : alpha = 0 : SE = 0 : GB = 0 : mu = 0 : Y_mod = 0 : rhot = 0 : a = 0 : ab = 0
: Vm = 0 : density = 0 : MW = 0 : k = 0 :         M_Taylor = 0 : alpha_Taylor = 0 :
Debye = 0 : M_NbT = 0 : AR = 0 : dSdt = 0 : inc = 0 : R = 0 : Nc(cells) = 0 :
time(cells) = 0 : Radius(cells) = 0 : N(cells) = 0 : dRdt(cells) = 0 : dNdt(cells) = 0
: Nbl(cells) = 0 : dNdt2(cells) = 0 : Zener(cells) = 0 : Force(cells) = 0 : X(cells) =
0 : SIGMA(cells) = 0 : rho(cells) = 0 : Rzero(cells) = 0 : dNdtC(cells) = 0 :
Rstar(cells) = 0 :           coarsef(cells) = 0 : Vf(cells) = 0 : Vfc(cells) = 0 :
S3T(cells) = 0 : K1 = 0 : K2 = 0 : K3 = 0 : K4 = 0 : Nbo = 0 : Nb0 = 0 : Nb1 = 0 : Nb2
= 0 : Nb3 = 0 : Nb4 = 0 : w = 0 : ke = 0 : dNb = 0 : ks_general = 0 : ks_bulk = 0 = 0 :
R0t = 0 : Rt = 0 : FvEq = 0 : Ntot = 0 : NbEqR = 0 : fcoarse = 0 : dNtdt = 0 : Avrami =
0 : dNtdt2 = 0 : dRtdtc = 0 : R0 = 0 : NbR = 0 = 0 : dNtdtC = 0 : dRtdt = 0 : dRtdtg =
0 : dRtdt2 = 0 : NbEqRbar = 0 : radius_temp = 0 = 0 : x1 = 0 : x2 = 0 : x_intermediate
= 0 : counter = 0 :f1 = 0 : f_intermediate = 0 : C = 0 : Nb = 0 : Ns = 0 : NbEq = 0 : f
= 0 : ks = 0 : Gv = 0 : Vol = 0 : Area = 0 : RC = 0 : dGt = 0 : dGtdr = 0 : r_nt = 0 :
G_nt = 0 : dGtdr_for_R0 = 0 : r_nt0 = 0 : flow = 0 : FC = 0 : this2 = 0 : PR = 0 : PR2
= 0 : Nbtemp = 0 : this = 0 : Pnet = 0 : VV = 0 : kf = 0 : V1 = 0 : V2 = 0 : P1 = 0 :
P2 = 0 : sflimit = 0 : Sv = 0 : Dcrt = 0 : Num_rex = 0 : Eb = 0 : beta = 0 : Mi = 0 :
GR(cells) = 0 : G_Z(cells) = 0 : S1 = 0 : S2 = 0 : samplingF = 0 : j = 0 : kshear = 0 :
strainT = 0 : RcH = 0 : STDEV = 0 : STDEVR = 0 : Kd = 0 : intI = 0 : intII = 0 :
Spptn(cells) = 0 : DRf = 0 : c1_AR = 0 : c2 = 0 : l1 = 0 : l2 = 0 : l3 = 0 : l4 = 0 :
Rtemp = 0 : Ntemp = 0 : GNoutB = 0 : GRoutB = 0 : CNoutB = 0 : CRoutB = 0 : NoutB = 0 :
RoutB = 0 : incs = 0 : Nst = 0 : Rst = 0 : NbsT = 0 : table(500000, 1) = 0 : F_left = 0
: F_right = 0 : k1x = 0 : k1y = 0 : k2x = 0 : k2y = 0 : k3x = 0 : k3y = 0 : k4x = 0 :
k4y = 0 : S3_with_rex = 0 : temporary4 = 0 : temporary5 = 0 : temporary1 = 0 :
temporary2 = 0 : temporary3 = 0
```

```
temporary0 = 0 : rec_contribution(cells) = 0 : rex_contribution = 0 : nbx(6000, 6000) =
0 : dC1 = 0 : dC2 = 0 : dC2a = 0 : dC3 = 0 : dC4 = 0 : dC5 = 0 : Ca = 0 : Cb = 0 : Ns_a
= 0 : Ns_b = 0 : c_equv = 0 : Ns_equv = 0 : C_Ns_Eq = 0 : d2GtdrdNb_c1 = 0 :
radius_sb(cells) = 0 : radius_critical(cells) = 0 : R_subgrain_avg(cells) = 0 :
Rex_subgrain_mob_fit1 = 0 : Mobility_LowAngle(cells) = 0 : rho_integral = 0 :
N_nuclei(cells) = 0 : chi_critical(cells) = 0 : Act_Rex_Vol_frac(cells) = 0 :
softening_fraction(cells) = 0 : M_HAG(cells) = 0 : appld_stress = 0 :
flow_softening(cells) = 0 : N_nuclei_cumu(cells) = 0 : Nucleation_Volume(cells) = 0 :
c1 = 0 : ppt_spacing = 0 : time2simulate = 1 : SG_Driving_force(cells) = 0 :
Growth_Driving_Force(cells) = 0 : Zener(cells) = 0 : phase2_growth(cells) = 0 :
film_nucleation(cells) = 0 : nuclei_fraction_cumu(cells) = 0 :
growth_rate(cells) = 0 : h = 0 : FN = 0 : Temp = 0 : Niterations = 1 : interval =
0.0000000000000001
    End Sub

    'Display Modeling Output
    Private Sub btn_print_form_Click(ByVal sender As System.Object, ByVal e As
System.EventArgs)
        Dim pf As New Microsoft.VisualBasic.PowerPacks.Printing.PrintForm
        pf.Form = Me
        pf.PrintAction = Printing.PrintAction.PrintToFile
        Dim path As String = "c:\users"
        pf.Print(Me, PowerPacks.Printing.PrintForm.PrintOption.FullWindow)
    End Sub
    Private Sub btn_get_data_Click(ByVal sender As System.Object, ByVal e As
System.EventArgs) Handles btn_get_data.Click
        btn_get_data.Visible = False
        If CheckBox11.Checked = True Then
            Call Excel_writer()
        End If
        If CheckBox12.Checked = True Then
            Call Text_writer()
        End If
        btn_get_data.Visible = True
    End Sub
    Private Sub Excel_writer()
        'Storing the final data into a 2D array results to b printed in excel
        Dim results(cells, 16) As Object
        For j As Integer = 0 To cells
            results(j, 0) = time(j)
            results(j, 1) = N(j)
            results(j, 2) = Radius(j) * 1000000000.0
            results(j, 3) = Nbl(j)
            results(j, 4) = SIGMA(j) / 1000000.0
            results(j, 5) = rho(j)
            results(j, 6) = GR(j)
            results(j, 7) = G_Z(j)
            results(j, 8) = M_HAG(j)
            results(j, 9) = radius_critical(j)
            results(j, 10) = R_subgrain_avg(j)
            results(j, 11) = chi_critical(j)
            results(j, 12) = N_nuclei(j)
            results(j, 13) = N_nuclei_cumu(j)
            results(j, 14) = Act_Rex_Vol_frac(j)
            results(j, 15) = softening_fraction(j)
            results(j, 16) = Act_L(j)
        Next j
        Dim oExcel As Object
```

```
        Dim oBook As Object
        Dim oSheet As Object
        'Start a new workbook in Excel
        oExcel = CreateObject("Excel.Application")
        oBook = oExcel.Workbooks.Add
        'Add headers to the worksheet on row 1
        oSheet = oBook.Worksheets(1)
        oSheet.Range("A1").Value = "Time (s)"
        oSheet.Range("B1").Value = "No of Ppt"
        oSheet.Range("C1").Value = "Ppt Rad, nm"
        oSheet.Range("D1").Value = "Nb (wt%)"
        oSheet.Range("E1").Value = "Stress_Discl,MPa"
        oSheet.Range("F1").Value = "Dislocation Density (rho)"
        oSheet.Range("G1").Value = "G"
        oSheet.Range("H1").Value = "G-Z"
        oSheet.Range("I1").Value = "M_HAGB"
        oSheet.Range("J1").Value = "Radius_Critical"
        oSheet.Range("K1").Value = "Subgrain radius"
        oSheet.Range("L1").Value = "Chi_Critical"
        oSheet.Range("M1").Value = "No of Rex Nuclei"
        oSheet.Range("N1").Value = "N_Rex_Nuclei_cumu"
        oSheet.Range("O1").Value = "Àct_Rex_frac"
        oSheet.Range("P1").Value = "Softening_frac"
        oSheet.Range("Q1").Value = "Act Length"
        'Transfer the array to the worksheet starting at cell A2
        oSheet.Range("A2").Resize(cells, 17).Value = results
        'Save the Workbook and Quit Excel
        oBook.SaveAs("TMP.Model.Results.xlsx")
        oExcel.Quit()
        System.Diagnostics.Process.Start("C:\users\kash\my
documents\TMP.Model.Results.xlsx")
    End Sub
    Private Sub Text_writer()
        Dim textWriter As New System.IO.StreamWriter("results.txt")
        Dim line As String
        line = CStr("time    ")
        textWriter.WriteLine(line)
        For cc As Integer = 1 To cells
            line = CStr(time(cc)) + "   " + CStr(Radius(cc)) + "   " + CStr(N(cc)) + "   "
+ CStr(Act_Rex_Vol_frac(cc))
            textWriter.WriteLine(line)
        Next cc
        textWriter.Flush()
        textWriter.Close()
        System.Diagnostics.Process.Start("results.txt")
    End Sub
    Private Sub btn_Draw_Graph_Click(ByVal sender As System.Object, ByVal e As
System.EventArgs) Handles btn_Draw_Graph.Click
        Dim graph_array(cells, 1) As Double
        graph_array(cells, 1) = 0
        If CheckBox9.Checked = True Then
            Chart1.Series.Clear()
            ' create a line chart series
            Dim newSeries As New Series(0)
            newSeries.ChartType = SeriesChartType.Line
            newSeries.BorderWidth = 2
            Chart1.Series.Add(newSeries)
        End If
```

```
Chart1.ChartAreas(0).AxisX.Title = "Time (sec)"
Chart1.ChartAreas(0).AxisX.Minimum = 0.0001
If CheckBox1.Checked = True Then
    For i As Integer = 1 To cells
        graph_array(i, 0) = time(i)
        graph_array(i, 1) = N(i)
        Chart1.ChartAreas(0).AxisY.Title = "No of Ppt"
    Next i
ElseIf CheckBox2.Checked = True Then
    For i As Integer = 1 To cells
        graph_array(i, 0) = time(i)
        graph_array(i, 1) = (2000000000.0 * Radius(i))
        Chart1.ChartAreas(0).AxisY.Title = "Dia (nm)"
    Next i
ElseIf CheckBox3.Checked = True Then
    For i As Integer = 1 To cells
        graph_array(i, 0) = time(i)
        graph_array(i, 1) = Nbl(i)
        Chart1.ChartAreas(0).AxisY.Title = "% Nb"
    Next i
ElseIf CheckBox4.Checked = True Then
    For i As Integer = 1 To cells
        graph_array(i, 0) = time(i)
        graph_array(i, 1) = (SIGMA(i)) / 1000000.0
        Chart1.ChartAreas(0).AxisY.Title = "SIGMA MPa"
    Next i
ElseIf CheckBox5.Checked = True Then
    For i As Integer = 1 To cells
        graph_array(i, 0) = time(i)
        graph_array(i, 1) = rho(i)
        Chart1.ChartAreas(0).AxisY.Title = "rho"
    Next i
ElseIf CheckBox6.Checked = True Then
    For i As Integer = 1 To cells
        graph_array(i, 0) = time(i)
        graph_array(i, 1) = N_nuclei(i)
        Chart1.ChartAreas(0).AxisY.Title = " No of Nuclei"
    Next i
    graph_array(cells, 1) = N_nuclei(cells - 1)
ElseIf CheckBox7.Checked = True Then
    For i As Integer = 1 To cells
        graph_array(i, 0) = time(i)
        graph_array(i, 1) = (radius_critical(i)) * 1000000.0
        Chart1.ChartAreas(0).AxisY.Title = "critical_radius_um"
    Next i
    graph_array(cells, 1) = radius_critical(cells - 1) * 1000000.0
ElseIf CheckBox8.Checked = True Then
    For i As Integer = 1 To cells
        graph_array(i, 0) = time(i)
        graph_array(i, 1) = 1000000.0 * R_subgrain_avg(i)
        Chart1.ChartAreas(0).AxisY.Title = "Avg_SG_rad_um"
    Next i
    graph_array(cells, 1) = 1000000.0 * R_subgrain_avg(cells - 1)
ElseIf CheckBox10.Checked = True Then
    For i As Integer = 1 To cells
        graph_array(i, 0) = time(i)
        graph_array(i, 1) = 100 * Act_Rex_Vol_frac(i)
        Chart1.ChartAreas(0).AxisY.Title = "Act_Rex_Vol_frac"
```

```
        Next i
        graph_array(cells, 1) = 100 * Act_Rex_Vol_frac(cells - 1)
    ElseIf CheckBox13.Checked = True Then
        For i As Integer = 1 To cells
            graph_array(i, 0) = time(i)
            graph_array(i, 1) = (softening_fraction(i)) * 100
            Chart1.ChartAreas(0).AxisY.Title = "Softening Frac"
        Next i
        graph_array(cells, 1) = (softening_fraction(cells - 1)) * 100
    ElseIf CheckBox14.Checked = True Then
        For i As Integer = 1 To cells
            graph_array(i, 0) = time(i)
            graph_array(i, 1) = GR(i) / 1000000.0
        Next i
        Chart1.ChartAreas(0).AxisY.Title = "G(MPa)"
        graph_array(cells, 1) = GR(cells - 1) / 1000000.0
    ElseIf CheckBox15.Checked = True Then
        For i As Integer = 1 To cells
            graph_array(i, 0) = time(i)
            graph_array(i, 1) = G_Z(i) / 1000000.0
        Next i
        Chart1.ChartAreas(0).AxisY.Title = "G-Z(MPa)"
        graph_array(cells, 1) = G_Z(cells - 1) / 1000000.0
    ElseIf CheckBox18.Checked = True Then
        For i As Integer = 1 To cells
            graph_array(i, 0) = time(i)
            graph_array(i, 1) = (flow_softening(i)) / 1000000.0
        Next i
        Chart1.ChartAreas(0).AxisY.Title = "Flow Stress (MPa)"
        graph_array(cells, 1) = (flow_softening(cells - 1)) / 1000000.0
    ElseIf CheckBox19.Checked = True Then
        For i As Integer = 1 To cells
            graph_array(i, 0) = time(i)
            graph_array(i, 1) = N_nuclei_cumu(i)
        Next i
        Chart1.ChartAreas(0).AxisY.Title = "Num.Rex.Nuclei"
        graph_array(cells, 1) = N_nuclei_cumu(cells - 1)
    End If
    For c As Integer = 1 To cells
        Chart1.Series(0).Points.AddXY(graph_array(c, 0), graph_array(c, 1))
    Next c
    Chart1.Series(0).IsValueShownAsLabel = True
    Chart1.ChartAreas(0).AxisX.IsMarginVisible = False
    ' Set Logarithmic scale & base
    Chart1.ChartAreas(0).AxisX.IsLogarithmic = True
    Chart1.ChartAreas(0).AxisX.LogarithmBase = 10
    Chart1.Series(0).ChartType = SeriesChartType.FastLine
    Chart1.Series(0).Color = Color.GreenYellow
    Chart1.BorderSkin.BorderColor = Color.Transparent
    Chart1.BorderSkin.BorderDashStyle = ChartDashStyle.Solid
    Chart1.BorderSkin.BorderWidth = 1
    Chart1.ChartAreas(0).AxisY.LineWidth = 2
    'gridlines
    Chart1.ChartAreas(0).AxisX.MajorGrid.Enabled = True
    Chart1.ChartAreas(0).AxisX.MajorGrid.Interval = 0.5
    Chart1.ChartAreas(0).AxisX.MajorGrid.LineColor = Color.Green
    Chart1.ChartAreas(0).AxisY.MajorGrid.Enabled = True
    Chart1.ChartAreas(0).AxisY.MajorGrid.LineColor = Color.Green
```

```
        Chart1.ChartAreas(0).AxisY.MinorGrid.Enabled = True
        Chart1.ChartAreas(0).AxisY.MinorGrid.LineColor = Color.Green
        ' Set Title font
        Chart1.ChartAreas(0).AxisX.TitleFont = New Font("Times New Roman", 16,
FontStyle.Underline)
        Chart1.ChartAreas(0).AxisY.TitleFont = New Font("Times New Roman", 16,
FontStyle.Underline)
        ' Set Title color
        Chart1.ChartAreas(0).AxisX.TitleForeColor = Color.Red
        Chart1.ChartAreas(0).AxisY.TitleForeColor = Color.Red
        'zoom
        Chart1.ChartAreas(0).CursorX.IsUserEnabled = True
        Chart1.ChartAreas(0).CursorX.IsUserSelectionEnabled = True
        Chart1.ChartAreas(0).AxisX.ScaleView.Zoomable = True
        Chart1.ChartAreas(0).AxisX.ScrollBar.IsPositionedInside = True
        Chart1.ChartAreas(0).AxisX.ScaleView.MinSize = 1
        Chart1.ChartAreas(0).AxisX.ScaleView.MinSizeType = DateTimeIntervalType.Number
        Chart1.ChartAreas(0).AxisX.ScrollBar.BackColor = Color.Olive
        Chart1.ChartAreas(0).AxisX.ScrollBar.ButtonColor = Color.Green
        Chart1.ChartAreas(0).AxisX.ScrollBar.LineColor = Color.OldLace
        'zoom Y axis
        Chart1.ChartAreas(0).CursorY.IsUserEnabled = True
        Chart1.ChartAreas(0).CursorY.IsUserSelectionEnabled = True
        Chart1.ChartAreas(0).AxisY.ScaleView.Zoomable = True
        Chart1.ChartAreas(0).AxisY.ScrollBar.IsPositionedInside = True
        Chart1.ChartAreas(0).AxisY.ScaleView.MinSize = 1
        Chart1.ChartAreas(0).AxisY.ScaleView.MinSizeType = DateTimeIntervalType.Number
        Chart1.ChartAreas(0).AxisY.ScrollBar.BackColor = Color.Olive
        Chart1.ChartAreas(0).AxisY.ScrollBar.ButtonColor = Color.Green
        Chart1.ChartAreas(0).AxisY.ScrollBar.LineColor = Color.OldLace
    End Sub
    Private Sub Button6_Click(ByVal sender As System.Object, ByVal e As
System.EventArgs) Handles Button6.Click
        Chart1.ChartAreas(0).AxisX.ScaleView.ZoomReset(0)
        Chart1.ChartAreas(0).AxisY.ScaleView.ZoomReset(0)
    End Sub 'Reset Zoom
    Private Sub btn_Exit_Click(sender As System.Object, e As System.EventArgs) Handles
btn_Exit.Click
        Me.Close()
    End Sub
End Class
```